Advanced Robust Control Strategies of Mechatronic Suspensions for Cars

Zilin Feng

under supervision of
Dr. Simos A. Evangelou
and Dr. Imad M. Jaimoukha

A Thesis submitted in fulfilment of requirements for the degree of
Doctor of Philosophy
of Imperial College London

Department of Electrical and Electronic Engineering
Imperial College London

November 30, 2022

Statement of Originality

This is to certify that to the best of my knowledge, the content of this thesis is my own work. This thesis has not been submitted for any degree or other purposes.

I certify that the intellectual content of this thesis is the product of my own work and that all the assistance received in preparing this thesis and sources have been properly acknowledged.

Zilin Feng

November 30, 2022

Copyright Declaration

The copyright of this thesis rests with the author. Unless otherwise indicated, its contents are licensed under a Creative Commons Attribution-Non Commercial 4.0 International Licence (CC BY-NC).

Under this licence, you may copy and redistribute the material in any medium or format. You may also create and distribute modified versions of the work. This is on the condition that: you credit the author and do not use it, or any derivative works, for a commercial purpose.

When reusing or sharing this work, ensure you make the licence terms clear to others by naming the licence and linking to the licence text. Where a work has been adapted, you should indicate that the work has been changed and describe those changes.

Please seek permission from the copyright holder for uses of this work that are not included in this licence or permitted under UK Copyright Law.

Zilin Feng

November 30, 2022

Acknowledgment

I am grateful to Imperial College London, City University London and Jiangsu University of Science and Technology for the high-quality education they have provided with me. Ten years academic training lays the solid foundation for my research work in the electrical and engineering area. First and foremost, I would like to sincerely thank my supervisors Dr. Simos Evangelou and Dr. Imad M Jaimoukha for their invaluable advice, continuous support, and patience during my PhD study. Their immense knowledge and plentiful experience have encouraged me in all the time of my academic research and daily life. Our weekly meeting has made my research work less confused and more efficient. Simos has also assisted me to improve my english writing ability through proofreading all my publications and reports.

I would also like to express gratitude to Dr. Min Yu and Dr. Cheng Cheng for their treasured support which was really influential in shaping my implementation methodologies and critiquing my results. Min yu has established a highly reliable methodology in modelling and control, enabling the following work clear to take over. Cheng has helped me in terms of synthesising various control strategies for the research. Furthermore, I would like to thank Georgiou Anastasis who supported me by sharing his knowledge in model predictive control theory and our perfect collaboration promoted each other to the destination of our PhD journey. It was very fortunate for me to have had them as my research collabora-

tor during my PhD. They made my research go more smoothly than what I expected.

I would also like to thank my perfect PhD mate, Xiao Pan, who becomes my best friend since postgraduate period, for his truly help on PhD application and latex writing. Without him, I cannot grasp the chance to begin my doctoral studies and proceed the research smoothly. In addition, my closest friend, Jieming Ye, helped me comfortably adapted to both the study and life and provided me with many precious suggestions for my job hunting in my 3rd year PhD study.

I would like to thank my friends, office mates, colleagues and research team – Jiamin Xu, Taiyu Zhu, Qing Wen, Yunxiao Zhang, Cheng Hu, Tingqi Zhang, Zihang Dong, Guitao Yang, Wangkun Xu, Jianhong Wang, Jing Li and Qingwen Pang for a cherished time spent together in the office, and in social settings.

Finally, I would like to show my deepest appreciation to my parents. Without your unconditionally support and huge financial assistance, I could not make it in Imperial College London. Hence, this thesis is my return to my parents. And last, but not least, I must express my very profound gratitude to my wife Jue Wang, who provides me with unfailing support and continuous encouragement throughout my years of study and through the process of researching and writing this thesis. This accomplishment would not have been possible without her. Thank you for being my best friend. I owe you everything.

Abstract

Two novel mechatronic suspensions for road vehicles are studied in this thesis: the Series Active Variable Geometry Suspension (SAVGS) and the Parallel Active Link Suspension (PALS). The SAVGS and the PALS complement each other in terms of the vehicle categories they serve, which range from light high-performance vehicles (the Grand Tourer) to heavy SUV vehicles, respectively, based on the sprung mass and the passive suspension stiffness. Previous work developed various control methodologies for these types of suspension. Compared to existing active suspension solutions, both the SAVGS and the PALS are capable of low-frequency chassis attitude control and high-frequency ride comfort and road holding enhancement.

In order to solve the limitation of both SAVGS and PALS robustness, μ-synthesis control methodologies are first developed for SAVGS and PALS, respectively, to account for structured uncertainties arising from changes to system parameters within realistic operating ranges. Subsequently, to guarantee robustness of both low-frequency and high-frequency vehicle dynamics for PALS, the μ-synthesis scheme is combined with proportional-integral-derivative (PID) control, employing a frequency separation paradigm.

Moreover, as an alternative robustness guaranteeing scheme that captures plant nonlinearities and road unevenness as uncertainties and disturbances, a novel robust model predictive control (RMPC) based methodology is proposed for the

SAVGS, motivated by the promise shown by RMPC in other industrial applications.

Finally, aiming to provide further performance stability and improvements, feedforward control is developed for the PALS. Nonlinear simulations with a set of ISO driving situations are performed to evaluate the efficiency and effectiveness of the proposed control methods in this thesis.

Table of contents

Statement of Originality **3**

Copyright Declaration **5**

Acknowledgment **7**

Abstract **9**

Table of contents **11**

List of Figures **15**

List of Tables **25**

Abbreviations **27**

Chapter 1. Introduction **29**

1.1 Background 29

1.2 Aims and Contributions 31

1.2.1 Research challenges 31

1.2.2 Research Aims 31

1.2.3 Publications 32

1.3 Thesis Outline 33

Chapter 2. Literature Review **35**

2.1 Development of the Vehicle Suspension Structure 35

2.1.1 Passive Suspension 36

2.1.2 Semi-Active Suspension 37

2.1.3 Active Suspension 37

2.1.4 State-of-the-Art Active Suspension 38

2.2 Vehicle Modelling 41

2.2.1 Computer Software 43
2.2.2 Quarter-Car Nonlinear Multi-body Model 43
2.2.3 Full-Car Nonlinear Multi-body Model 44
2.2.4 Linear Equivalent Model with SAVGS and PALS 46
2.2.5 PALS Full-car Steady-state Model and Analysis 57
2.2.6 Road-profile Models 60
2.3 Vehicle Suspension Control 61
2.3.1 Chassis Attitude Control 62
2.3.2 Vibration Attenuation Control 64
2.3.3 Multi-objective Hybrid Control 72
2.4 Conclusion 74

Chapter 3. Uncertainties Investigation and Mu-Synthesis Control Design for a Full Car **75**
3.1 Introduction 75
3.2 Uncertainties Investigation 76
3.2.1 Uncertainties in linearisation of full car SAVGS 76
3.2.2 Uncertainties in linearisation of full car PALS 77
3.3 Robust Control Design 79
3.3.1 SAVGS Control Scheme 79
3.3.2 PALS μ-synthesis-based control scheme 88
3.4 Numerical Simulations and analysis 92
3.4.1 SAVGS Multi-body Full-car 92
3.4.2 PALS Multi-body Full-car 99
3.5 Conclusion 105

Chapter 4. Hybrid Control of Full-Car with PALS Under Variable Payload **106**
4.1 Introduction 106
4.2 Control Methodologies Development 107
4.2.1 Multi-objective blended control scheme 108
4.2.2 Benchmark control schemes 109
4.3 Numerical Simulations and analysis 110
4.3.1 Case Study on steady-state cornering 111
4.3.2 Case Study on Step Steer 112

4.3.3 Case Study on Brake in a Turn 112
4.3.4 Case Study on high-frequency driving manoeuvres 113
4.4 Conclusions 118

Chapter 5. Feedforward PID Control of Full-Car with PALS for Improved Chassis Attitude stabilisation **120**
5.1 Introduction 120
5.2 Development of tire force compensation model 121
5.2.1 Nonlinear simulation fit based compensation model 122
5.3 Control Methodology Development 124
5.3.1 PID control ('PALS-PID') 125
5.3.2 Nonlinear Feedforward PID ('FF-PID-non') 126
5.4 Numerical Simulations with nonlinear multi-body model and analysis 127
5.4.1 Step Steer 128
5.4.2 Steady State Cornering 128
5.4.3 Brake in a turn 130
5.4.4 Pure longitudinal acceleration and braking 130
5.4.5 Fishhook 132
5.4.6 Continuous sinusoid steer 134
5.5 Conclusion 135

Chapter 6. Improved ride comfort and road holding through LMI-based robust MPC for a quarter-car model with SAVGS **137**
6.1 Introduction 137
6.1.1 Notation 138
6.2 Suspension model and design requirements 138
6.2.1 Quarter Car SAVGS linear equivalent model 139
6.2.2 Quarter Car SAVGS Uncertain system 139
6.2.3 Objectives and constraints requirements 142
6.3 Robust Model Predictive Control Design 142
6.3.1 System Description 143
6.3.2 Problem formulation 144
6.4 Overall control scheme 150
6.4.1 PI control to solve the single link drifting 150
6.4.2 Selection of the disturbance in Robust MPC design 153

6.4.3 Constraint conversion between nonlinear high fidelity model and linear equivalent model 153
6.5 Numerical Simulations and analysis 155
6.5.1 Simulation With Harmonic Road 156
6.5.2 Simulation With Smoothed Bump and Hole 157
6.5.3 Simulation With Random Road 159
6.6 CONCLUSIONS 160

Chapter 7. Conclusions and Future Work **164**
7.1 Conclusions 165
7.2 Future work 166

Bibliography **168**

List of Figures

1.1 The PALS (left) and the SAVGS (right) application to a quarter-car model with a double wishbone suspension 30

2.1 Passive, Semi-active and Active Quarter Car Model 36

2.2 Simplified two DOF quarter-car (left), four DOF half-car (center) and seven DOF full-car (right) models. The particular case of an actuator in series with a passive spring-damper is shown in this figure. 42

2.3 SAVGS application to a quarter-car double-wishbone suspension [4]. . 44

2.4 PALS application to a quarter car double-wishbone suspension [22]. . 45

2.5 (a) Transformation between the linear equivalent and multi-body models of the SAVGS quarter car; (b) Schematic of the SAVGS quarter-car model. 49

2.6 Function α for the conversion between the actual rotary single-link speed (ω_{SL}) and the linear equivalent actuator speed ($\Delta \dot{z_{lin}}$) with quarter-car SAVGS. 50

2.7 (a) Transformation between the linear equivalent and multi-body models of the PALS quarter-car; (b) Schematic of the SAVGS quarter car model. 51

2.8 Function β for the conversion between the rotary actuator torque (T_{RC}) and the linear equivalent actuator force (F_{RC}) with quarter-car PALS. 52

2.9 Linear equivalent model of SAVGS full car [24, 25].M_s is the sprung mass, T_p and T_r are the chassis pitch and roll disturbance moments respectively, z_{lini} are the linear equivalent actuator displacements at each corner, θ and ϕ are the pitch and roll angles respectively, and the z variables denote linear vertical displacements of the points/masses indicated, while the rest of the symbols are defined in Table 2.2. . . . 52

2.10 Conversion between linear equivalent and multi-body models of the SAVGS full car. . . . 53

2.11 Linear equivalent model of PALS full car. F_{RCi} are the linear equivalent actuation forces at each corner, while the rest of the symbols are defined in the subsection 2.2.4.3. . . . 55

2.12 Conversion between linear equivalent and multi-body models of the PALS full car. . . . 56

2.13 Schematic of the steady-state PALS-retrofitted full-car model. . . . 57

2.14 PSD estimate of the random-road profiles, with roughness A to C considered in this thesis shown in blue, green and red lines, corresponding to good, above average and average quality road. . . . 62

2.15 Multi-objective PID chassis attitude control scheme for the SAVGS full car [2]. . . . 63

2.16 Skyhook control in a linear equivalent quarter-car model [36]. . . . 65

2.17 A generalised regulator. P corresponds to a time-invariant state-space representation of a linear plant, K to the related synthesised controller, $\mathbf{w}$ to exogenous disturbance signals, $\tilde{\mathbf{z}}$ to the error signals to be minimised, $\mathbf{u}$ to the control input, and $\mathbf{y}$ to the system measurements for feedback. . . . 66

2.18 (a) An extended generalised regulator for μ-synthesis, and (b) the analysis framework [40]. Δ is a structured uncertainty block diagonal matrix. . . . 68

2.19 Configuration of the adaptive neural network-based robust control for active suspension.[53] 71
2.20 Preview control in active suspension, equipped with advanced camera [57]. 72
2.21 Configuration of the frequency-biased multi-objective control scheme in the PALS-retrofitted full car [5]. 73
2.22 The structure of an energy-harvesting suspension system [65]. 74

3.1 Nonlinear (solid) and linearised (dashed) characteristics of damper force versus damper velocity for the damper units installed at the front (black) and rear (red) axles for the GT with SAVGS full car[24]. 78
3.2 Nonlinear (solid) and linearised (dashed) characteristics of damper force versus damper velocity for the damper units installed at the front (black) and rear (red) axles for the SUV with PALS full car. . . 79
3.3 Generalised regulator. P corresponds to a time-invariant state-space representation of a linear plant, K to the synthesised controller, $\mathbf{w}$ to exogenous disturbance signals, $\tilde{\mathbf{z}}$ to the cost signals to be minimised, $\mathbf{u}$ to manipulated variables, and $\mathbf{y}$ to the measurements feedback. . . 80
3.4 Interconnection for H_∞ control for the GT with SAVGS full car, where the signals and blocks are explained in (3.6)-(3.15). 82
3.5 μ-synthesis: (a) extended generalised regulator, and (b) analysis framework [40]. P is a time-invariant state-space representation of a linear plant, K is a μ-synthesis based controller, Δ is a structured uncertainty block diagonal matrix, $\mathbf{w}$ correspond to system exogenous disturbances, and $\tilde{z}$ to the cost signals to be minimised. 86
3.6 Interconnection for μ-synthesis control for the SUV with PALS full car. 90
3.7 Numerical simulation results in the case of $M_s = M_{\text{nom}}$ for the GT with SAVGS full car: the PSD of $\ddot{z}_s$, $\ddot{\theta}_s$ and $\ddot{\phi}_s$ with the H_∞ and different μ-synthesis controllers when the vehicle is running over ISO random road class C at a constant forward speed of 100 km/h. 94

3.8 Numerical simulation results in the case of $M_s = M_{\text{nom}}$ for the GT with SAVGS full car: the PSD of Δl_{t1} and Δl_{t3} with the H_∞ and different μ-synthesis controllers when the vehicle is running over ISO random road class C at a constant forward speed of 100 km/h. 95

3.9 Numerical simulation results in the case of $M_s = M_{\text{max}}$ for the GT with SAVGS full car: the PSD of $\ddot{z}_s$, $\ddot{\theta}_s$ and $\ddot{\phi}_s$ with the H_∞ and different μ-synthesis controllers when the vehicle is running over ISO random road class C at a constant forward speed of 100 km/h. 97

3.10 Numerical simulation results in the case of $M_s = M_{\text{max}}$ for the GT with SAVGS full car: the PSD of Δl_{t1} and Δl_{t3} with the H_∞ and different μ-synthesis controllers when the vehicle is running over ISO random road class C at a constant forward speed of 100 km/h. 98

3.11 Numerical simulation results in the case of $M_s = M_{\text{max}}$ for the GT with SAVGS full car: $\ddot{z}_s$ time histories for the passive, H_∞-controlled and $\mu_{combined}$-controlled systems when the vehicle is running over ISO random road class C at a constant forward speed of 100 km/h. 99

3.12 The PSD gain of $\ddot{z}_s$ at the frequency of 2 Hz for different values of M_s (swept from M_{nom} to M_{max} in 30 kg increments) for the GT with SAVGS full car when the vehicle is running over ISO random road class C at a constant forward speed of 100 km/h. The passive system, and H_∞ and different μ-synthesis control performances are compared. 99

3.13 Numerical simulation results: the PSD gain of CMC vertical acceleration ($\ddot{z}_s$), pitch acceleration ($\ddot{\theta}_s$), roll acceleration ($\ddot{\phi}_s$) and tire deflection (Δl_{t1}) with the passive, 'PALS-H_∞' and 'PALS-μ' controllers in the sprung mass, M_s, cases of M_{nom} (top-left), M_{min} (top-right), and M_{max} (bottom-left), and the RMS value variation of $\ddot{z}_s$, $\ddot{\theta}_s$, $\ddot{\phi}_s$ and Δl_{t1} with the passive, 'PALS-H_∞' and 'PALS-μ' controllers for M_s swept from M_{min} to M_{max} in 150kg increments (bottom-right) when the vehicle is running over ISO random road class C at a constant forward speed of 100 km/h. 101

3.14 Numerical simulation results: the PSD gain of CMC vertical acceleration ($\ddot{z}_s$), at the frequency of 4 Hz for different values of M_s (swept from M_{min} to M_{max} in 150 kg increments) when the vehicle is driven over an ISO random road Class C at 100 km/h, for different cases of suspension control. 103

3.15 Numerical simulation results: the variation of CMC vertical acceleration ($\ddot{z}_s$), pitch acceleration ($\ddot{\theta}_s$), tire deflection (Δl_{t1}) and power consumption in the DC batteries ($P_{battery}$) with the passive, 'PALS-H_∞' and 'PALS-μ' controllers in the sprung mass, M_s, cases of M_{nom} (top-left), M_{min} (top-right), and M_{max} (bottom-left), and the RMS value variation of $\ddot{z}_s$, $\ddot{\theta}_s$, Δl_{t1} and $P_{battery}$ with the passive, 'PALS-H_∞' and 'PALS-μ' controllers for M_s swept from M_{min} to M_{max} in 150kg increments (bottom-right) when the vehicle is running over a bump of 0.05 m height and 2 m length at a constant forward speed of 20 km/h. 104

4.1 Configuration of the multi-objective blended control scheme ('PALS-PID-μ') in the PALS-retrofitted full car. 109

4.2 Numerical simulation results for the SUV with PALS full car nonlinear model: the chassis roll angle (ϕ) for the M_{nom} case when the vehicle is undergoing an ISO steady-state cornering at 100 km/h, for different cases of active suspension control. 111

4.3 Numerical simulation results for the SUV with PALS full car nonlinear model: the chassis roll angle (ϕ) and total power consumption in the DC batteries ($P_{battery}$) for the M_{nom} case when the vehicle is undergoing an ISO step steer at 100 km/h, for different cases of active suspension control. 113

4.4 Numerical simulation results: the chassis pitch angle (θ) and chassis roll angle (ϕ) for the M_{nom} case when the vehicle is undergoing an ISO brake in turn at initial longitudinal speed 80 km/h, for different cases of active suspension control. 114

4.5 Numerical simulation results: the time-domain value of CMC vertical acceleration ($\ddot{z}_s$), pitch acceleration ($\ddot{\theta}$), tire deflection Δl_{t1} and power consumption in the DC batteries ($P_{battery}$) for the M_{nom} case when the vehicle is driven over an ISO speed bump at 20 km/h, for different cases of suspension control. 115

4.6 Numerical simulation results: the PSDs of CMC vertical acceleration ($\ddot{z}_s$), pitch acceleration ($\ddot{\theta}$), roll acceleration ($\ddot{\phi}$) and tire deflection Δl_{t1} for the M_{nom} case when the vehicle is driven over an ISO random road Class C at 100 km/h, for different cases of suspension control. . . 117

4.7 Numerical simulation results: the total power consumption in the DC batteries ($P_{battery}$) in a 2.5 s time history for the M_{nom} case when the vehicle is driven over an ISO random road Class C at 100 km/h, for different cases of active suspension control. 117

4.8 The average value variation of total power consumption in the DC batteries when the vehicle is driven over an ISO random road Class C at 100 km/h and M_s is swept from $M_{\min}$ to $M_{\max}$ in 150 kg increments, for the cases of 'PALS-H_∞','PALS-μ' and 'PALS-PID-μ' controllers. . 118

4.9 Numerical simulation results: the RMS value performance improvement of CMC vertical acceleration ($\ddot{z}_s$), pitch acceleration ($\ddot{\theta}$), roll acceleration ($\ddot{\phi}$) and tire deflection (Δl_{t1}), as a percentage of the passive case performance, in the sprung mass, M_s, cases of M_{nom} (top), $M_{\min}$ (middle), and $M_{\max}$ (bottom) when the vehicle is driven over an ISO random road Class C at 100 km/h, for different cases of suspension control. The precise calculation of the height of the bars is $\frac{\text{metric}_{\text{passive}}-\text{metric}_{\text{active}}}{\text{metric}_{\text{passive}}}$, where 'metric' is the RMS value of one of $\ddot{z}_s$, θ, ϕ, and Δl_{t1}, and 'active' is one of the active suspension controller cases. 119

5.1 Vertical tire force increment (ΔF_{tzi}) polynomial fitting with respect to the lateral acceleration (a_y) in the steady state cornering manoeuvre, where the black solid line corresponds to the nonlinear simulation ΔF_{tzi} data and the blue dashed line to the third order polynomial fitting line. 123

5.2 Vertical tire force increment (ΔF_{tzi}) linear fitting with respect to the longitudinal acceleration (a_x) in the constant deceleration manoeuvre, where the black circles correspond to the nonlinear simulation ΔF_{tzi} data and the blue dashed line to the first order polynomial fitting line 123

5.3 Vertical tire force increment (F_{tzi}) in the ISO steady-state cornering manoeuvre as compared to initial state (100 km/h straight line driving manoeuvre) versus time: the blue line depicts the case without using compensation model, the green line depicts the case with steady state compensation model and the black dashed line depicts the case with nonlinear simulation fit model. 124

5.4 Vertical tire force increment (F_{tzi}) in the ISO brake in turn manoeuvre as compared to initial state (80 km/h straight line driving manoeuvre) versus time: the blue line depicts the case without using compensation model, the green line depicts the case with steady state compensation model and the black dashed line depicts the case with nonlinear simulation fit model. 124

5.5 Multi-objective PID control implementation in the PALS-retrofitted full car. [5, 21] 126

5.6 'FF-PID-non' control implementation in the PALS-retrofitted full car with PID block defined in Figure 5.5. 127

5.7 Numerical simulation results for the SUV with PALS full car: the chassis roll angle (ϕ) and front left corner rocker torque (T_{RC_1}) when the vehicle is undergoing an ISO step steer at 100 km/h, for different methods of suspension control. 129

5.8 Numerical simulation results for the SUV with PALS full car: the chassis roll angle (ϕ) when the vehicle is undergoing an ISO steady-state cornering, for different cases of active suspension control. 129

5.9 Numerical simulation results: the chassis pitch angle (θ), chassis roll angle (ϕ), rocker torque of front left corner (T_{RC_1}) and rear left corner (T_{RC_3}) when the vehicle is undergoing an ISO brake in turn at initial longitudinal speed 80 km/h, for different methods of suspension control. 131

5.10 Numerical simulation results: the forward speed (v_x) and the chassis pitch angle (θ) when the vehicle is undergoing an ISO longitudinal acceleration/deceleration manoeuvre for different methods of suspension control. 132

5.11 Numerical simulation results: the forward speed (v_x), chassis yaw angle (ψ), roll angle (ϕ) and lateral acceleration (a_y) with MES=40 mph (top-left), and MES=50 mph (top-right); and the vertical tire force (F_{tzi}) with with MES=40 mph (bottom-left), and MES=50 mph (bottom-right) when the vehicle performs fishhook manoeuvres for different methods of suspension control. 133

5.12 Numerical simulation results: Ratio of RMS roll angles obtained with different cases of active and passive suspensions when the vehicle performs a sinusoid steering-wheel manoeuvre. 135

6.1 PI incorporated plant model of quarter car SAVGS, where $\bar{\mathbf{d}}$ corresponds to the stack vector for disturbance bound, P' to the new uncertain system with parallel PI incorporated, and $z_{lin}^{(ref)}$ to the exogenous reference signal of linear actuator displacement. 152

6.2 Plot of function α with respect to Δz_{lin} for conversion between multibody and linear equivalent model. 154

6.3 Block diagram of quarter car SAVGS closed-loop control and simulation scheme. 156

6.4 Numerical simulation results (top to bottom): the sprung mass acceleration, tire deflection, suspension deflection and single-link angle, when the quarter car SAVGS is undergoing a harmonic road profile, with 2 Hz frequency and 2.75 cm peak-to-peak amplitude [86], for different cases of active suspension control. 157

6.5 Output torque vs. output speed characteristics of the quarter car SAVGS when it is undergoing a sinusoidal road profile for different cases of active suspension control, with torque-speed operating points and actuator limit boundaries shown in blue solid lines and magenta solid lines, respectively. 157

6.6 Numerical simulation results (top to bottom): the sprung mass acceleration, tire deflection, suspension deflection and single-link angle when the quarter-car SAVGS is running over a smoothed bump (0-2 s) and hole (0-4 s), with 2.75 cm peak-to-peak amplitude in road height, 1.4 m width and 10 km/h driving speed [86] for different cases of active suspension control. 158
6.7 Output torque vs. output speed characteristics when the quarter car SAVGS is undergoing a smoothed bump and hole road profile for different cases of active suspension control, with torque-speed operating points and actuator limit boundaries shown in blue solid lines and magenta solid lines respectively. 159
6.8 Numerical simulation results: the PSD estimate of the sprung mass acceleration (top) and tire deflection (bottom), when the quarter car SAVGS is undergoing random road (Classes A-C) for different cases of active suspension control. 161
6.9 Output torque vs. output speed characteristics when the quarter car SAVGS is undergoing random road profile (class C) for H_∞ control (top) and robust model predictive control (bottom), with torque-speed operating points and actuator limit boundaries shown in blue solid lines and magenta solid lines respectively. 162

List of Tables

2.1 Main Parameters in SAVGS- and PALS- retrofitted quarter car test rig 48
2.2 Main Parameters of Original and SAVGS Retrofitted GT full car, and linear equivalent model (F: Front, R: Rear) 54
2.3 Main Parameters of Original and PALS Retrofitted SUV full car, and linear equivalent model (F: Front, R: Rear) 56

3.1 RMS and peak-to-peak values of the $\ddot{z}_s$, $\ddot{\theta}_s$ and $\ddot{\phi}_s$ with different controllers, $M_s = M_{\text{nom}}$ for the GT with SAVGS full car, when the vehicle is running over ISO random road class C at a constant forward speed of 100 km/h. 95
3.2 RMS and peak-to peak values of the Δl_{t1} and Δl_{t3} with different controllers, $M_s = M_{\text{nom}}$ for the GT with SAVGS full car, when the vehicle is running over ISO random road class C at a constant forward speed of 100 km/h. 96
3.3 RMS and peak-to-peak values of the $\ddot{z}_s$, $\ddot{\theta}_s$ and $\ddot{\phi}_s$ with different controllers, $M_s = M_{\text{max}}$ for the GT with SAVGS full car, when the vehicle is running over ISO random road class C at a constant forward speed of 100 km/h. 96
3.4 RMS and peak-to-peak values of the Δl_{t1} and Δl_{t3} with different controllers, $M_s = M_{\text{max}}$ for the GT with SAVGS full car, when the vehicle is running over ISO random road class C at a constant forward speed of 100 km/h. 98

4.1 PID tuning parameters in 'PALS-PID' 'PALS-PID-H_∞' and 'PALS-PID-μ' control schemes 110

5.1 PID tuning parameters in 'PALS-PID' and 'FF-PID-non' control schemes 127

6.1 RMS values of the $\ddot{z}_s$ and l_t with different controllers (Rand denotes random) 160

Abbreviations

SD:	Spring Damper
SAVGS:	Series Active Variable Geometry Suspension
PALS:	Parallel Active Link Suspension
GT:	Grand Tour
SUV:	Sport Utility Vehicle
PID:	Proportional Integral Differential
RMPC:	Robust Model Predictive Control
LMI:	Linear Matrix Inequality
ADS:	Adaptive Damping System
ABC:	Active Body Control
DOF:	Degrees of Freedom
QC:	Quarter Car
FC:	Full Car
PMSM:	Permanent Magnet Synchronous Machine
UW:	Upper Wishbone
WH:	Wheel
PSD:	Power Spectral Density
OCD:	Overturning Couple Distribution
DC:	Direct Current

T-S: Takagi-Sugeno

SMC: Sliding Mode Control

LQR: Linear Quadratic Regulator

LQG: Linear Quadratic Gaussian

RHC: Receding Horizon Control

NN: Neural Network

SL: Single Link

CMC: Center of Mass of the Chassis

ISO: International Organisation for Standardisation

ICE: Internal Combustion Engine

RMS: Root Mean Square

LSS: Low Speed Shaft

HSS: High Speed Shaft

LFT: Linear Fractional Transformation

PTP: Peak to Peak

MES: Maneuver Entrance Speed

RMPC: Robust Model Predictive Control

RHC: Receding Horizon Control

NN: Neural Network

SL: Single Link

Chapter 1

Introduction

1.1 Background

The conventional passive suspension system equipped with spring-damper (SD) units plays an important role in a car, as it isolates the vehicle's chassis from road disturbances. Over the past decades, with the increasing demand for more efficient systems and growing requirements for high-level ride comfort and better road-handling performance, the innovative concept of active suspension has appeared. Recently, two novel mechatronic suspensions have been proposed, the Parallel Active Link Suspension (PALS) and the Series Active Geometric Suspension (SAVGS), both of which involve electromagnetic actuators and active links. These have proven to be practically feasible in quarter-car studies [1, 2, 3, 4]. The schematics of the PALS and the SAVGS, including their practical implementations in a double wishbone suspension, are shown in Figure. 1.1. In the case of the SAVGS, the active single-link component ('F-G'), which is in series with the end eye of the SD unit and the other end of the link ('G'), is fixed on the chassis. It is driven by a suitable actuator involving a permanent magnet synchronous motor (PMSM) and an epicyclic gearbox, thereby improving the performance of the double-wishbone suspension. In

the case of the PALS, a rocker-pushrod assembly ('K-J-F') is introduced between the sprung (M_s) and unsprung (M_u) masses, in parallel with the conventional SD. An active component, the rocker ('K-J'), which is driven by a rotary actuator, generates the torque (T_{RC}) acting from the chassis onto the lower wishbone to improve the performance of the double-wishbone suspension.

Unlike passive suspension, both the PALS and the SAVGS have features of: i) chassis attitude control; and ii) ride comfort and road-holding enhancement at their frequency of interest. Compared to other active suspensions, both the PALS and the SAVGS have the following advantages: i) remarkable performance enhancement; ii) negligible unsprung mass and small sprung-mass increments; iii) a simplified structure, with the conventional anti-roll bar replaced and its functionality encompassed by active links at each corner of the chassis; and iv) a safer operation (and so on).

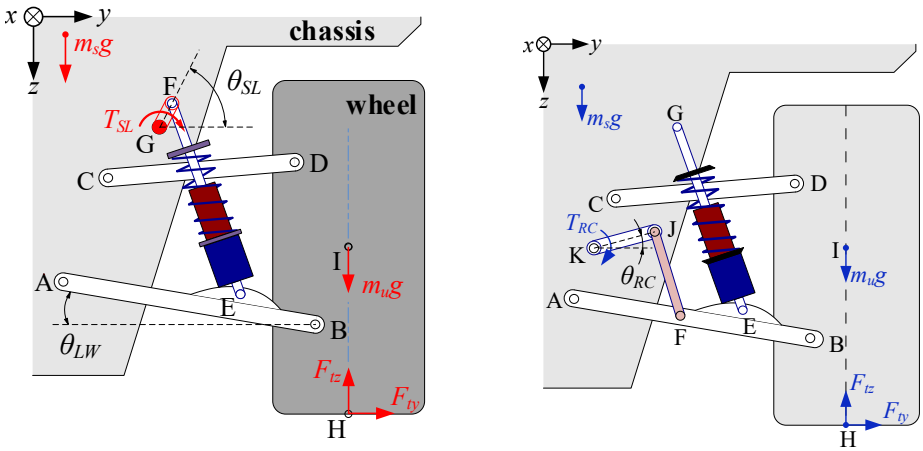


Figure 1.1: The PALS (left) and the SAVGS (right) application to a quarter-car model with a double wishbone suspension

In addition, the PALS and the SAVGS are complementary to each other, as they are advantageous in terms of their respective application to different vehicle categories and different suspension structures. Previous work in [1, 2, 3] has illustrated that the SAVGS is more suitable for medium or light-sized vehicles with stiff suspension springs (e.g. the Grand Tourer [GT]) while the PALS is particularly

advantageous in the heavier vehicles with less-stiff springs (e.g. SUV). The reasons for this, illustrated in [5], can be briefly summarised as follows. First, since the SAVGS acts in series with passive springs, it needs to continuously apply a nominal torque to support the whole of the sprung mass. Hence, the power requirement would become excessive in the SAVGS application to heavier vehicles. Second, there are larger actuator torque requirements if the spring is stiff (e.g, the GT) because the spring is displaced by the parallel arrangement in the PALS while in operation. Therefore, the PALS is less suitable for the GT.

1.2 Aims and Contributions

1.2.1 Research challenges

we now list the most significant challenges encountered when designing effective control methodologies for the vehicle active suspensions that this thesis will address.

1. *the practical structured uncertainties of sprung mass and suspension damping coefficient are not taken into account, which results in the lack of robustness.*

2. *the PID control used in the hybrid schemes has slow response time, which leads to reduced performance and reduced stability in some circumstances*

1.2.2 Research Aims

Previous work of the control methodologies designed for SAVGS and PALS focused on chassis leveling and vibration attenuation with more details shown later in the literature review in Chapter 2. Based on the research challenges, the primary research aims relevant to designing effective control methodologies for the vehicle active suspensions are summarised:

1. *to identify and characterise the uncertainties of the SAVGS/PALS-retrofitted full car that are mainly ignored in the previous robust suspension control design*

2. *to formulate μ-synthesis-based control for the full-car SAVGS and PALS, with their practical uncertainties taken into account, aiming to address their robustness limitation and improve ride comfort and road holding in their high-frequency vehicle dynamics*

3. *to propose a feedforward control strategy for full-car PALS that is combined with the previously developed PID control scheme [5] to address the slow response and stability issue, for the mitigation of pitch and roll motions in the context of low-frequency vehicle dynamics*

Then, the secondary research aims are listed as:

1. *to develop a multi-objective blended full-car PALS control scheme to enable the functions of general (low- and high- frequency) motions under a variable payload*

2. *to propose a RMPC-based solution for quarter-car SAVGS to improve the ride-comfort and road-holding in the high-frequency dynamics and to account for nonlinearities by considering them as uncertainties and disturbances*

1.2.3 Publications

The research results illustrated in the thesis have been published or are currently under review in several archival journals and international conferences. The list of these publications is reported as follows:

- Papers in international journals

1. **Z. Feng**, M. Yu, S. A. Evangelou, I. M. Jaimoukha and D. Dini, "*Mu-synthesis PID Control of Full-Car with Parallel Active Link Suspension Under Variable Payload*" in IEEE Transactions on Vehicular Technology, 2022 doi: 10.1109/TVT.2022.3203610

2. **Feng, Zilin** and Yu, Min and Georgiou, Anastasis and Evangelou, Simos A and Jaimoukha, Imad M and Dini, Daniele, "*Improved ride comfort and road holding through LMI-based robust MPC for a quarter car model of series active variable geometry suspension*" IEEE Transactions on Control Systems Technology), (in preparation)

- papers included in proceedings of international conferences

1. **Feng, Zilin** and Yu, Min and Cheng, Cheng and Evangelou, Simos A and Jaimoukha, Imad M and Dini, Daniele,"*Uncertainties Investigation and μ-Synthesis Control Design for a Full Car with Series Active Variable Geometry Suspension,*" IFAC-PapersOnLine, 53(2), 13882-13889, 2020, https://doi.org/10.1016/j.ifacol.2020.12.901.

2. **Feng Z**, Yu M, Evangelou S, Jaimoukha I, Dini D "*Feedforward PID Control of Full-Car with Parallel Active Link Suspension for Improved Chassis Attitude Stabilization,*" in proceeding of the 6th IEEE Conference on Control Technology and Applications (CCTA), 2022, doi: 10.48550/arXiv.2203.04162

1.3 Thesis Outline

The rest of this thesis will review the main works on robust control methodologies for vehicle active suspension and describe this thesis' contribution to the field. The thesis is structured as follows.

Chapter 2 contains a thorough literature review of state-of-the-art approaches in the field of vehicle suspension systems, together with a brief explanation of the SAVGS and PALS concepts. It provides a review of the literature on the modelling of the multi-body quarter- and full-car nonlinear models and the linearisation of the quarter- and full-car models. A review of recent studies on control approaches to active suspension, taking into account three categories of performance objectives, is also completed.

Chapter 3 proposes a μ-synthesis full-car control design using the SAVGS. The aim of doing so is to enhance the ride comfort and road-holding performance, with two significant practical uncertainties in the sprung mass and the suspension damping taken into account. Numerical simulations with a high-fidelity nonlinear vehicle model are performed and the fixed and swept values of the sprung mass are tested, thereby assessing the control robustness and performance of the developed scheme against both the passive suspension and the H_∞-controlled SAVGS.

Chapter 4 presents a combined μ-synthesis PID control scheme for a full-car control design with the PALS to simultaneously achieve the low-frequency mitigation of attitude motions and the high-frequency vibration suppression of the vehicle.

Chapter 5 proposes the robust model predictive control based solution in the application to a quarter car SAVGS with suspension damping uncertainties taken into consideration in the suspension control design, achieving improvement in terms of the ride comfort and road holding performance.

Chapter 6 proposes a feedforward control strategy for the PALS that is combined with a previously developed PID full-car control scheme, to address the problem of feedback delays in chassis attitude stabilisation.

Finally, in Chapter 7 concluding remarks are discussed and the main areas of future work are outlined.

Chapter 2

Literature Review

This chapter reviews the development of the mechatronic structure, mathematical models, control strategies and experimental testing methods for existing vehicle suspensions.

2.1 Development of the Vehicle Suspension Structure

Systematic research on vehicle suspensions has been carried out since the 1930s, since when a great many suspension structures have been designed to achieve better performance [4]. The main developed and proposed suspensions include double wishbone suspension (1930s) and McPherson strut suspensions (1940s). The advantage of the latter is that it has less sprung mass and occupies a smaller space, while the former (which is focused on and applied in this research on the applications of SAVGS and PALS) is able to guarantee smaller wheel camber angle changes in bump and rebound conditions.

Several suspension designs have been found to achieve the purposes of: i) supporting the chassis; ii) improving ride comfort for passengers; iii) controlling the at-

titude of the vehicle and wheels; and iv) ensuring steerability and manoeuvrability. Some of these are determined by the geometric layout of the axles (e.g., dependent and independent suspensions.) In dependent suspensions, wheels on the same axle are rigidly connected to one another, while in independent suspensions, the motion of each wheel is completely independent from the others. The other suspensions in this thesis are classified into three types according to their force-producing elements: passive suspension; semi-active suspension; and active suspension (Figure 2.1).

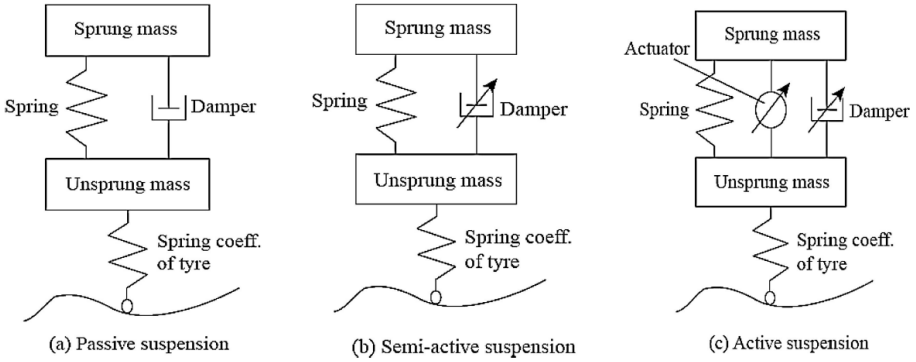


Figure 2.1: Passive, Semi-active and Active Quarter Car Model

2.1.1 Passive Suspension

The passive suspension system is a conventional suspension system made of coil springs and shock absorbers that are mounted in parallel at each of the vehicle's wheels. The choice of SD units relies on their application and the predicted driving conditions [4]. The purpose of the spring is to support the vehicle body; it is used to simultaneously absorb and store energy, while the damper or shock absorber dissipates the stored energy in the spring and prevents excessive oscillation by controlling the input from the road that is transmitted to the vehicle. [6] represents a preliminary optimisation study of the possible benefits of the novel mechanical

elements (i.e. the inerter) which cannot be achieved by conventional passive struts in vehicle suspension systems. In general, this type of system has been widely used in automotive applications due to its low cost and simple implementation. However, it can only passively adapt to the road profile and therefore cannot maintain best performance due to the fact that its elements' (the spring and damper's) values are not tune-able. Hence, the passive suspension system can optimise ride and stability to some degree, but cannot eliminate the conflict between them. With the development of new control techniques and growing demand for more efficient suspension, innovative suspension systems started to appear. These offer greater freedom to optimise the variety of performance requirements.

2.1.2 Semi-Active Suspension

Semi-active (sometimes referred to as variable damper) suspensions typically include the same force-producing elements as passive suspensions, with the main difference being that the damping coefficient of the shock absorber can be actively adjusted by a control unit. Hence, the mechanical layout of a semi-active suspension is identical to that of a passive one. Switching between the damper characteristics, a reaction force can be produced. Semi-active suspension systems require less compromise between ride comfort and handling than passive suspension systems and consume far less power than active suspension systems. However, the possibility of improvement in terms of ride comfort and road holding (given the increased power consumption) is rather limited compared to that offered by active suspension [4].

2.1.3 Active Suspension

In addition to the SD units found in the passive and the semi-active suspension systems, an actuator is introduced in the active suspension system; this is either in

series (SAVGS) or in parallel (PALS) to the aforementioned SD unit of the passive suspension, providing external force (energy) to the system and thereby improving its dynamic behaviour. Therefore, an active suspension system can adjust its suspension parameters in different circumstances, responding to irregularities and disturbances and thereby reaching a desired combination of ride comfort and road-handling performance. These extra features come at the price of more complexity, higher costs and power consumption, and inconvenient maintenance requirements. Prior research reported in [3, 4, 7] demonstrates the suitability and performance of the SAVGS in a light to medium-sized vehicle with stiff suspension springs (e.g., the GT). The SAVGS is particularly advantageous in this category compared to other possible suspension topologies (e.g., those with actuators acting in parallel to the spring), while the PALS is not suited, being more appropriate to heavier vehicles with less stiff springs (e.g., SUVs). The reasons for this are as follows: i) the 'series' active-link/SD configuration is deemed to be especially suitable for the GT, which has a light-to-medium chassis weight and stiff suspension springs; ii) the system demands much larger torque and power from a link-driving actuator when applied to a heavy car such as an SUV; and iii) the parallel arrangement of the rocker-pushrod assembly can deal with a heavier chassis weight suspended by less stiff springs and with lower actuator requirements and power consumption. In terms of the choice of actuator, commonly-used hydraulic actuators are being gradually replaced by electromechanical ones, since they guarantee a faster response and are more easily implemented.

2.1.4 State-of-the-Art Active Suspension

The main suspension technologies used commercially, beyond the widely used passive suspensions, include air springs (air suspension), and other advanced active suspension systems such as Mercedes' active body control and Audi's predictive

active suspension. These suspensions are developed with the aim of continuously pursuing the achievement of improved suspension performance, concise structures, low energy costs and high reliability in the process of vehicle and transportation electrification.

2.1.4.1 Air-spring Suspension

Air suspension replaces the steel springs between the wheels and the chassis with airbags in heavy vehicle applications such as buses and trucks, as well as in some passenger cars [8, 9, 10]. The pressure of the air can be adjusted using an electric or engine-driven air pump or compressor, enabling the car's height to be changed along with the driving feel: a softer airbag can add more comfort, while a firmer one can make a car sportier to drive. This adjustment may be carried out automatically or by pressing a button inside the car. Unlike hydropneumatic suspension, which offers many similar features, air suspension does not use pressurised liquid; rather, it uses pressurised air. The air pressure inflates flexible bellows which are usually made from textile-reinforced rubber, and raises the chassis from the axle [11]. As with variable dampers (by which the damping can be varied), the spring stiffness in the air suspension can be varied by reservoir systems that may be fully adjustable (that is, being able to adjust each wheel's air pressure individually). Although air suspension is generally regarded as one of the best advancements in car technology in recent years, it only tends to be available on more expensive cars, particularly tall SUVs. This is because it costs more to make than traditional suspension components such as springs; additionally air suspension systems are more expensive to replace.

Air suspension is increasingly being used in passenger cars, as in the following examples. i) The Mercedes-Benz airmatic suspension benefits from the use of adjustable air springs in combination with an adaptive damping system (ADS), which sharpens handling through instant adjustments to the shock absorbers [12].

Mercedes-Benz models equipped with airmatic suspension systems also have 'Sport' and 'Comfort' driving modes, which can be selected by drivers based on their preferences; these modes are equipped on various models, including the CLS Coupe, S-Class, S-Class Maybach, GLE Coupe and GLS SUV. [13]. ii) The Audi adaptive air suspension system, working in combination with controlled damping, offers a wide range of rides, ranging from smooth cruising to sporty handling. Depending on the speed and the driver's preferences, the system adjusts the ride height according to the road conditions. The air suspension also offers level control as a function of load; this is equipped on various models, including the A8, A6 Allroad, A6, Q5 and Q7 [14, 15]. iii) The BMW Adaptive two-axle air suspension ensures extremely comfortable driving with great driving dynamics. The air suspension automatically keeps the vehicle at a constant height, regardless of the load, so that ground clearance and spring travel reserves are maintained even at maximum load. At higher speeds, the vehicle automatically lowers, thereby reducing drag and fuel consumption. In addition, the vehicle can be raised manually or lowered automatically at the touch of a button, making it easier to get in and out or to load the luggage compartment. iv) Tesla Motors offers an 'Active Air Suspension' on the Model S and Model X. This lowers or raises the vehicle for aerodynamic purposes [16].

2.1.4.2 Mercedes' Active Body Control

Active Body Control, (ABC), is the Mercedes-Benz brand name used to describe their hydraulic fully active suspension. It allows control of vehicle-body motions and therefore virtually eliminates body roll in many driving situations, including cornering, accelerating and braking. In the ABC system, four level sensors (one at each wheel) measure the ride level of the vehicle: three accelerometers measure the vertical body acceleration, while one acceleration sensor measures the longitudinal and one sensor measures the transverse body acceleration. At each hydraulic cylin-

der, a pressure sensor monitors the hydraulic pressure; the computer detects body movement from sensors located throughout the vehicle and controls the action of the active suspension through the use of hydraulic servomechanisms. This allows the driver to adjust the suspension and thereby maintain a more level ride in more demanding driving conditions.[17, 18]

2.1.4.3 Audi's Predictive Active Suspension

The Audi A8's predictive suspension works in tandem with a front-mounted camera that is able to detect uneven surfaces before the vehicle actually drives over them. This prepares the car by pre-adjusting the suspension for maximum comfort. The camera is so fast that it gathers information about the road surface up ahead 18 times a second, while the active suspension can lower or lift the car's body by up to 85 mm within five-tenths of a second. The predictive suspension comes with a benefit even when the car is standing still, as it automatically raises the body by as much as 50 mm when the door handle is used, thereby enabling an easier entrance. [19]

2.2 Vehicle Modelling

The most frequently found models in the literature for control synthesis and the dynamic analysis of suspension systems are simplified ones relating to the vertical dynamics of the car, such as quarter-car, half-car, and full-car linear models (Figure 2.2).

The quarter-car model is a simplified linear model of a quarter of a car with either one or two degrees of freedom (DOFs) of sprung mass and unsprung mass vertical displacement. It emphasises the ride dynamics reasonably well [20] and provides a simple description of the active suspension control design.

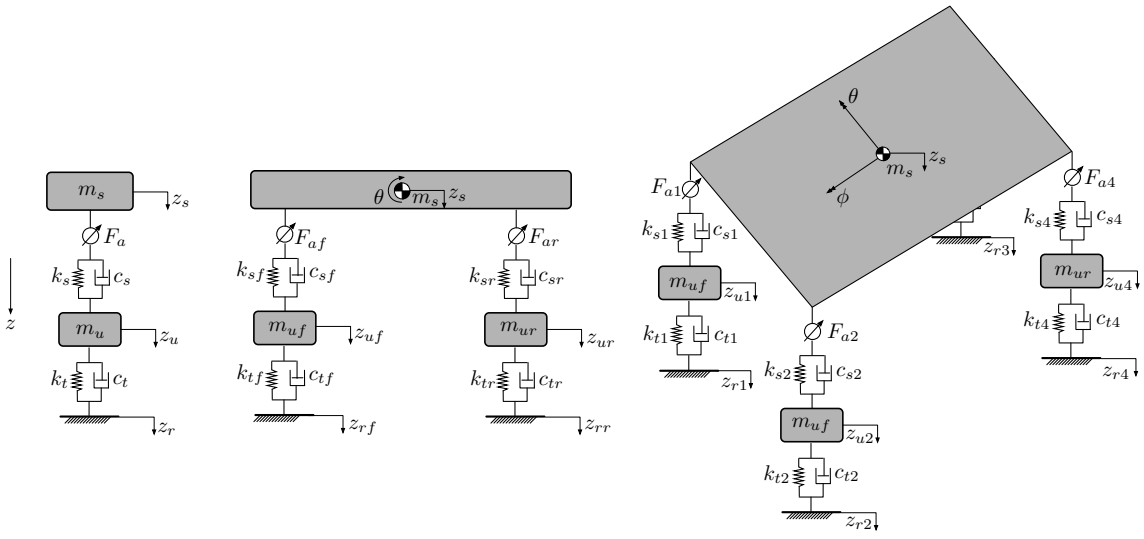


Figure 2.2: Simplified two DOF quarter-car (left), four DOF half-car (center) and seven DOF full-car (right) models. The particular case of an actuator in series with a passive spring-damper is shown in this figure.

2.2.1 Computer Software

A symbolic multi-body software Autosim has been used to build the quarter- and full-car vehicle models. In the latter case, it writes the simulation code via C, Fortran or C-MEX programs containing all the resulting equations of motion , which are then included into a Simulink block as an S-function containing its state-space representation.

2.2.2 Quarter-Car Nonlinear Multi-body Model

In this subsection, the nonlinear multi-body SAVGS- and PALS-retrofitted quarter-car models are reviewed. Then, the nonlinear multi-body SAVGS- and PALS-retrofitted full-car models are reviewed. The selection of their suspension parameters are detailed in the Table 2.1. The nonlinear multi-body quarter-car model has been defined in AutoSim; it extends the conventional quarter car to include a double-wishbone geometric arrangement. The suspension involves a sprung mass that is allowed to move vertically and an unsprung mass that is connected to it via a massless double-wishbone kinematic linkage. A road-tire compression force F_{tz}, which is proportional to the tire deflection, acts on the unpsrung mass to support the overall mass of the quarter car and thereby introduce the road forcing. The nonlinearities (for example, the damping force against the SD compression/extension velocity) are built based on lookup tables.

2.2.2.1 SAVGS-retrofitted Quarter-car Model

As shown in Figure 2.3, the main components of a nonlinear SAVGS model, consisting of the single-link and its driving actuator and gearbox, are also integrated, completing the SAVGS retrofit in the quarter-car model [3, 7, 21].

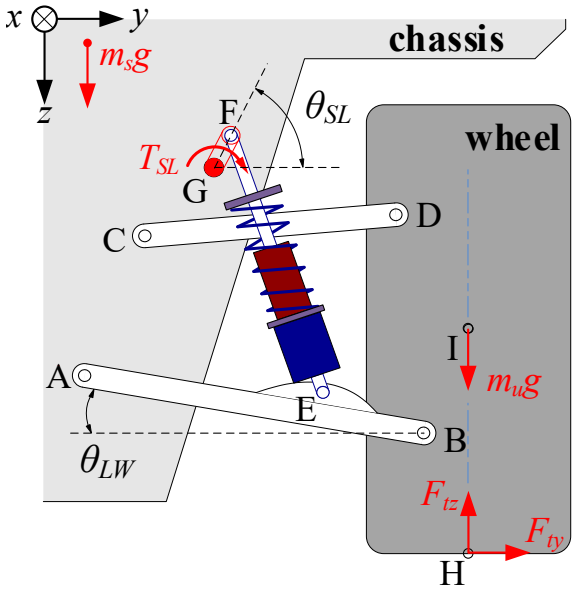


Figure 2.3: SAVGS application to a quarter-car double-wishbone suspension [4].

2.2.2.2 PALS-retrofitted Quarter-car Model

As shown in Figure 2.4, the main components of a nonlinear PALS model, consisting of the rocker-pushrod assembly and its actuator and gearbox, are then integrated to complete the PALS retrofit in the quarter-car model.

2.2.3 Full-Car Nonlinear Multi-body Model

The nonlinear multi-body model of the full car considered in this thesis has been developed in [21] and it is briefly summarised here. The characteristics of a 6 degree of freedom (DOF) chassis, spinning wheels, powertrain elements (internal combustion engine, transmission gearbox, propeller shaft and differential mechanism), pinion-rack steering system, breaking system, passive suspension assembly, wheel tire force and moment system are mathematically described. Furthermore, PID controllers are synthesised separately for closed-loop longitudinal control, which coordinates the gas and braking pedal positions, and lateral control that corresponds

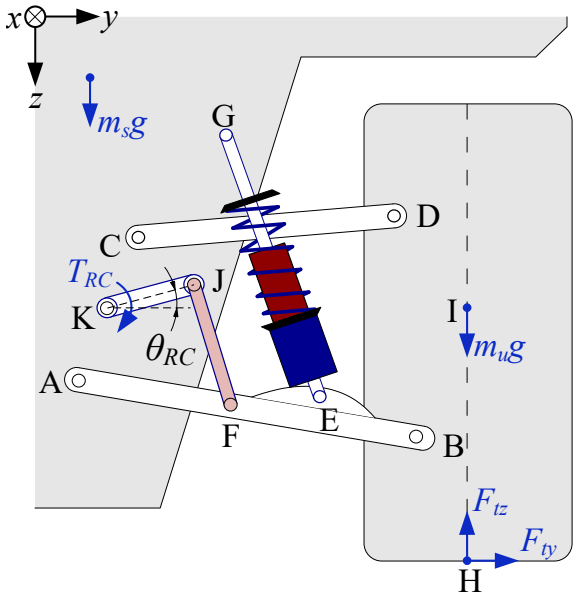


Figure 2.4: PALS application to a quarter car double-wishbone suspension [22].

to steering column position manipulation to implement various ISO-defined driving manoeuvres.

Previous research in [22] suggests the suitability and performance of the PALS for heavy vehicles (for example, SUVs) with less stiff springs, as compared to, for example, high performance cars. The PALS is especially advantageous in this vehicle type as compared to other kinds of vehicle suspension (for example, with actuators acting in series to the spring, such as in the SAVGS) due to less energy consumption and actuation torque requirements. The reason is that the parallel arrangement in the PALS displaces the passive suspension spring directly while operating. Therefore, if the spring is stiff, such as in a high performance car, there are larger actuator torque requirements than if the spring is softer, as in a SUV. This makes the PALS less suitable for a high performance car, whereas in the SAVGS case the stiff spring of a high prerformance car is beneficial [1, 4, 7].

2.2.3.1 SAVGS-retrofitted Full-car Model

As in the description in subsection 2.2.2.1, the full-car SAVGS installs the quarter-car retrofit at the four corners. The major parameters of the GT car with SAVGS are given later in Table 2.2.

2.2.3.2 PALS-retrofitted Full-car Model

As in the description in subsection 2.2.2.2, the full-car PALS installs the quarter-car retrofit at the four corners. The rocker-pushrod assembly at each corner is optimised following the procedure proposed in [22] to maximise the influence from rocker torque to the increment of the vertical tire force. The major parameters of the SUV both with passive suspension and PALS are given in Table 2.3

2.2.4 Linear Equivalent Model with SAVGS and PALS

To enable the linear robust control synthesis, quarter-car linear equivalent models are derived respectively for the SAVGS and PALS, while the full-car SAVGS/-PALS linear equivalent models are derived as the extension to the quarter-car linear equivalent models. Two vehicles representative of the Grand Tourer (GT) and full size Sports Utility Vehicle (SUV) classes have been considered in order to explore the SAVGS and PALS capabilities respectively. Their parameters and values are detailed in the Table 2.2 and Table 2.3.

2.2.4.1 Linear Equivalent Model of the Quarter-car SAVGS

The SAVGS quarter-car linear equivalent model derived in [3, 4] and shown in Figure 2.5 is summarised here. The equivalent model is generated in AutoSim by linearising at the trim state (single-link angle variation $\Delta\theta_{SL} = 90^{\circ}$) of the nonlinear

quarter-car SAVGS multi-body model illustrated in Sec. 2.2.2.1. The suspension's geometric nonlinearities are associated with the single-link angle variation lumped into the function α for the conversion (ω_{SL}) between the actual rotary single-link speed and the linear equivalent actuator speed ($\Delta \dot{z_{lin}}$) (as plotted in 2.6, such that it continues to be accurate for a large range of operating conditions. Therefore, with the derived equivalent spring stiffness and damping coefficient [4], the state-space equations of the quarter-car SAVGS linear equivalent model are constructed as follows:

$$\begin{aligned} m_s\ddot{z}_s &= k_{eq}(\Delta l_s - \Delta z_{lin}) + c_{eq}(\dot{l}_s - \dot{z}_{lin}) \\ m_u\ddot{z}_u &= -k_{eq}(\Delta l_s - \Delta z_{lin}) - c_{eq}(\dot{l}_s - \dot{z}_{lin}) + k_t\Delta l_t + c_t\dot{l}_t. \end{aligned} \tag{2.1}$$

where the system state and the outputs and inputs are given respectively as follows:

$$\begin{aligned} x &= [\dot{z}_s, \dot{z}_u, \Delta l_s, \Delta l_t, \Delta z_{lin}]^T, \\ y &= [\ddot{z}_s, \Delta l_s, \Delta l_t]^T \\ u &= [\dot{z}_r, \dot{z}_{lin}]^T \end{aligned} \tag{2.2}$$

in which: $\dot{z}_{lin}$ is the derivative of the linear equivalent actuator displacement of the quarter-car SAVGS.

2.2.4.2 Linear Equivalent Model of the Quarter-car PALS

The PALS quarter-car linear equivalent model shown in Figure 2.7 is summarised here. The equivalent model of the PALS quarter car is independent of the rotation angle $\Delta\theta_{RC}$, with the geometric nonlinearities lumped in function β for the conversion between the rotary actuator torque (T_{RC}) and the linear equivalent actuator force (F_{RC}) as plotted in 2.8.

With the parameters of equivalent spring stiffness ($k_{SD}^{(eq)}$) and damping coefficient ($c_{SD}^{(eq)}$) derived in [22], the linear equivalent PALS quarter-car model can be

Table 2.1: Main Parameters in SAVGS- and PALS- retrofitted quarter car test rig

Parameters	Value
SAVGS-retrofitted quarter car test rig [4]	
Weight of sprung mass	320 kg
Weight of unsprung mass	49 kg
Spring stiffness	157614 $\frac{N}{m}$
Damping coefficient	5792 $\frac{Ns}{m}$
Tire stiffness	275000 $\frac{N}{m}$
Tire damping coefficient	300 $\frac{Ns}{m}$
Single-link length	11 mm
Peak-to-peak road height	27.5 mm
PALS-retrofitted quarter car test rig [23]	
Weight of sprung mass	320 kg
Weight of unsprung mass	50 kg
Spring stiffness	157614 $\frac{N}{m}$
Damping coefficient	5792 $\frac{Ns}{m}$
Tire stiffness	275000 $\frac{N}{m}$
Tire damping coefficient	300 $\frac{Ns}{m}$
Rocker length	74.2 mm
Pushrod length	147.9 mm

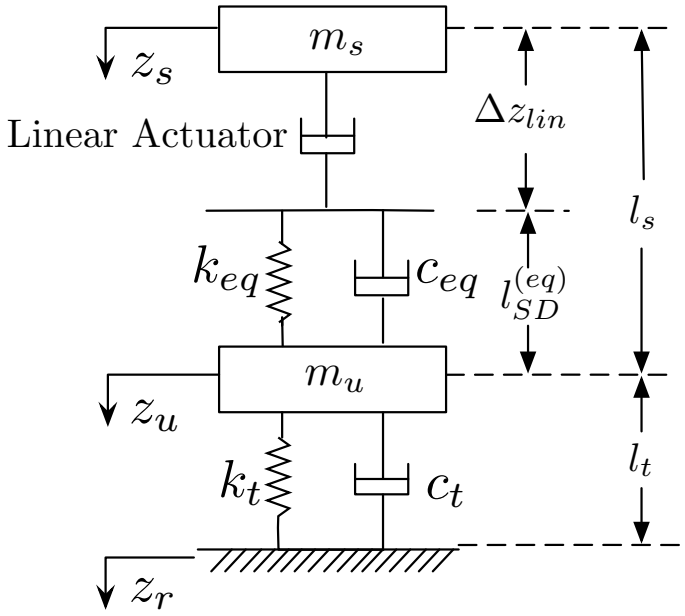
constructed as follows:

$$\begin{aligned} m_s\ddot{z}_s &= k_{SD}^{(eq)}\Delta l_s + c_{SD}^{(eq)}\dot{l}_s - F_{RC} \\ m_u\ddot{z}_u &= -k_{SD}^{(eq)}\Delta l_s - c_{SD}^{(eq)}\dot{l}_s + k_t\Delta l_t + c_t\dot{l}_t + F_{RC}. \end{aligned} \tag{2.3}$$

where the system state and the outputs and inputs are given respectively as follows:

$$\begin{aligned} x &= [\dot{z}_s, \dot{z}_u, \Delta l_s, \Delta l_t]^T, \\ y &= [\ddot{z}_s, \Delta l_s, \Delta l_t]^T \\ u &= [\dot{z}_r, F_{RC}]^T \end{aligned} \tag{2.4}$$

in which: F_{RC} is the linear equivalent actuation force of the quarter-car PALS.



(b)

Figure 2.5: (a) Transformation between the linear equivalent and multi-body models of the SAVGS quarter car; (b) Schematic of the SAVGS quarter-car model.

2.2.4.3 Linear Equivalent Model of the Full-car SAVGS

To enable the linear robust control synthesis, a linear equivalent model of the SAVGS full car described in [24], as shown in the schematic of the full car in Figure 2.9, is employed and summarised here. This model lumps the suspension geometric nonlinearities at each corner such that it continues to be accurate for a large range of operating conditions. Its state space representation can be obtained as follows:

$$\begin{aligned} \dot{x} &= Ax + Bv, \\ y &= Cx + Dv, \end{aligned} \tag{2.5}$$

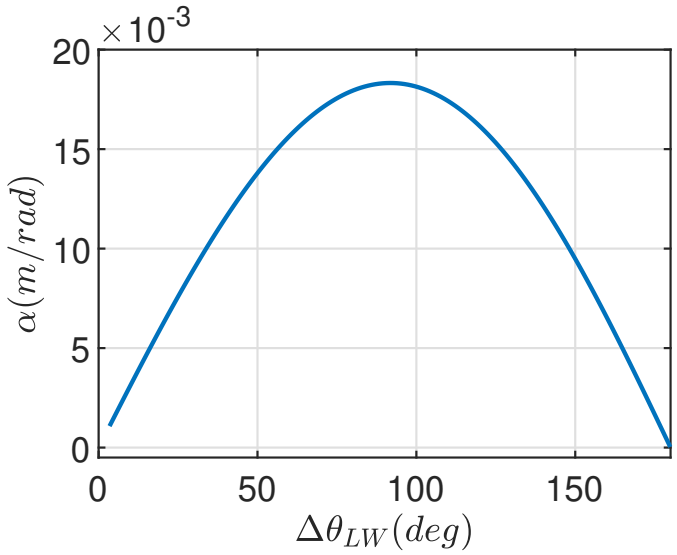
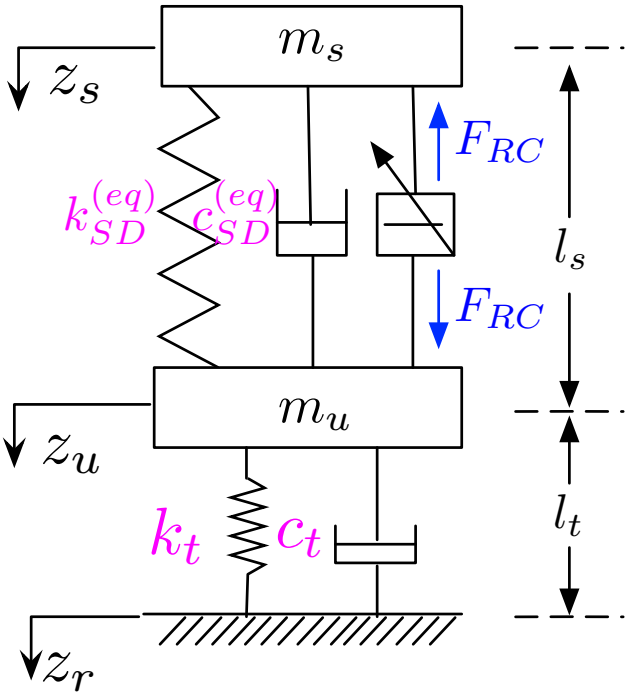


Figure 2.6: Function α for the conversion between the actual rotary single-link speed (ω_{SL}) and the linear equivalent actuator speed ($\Delta\dot{z_{lin}}$) with quarter-car SAVGS.

where $x = [\dot{z}_s, \dot{\theta}, \dot{\phi}, \boldsymbol{\dot{z}_u}^T, \Delta\boldsymbol{l_s}^T, \Delta\boldsymbol{l_t}^T, \boldsymbol{z_{lin}}]^T$ is the system state, in which: a) $\dot{z}_s$ is CMC (center of the mass of the chassis) vertical velocity, b) $\dot{\theta}$ and $\dot{\phi}$ are pitch and roll velocities of the chassis respectively, c) $\boldsymbol{\dot{z}_u} = [\dot{z}_{u1}, \dot{z}_{u2}, \dot{z}_{u3}, \dot{z}_{u4}]^T$ are the vertical velocities of the unsprung masses (m_u) at each wheel, d) $\Delta\boldsymbol{l_s} = [\Delta l_{s1}, \Delta l_{s2}, \Delta l_{s3}, \Delta l_{s4}]^T$ are the suspension deflections at the four corners (for example, $\Delta l_{s1} = z_{u1} - z_1$, where the vertical position of the sprung mass at each wheel z_i is linearised and approximated as:

$$\begin{aligned} z_1 = z_s - b_f\theta - \frac{t_f}{2}\phi, z_2 = z_s - b_f\theta + \frac{t_f}{2}\phi, \\ z_3 = z_s + b_r\theta - \frac{t_r}{2}\phi, z_4 = z_s + b_r\theta + \frac{t_r}{2}\phi, \end{aligned} \tag{2.6}$$

where a) z_s is the linear displacement of the CMC in the vertical direction. b) $\Delta\boldsymbol{l_t} = [\Delta l_{t1}, \Delta l_{t2}, \Delta l_{t3}, \Delta l_{t4}]^T$ are the tire deflections at each corner (for example, $\Delta l_{t1} = z_{r1} - z_{u1}$), and c) $\boldsymbol{z_{lin}} = [z_{lin1}, z_{lin2}, z_{lin3}, z_{lin4}]^T$ are the linear equivalent actuator displacements at each corner. The system input includes the disturbance signals and control input, which is defined as: $v = [\mathbf{w}^T, \mathbf{u}^T]^T$ where the exogenous



(b)

Figure 2.7: (a) Transformation between the linear equivalent and multi-body models of the PALS quarter-car; (b) Schematic of the SAVGS quarter car model.

disturbance signal is $\mathbf{w} = [\dot{\boldsymbol{z}}_{\boldsymbol{r}}^T, T_p, T_r]^T$ and the control input is $\mathbf{u} = \dot{\boldsymbol{z}}_{\boldsymbol{lin}}$, in which $\dot{\boldsymbol{z}}_{\boldsymbol{r}} = [\dot{z}_{r1}, \dot{z}_{r2}, \dot{z}_{r3}, \dot{z}_{r4}]^T$ are the derivatives of the road (displacement) profiles at the four wheels, T_p and T_r are respectively the exogenous pitch and roll torques applied on the chassis, and $\dot{\boldsymbol{z}}_{\boldsymbol{lin}} = [\dot{z}_{lin1}, \dot{z}_{lin2}, \dot{z}_{lin3}, \dot{z}_{lin4}]^T$ are the derivatives of the linear equivalent actuator displacements. The selection of the vector of output variables, y, is based on the the sensors availability as:

$$y = [\boldsymbol{z}_{\boldsymbol{lin}}^T, \Delta\boldsymbol{l}_{\boldsymbol{t}}^T, \Delta\boldsymbol{l}_{\boldsymbol{s}}^T, \ddot{z}_s, \ddot{\theta}, \ddot{\phi}]^T, \tag{2.7}$$

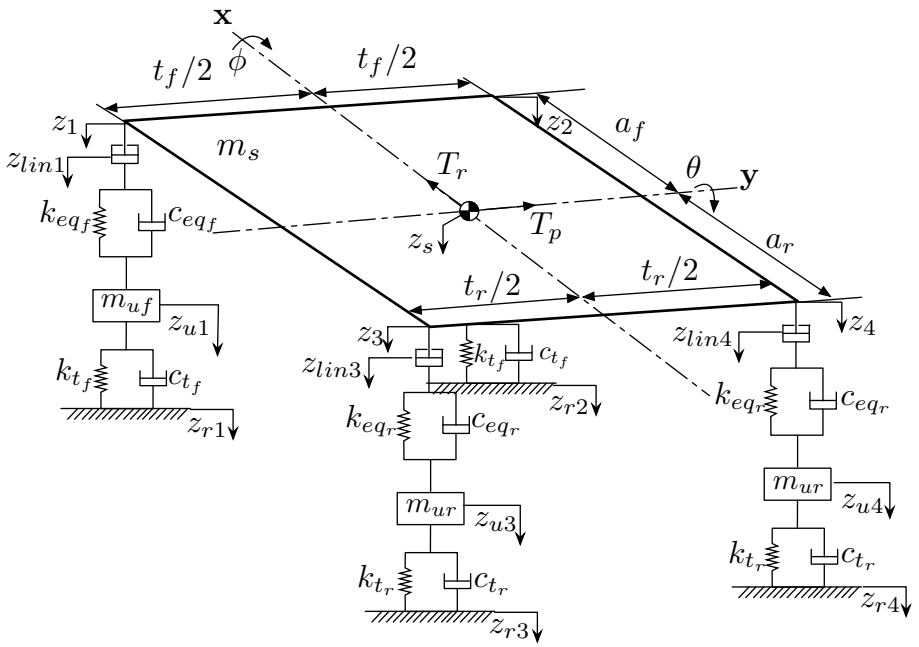


Figure 2.9: Linear equivalent model of SAVGS full car [24, 25].M_s is the sprung mass, T_p and T_r are the chassis pitch and roll disturbance moments respectively, z_{lini} are the linear equivalent actuator displacements at each corner, θ and ϕ are the pitch and roll angles respectively, and the z variables denote linear vertical displacements of the points/masses indicated, while the rest of the symbols are defined in Table 2.2.

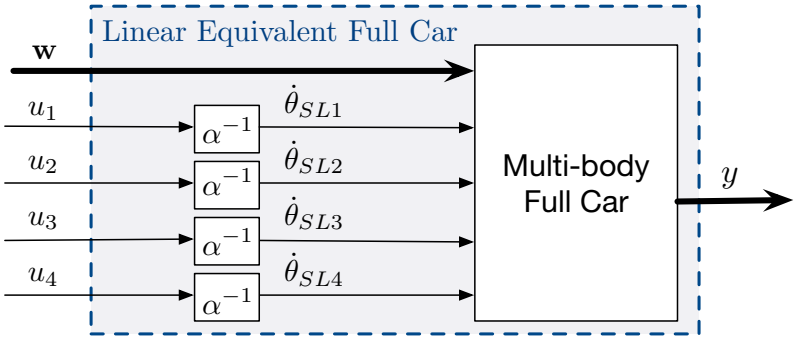


Figure 2.10: Conversion between linear equivalent and multi-body models of the SAVGS full car.

2.2.4.4 Linear Equivalent Model of the Full-car PALS

To enable linear robust control synthesis, a linear equivalent model of the PALS full car that extends the linear equivalent quarter car model [22] and extracts the suspension geometry nonlinearities, as also presented in [5] is employed and summarised here, as shown in Figure 2.11 and with its parameters value detailed in Table 2.3.

The state space representation of the model can be constructed as follows:

$$\begin{aligned} \dot{x} &= Ax + Bv, \\ y &= Cx + Dv. \end{aligned} \tag{2.8}$$

Table 2.2: Main Parameters of Original and SAVGS Retrofitted GT full car, and linear equivalent model (F: Front, R: Rear)

Parameters	Value
Original vehicle [7, 21, 24, 26]	
CMC Height	0.424 m
F/R Weight distribution	43/57 %
Total/Sprung mass	1525/1325 kg
F/R Suspension spring stiffness	92/158 $\frac{kN}{m}$
F/R Tire stiffness	275 $\frac{kN}{m}$
F/R Tire damping	300 $\frac{Ns}{m}$
F/R Installation ratio	0.60/0.56
Linear equivalent model SAVGS full car	
F/R Nominal Suspension damping ($\bar{c}_{eq_f}/\bar{c}_{eq_r}$)	1492.7 / 2028 $\frac{Ns}{m}$
F/R Equivalent Suspension stiffness (k_{eq_f}/k_{eq_r})	35.41 / 58.96 $\frac{kN}{m}$
F/R Tire stiffness (k_{tf}/k_{tr})	275 $\frac{kN}{m}$
F/R Tire damping (c_{tf}/c_{tr})	300 $\frac{Ns}{m}$
F/R Track width (t_f/t_r)	1.669 / 1.615 m
F/R Wheelbase (a_f/a_r)	2.6 / 2.6 m
Nominal sprung mass (M_{nom})	1375 kg
SAVGS retrofit (actuator per corner) [7, 21, 24, 26]	
F&R Actuator mass	6 kg
F&R Gear Ratio	40
F/R Low speed shaft (LSS) continuous torque	97/97 $N{\cdot}m$
F/R LSS peak torque	205/205 $N{\cdot}m$

The state vector is chosen as follows for the minimal realisation of the linear system:

$$x = [\dot{z}_s, \dot{\theta}, \dot{\phi}, \dot{\boldsymbol{z}}_{\boldsymbol{u}}^T, \Delta \boldsymbol{l}_{\boldsymbol{s}}^T, \Delta \boldsymbol{l}_{\boldsymbol{t}}^T]^T, \tag{2.9}$$

where the variables in the state vector are defined in the SAVGS full car subsection 2.2.4.3).

The system input vector v includes the disturbance signals and control input:

$$v = [\mathbf{w^T}, \mathbf{u^T}]^\mathbf{T}, \tag{2.10}$$

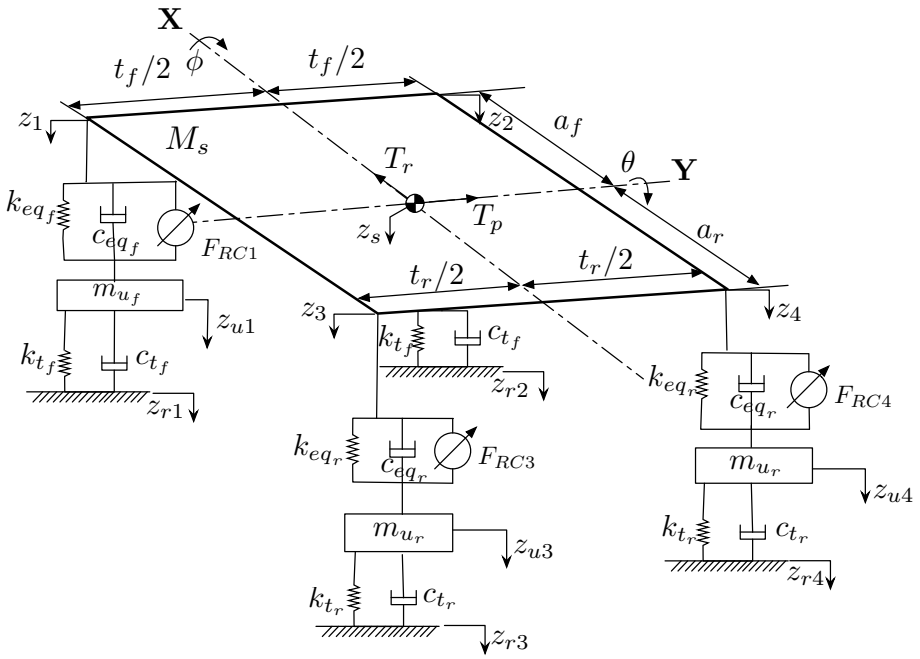


Figure 2.11: Linear equivalent model of PALS full car. F_{RCi} **are the linear equivalent actuation forces at each corner, while the rest of the symbols are defined in the subsection 2.2.4.3.**

where the exogenous disturbance signal $\mathbf{w} = [\dot{\mathbf{z}}_{\boldsymbol{r}}^{\mathbf{T}}, \mathbf{T_p}, \mathbf{T_r}]^{\mathbf{T}}$ consists of vertical road profiles at each wheel. The control input is $u = \boldsymbol{F_{RC}}$ where $\boldsymbol{F_{RC}} = [F_{RC1}, F_{RC2}, F_{RC3}, F_{RC4}]^T$ is the linear equivalent actuation force of the PALS at each corner. The selection of the vector of output variables, y, is based on the sensors availability to achieve the control objectives as:

$$y = [\ddot{z}_s, \ddot{\theta}, \ddot{\phi}, \Delta \boldsymbol{l}_{\boldsymbol{s}}^T, \Delta \boldsymbol{l}_{\boldsymbol{t}}^T]^T, \tag{2.11}$$

In addition, as shown in Figure 2.12, conversion functions β_i (from each linear equivalent actuation force F_{RCi} to the generated torque of the actual PALS rotary actuator) that are related to the suspension geometry variation against the suspension deflection increment, are further taken into account. That is to bridge the linear equivalent and nonlinear multi-body models of the PALS full car and compensate the varied geometry nonlinearity in terms of the suspension stroke.

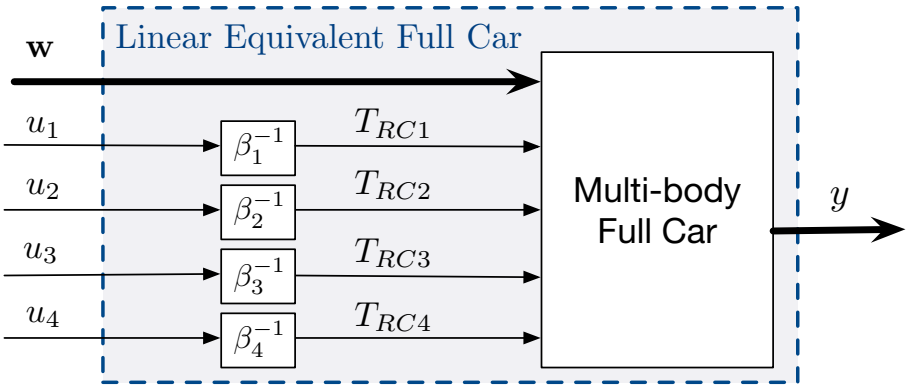


Figure 2.12: Conversion between linear equivalent and multi-body models of the PALS full car.

Table 2.3: Main Parameters of Original and PALS Retrofitted SUV full car, and linear equivalent model (F: Front, R: Rear)

Parameters	Value
Original vehicle [5, 7]	
CMC Height	0.71 m
F/R Weight distribution	50/50 %
Total/Sprung mass	2950/2700 kg
F/R Suspension spring stiffness	150/200 $\frac{kN}{m}$
F/R Tire stiffness	290 $\frac{kN}{m}$
F/R Tire damping	300 $\frac{Ns}{m}$
F/R Installation ratio	0.58/0.50
Linear equivalent model PALS full car	
F/R Nominal Suspension damping ($\bar{c}_{eq_f}/\bar{c}_{eq_r}$)	2355 / 2002 $\frac{Ns}{m}$
F/R Equivalent Suspension stiffness (k_{eq_f}/k_{eq_r})	53.5 / $\frac{kN}{m}$
F/R Tire stiffness (k_{tf}/k_{tr})	290 $\frac{kN}{m}$
F/R Tire damping (c_{tf}/c_{tr})	300 $\frac{Ns}{m}$
F/R Track width (t_f/t_r)	1.677 / 1.696 m
F/R Wheelbase (a_f/a_r)	1.538 / 1.538 m
Nominal sprung mass (M_{nom})	2700 kg
PALS retrofit (actuator per corner) [5, 7]	
F&R Actuator mass	12 kg
F&R Gear Ratio	66
F/R Low speed shaft (LSS) continuous torque	166/165 $N{\cdot}m$
F/R LSS peak torque	273/273 $N{\cdot}m$

2.2.5 PALS Full-car Steady-state Model and Analysis

A mathematical steady-state model of the full car, as shown in Figure 2.13, is developed to analyse the equilibrium forces and further evaluate the PALS capability in terms of chassis levelling. The vertical tire force F_{tz} at any given corner can be estimated as follows:

$$F_{tz} = F_{tz}^{(ne)} + \Delta F_{tz}^{(ax)} + \Delta F_{tz}^{(ay)} + \Delta F_{tz}^{(ae)}, \tag{2.12}$$

where $F_{tz}^{(ne)}$ is the vertical tire force in the nominal configuration, $\Delta F_{tz}^{(ax)}$ and $\Delta F_{tz}^{(ay)}$ represent the vertical tire force increments due to longitudinal and lateral accel-

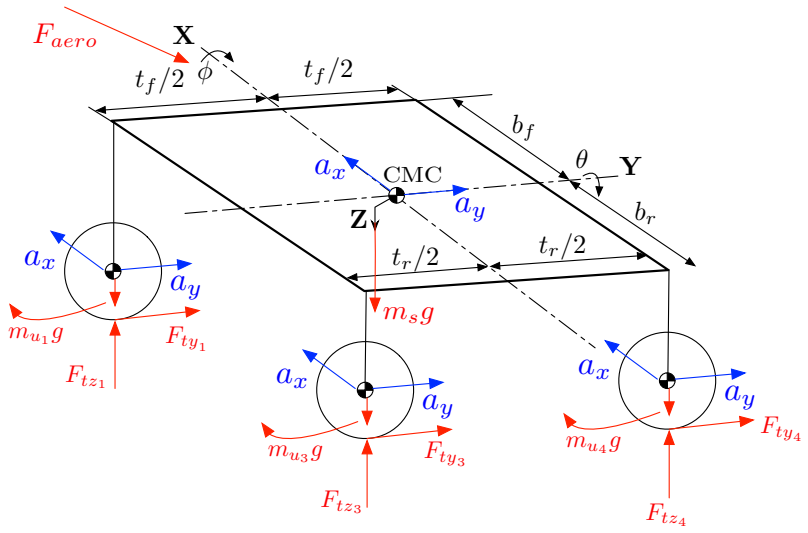


Figure 2.13: Schematic of the steady-state PALS-retrofitted full-car model.

For the equilibrium of vertical forces to hold for the whole vehicle and for each axle independently, the following relationships must be satisfied:

$$\begin{aligned} &\Delta F_{tz_1}^{(ax)} = \Delta F_{tz_2}^{(ax)} = -\Delta F_{tz_3}^{(ax)} = -\Delta F_{tz_4}^{(ax)}, \\ &\Delta F_{tz_1}^{(ay)} = -\Delta F_{tz_2}^{(ay)}, \quad \Delta F_{tz_3}^{(ay)} = -\Delta F_{tz_4}^{(ay)}, \end{aligned} \tag{2.13}$$

where the right subscript refers to the corner number 1 to 4 denoting the front left, front right, rear left and rear right corners, respectively. The vertical tire force increment due to vehicle longitudinal acceleration is obtained by the balance of pitching moments $\Sigma M_y = 0$:

$$\Delta F_{tz_1}^{(ax)} = [\frac{m_s h_{CMC} + 2(m_{u_f} R_{wh_f} + m_{u_r} R_{wh_r})}{2(b_f + b_r)}] a_x, \tag{2.14}$$

where m_{u_f} and m_{u_r} correspond to the front and rear unsprung mass, respectively, which are not supported by the springs, m_s to the sprung mass which is the rest of the mass of the car, h_{CMC} to the height above the ground of the center of the mass of the chassis, b_f and b_r to the front and rear wheelbase and R_{wh_f} and R_{wh_r} to the front and rear wheel radius, respectively.

Similarly, the vertical tire force increment influenced by lateral acceleration can be estimated through the balance of rolling moments:

$$\begin{aligned} M_x &= [(m_s h_{CMC} + 2(m_{u_f} R_{wh_f} + m_{u_r} R_{wh_r})] a_y, \\ \Delta F_{tz_1}^{(ay)} t_f &= (1 - \sigma) M_x, \\ \Delta F_{tz_3}^{(ay)} t_r &= \sigma M_x, \end{aligned} \tag{2.15}$$

where $\sigma \in [0\ 1]$ is defined as the ratio of overturning distribution (OCD) provided by the rear axle.

The vertical tire force increment on both front and rear axles caused by their aerodynamics force can be calculated through:

$$\begin{aligned} \Delta F_{tz_1}^{(ae)} = F_{tz_2}^{(ae)} &= \frac{1}{2} c_{ad_f} v_x^2, \\ \Delta F_{tz_3}^{(ae)} = F_{tz_4}^{(ae)} &= \frac{1}{2} c_{ad_r} v_x^2, \end{aligned} \tag{2.16}$$

where c_{ad_f} and c_{ad_r} are the aerodynamic downforce coefficients for the front and rear axles, respectively, and v_x is the longitudinal velocity of the vehicle.

Based on the steady state vertical tire forces of the full car provided in (2.12)-(2.16), the chassis leveling capability of PALS can be achieved as follows.

Applying the principle of virtual work to a corner of the car with rocker-pushrod and the double wishbone linkages with the road wheel taken into account and considering a static chassis yields

$$T_{RC_i} = \frac{\partial z_{H_i}}{\partial \theta_{RC_i}} \Delta F_{tz_i} = \frac{\partial l_{s_i}}{\partial \theta_{RC_i}} \Delta F_{RC_i}, \tag{2.17}$$

where z_{H_i} is the vertical coordinate of the road wheel center, θ_{RC_i} is the rocker angle with respect to the horizontal line, l_{s_i} is the suspension deflection, and F_{RC_i} is the linear equivalent actuation force.

Transformation functions between ΔF_{tz_i} and T_{RC_i} at each corner can be defined as follows:

$$\beta_i = \beta_i(z_{H_i}) = \frac{\Delta F_{tz_i}}{T_{RC_i}} = \frac{\partial \theta_{RC_i}}{\partial z_{H_i}}. \tag{2.18}$$

The uncertainties have been considered in the μ-synthesis control applied in many active suspension systems [27, 28]. However, for the SAVGS and PALS suspension system studied in this thesis, the previous work did not take into account practical structured uncertainties, which may lead to substantial deterioration of the suspension performance under certain circumstances. Therefore, the μ-synthesis-based control is first developed in thesis for SAVGS and PALS with uncertainties taken into account to solve the robustness. Moreover, the feedforward control has been utilised in semi-active suspension to improve the stability in [29]. Nevertheless, the previous work has only synthesized PID control in the SAVGS and PALS suspension system for chassis leveling which has slow response time and leads to reduced performance and reduced stability in some circumstances. Therefore, a feedforward-PID control strategy based on nonlinear simulation fit derived compensation model is proposed in this thesis to address the problem of feedback delay in chassis stabilisation and

slow response time of PID control in chassis leveling.

2.2.6 Road-profile Models

The modelling of the road profile is of great importance to simulations of vehicle models, being the main excitation source. The vehicle dynamics' responses to the road input determine the vehicle-body acceleration, suspension travel, tire deflection, and vehicle displacements. In this thesis, road disturbances can normally be classified into two groups: i) deterministic roads, such as bumps and sinusoidal profiles; and ii) random roads.

2.2.6.1 Sinusoidal Roads

Sinusoidal inputs are often utilised to study vehicle motions. A 2 Hz frequency is used to investigate the superior improvement of the synthesised controller at a frequency near the vehicle's natural frequencies.

2.2.6.2 Smoothed Speed Bumps

Speed bumps (or humps) are common on some roadways and are normally approximated as a raised cosine shape. The rear axle experiences a bump after a travel distance delay due to the wheel base (l_w) with respect to the front wheel. The mathematical representations of the front and rear wheels' road heights, h_f and h_r, when running over a standard laterally uniform bump (0.05 m height and 20.55 m length) are presented below:

$$\begin{aligned} h_f &= 0.025(1 - cos(2\pi x/2)), \\ h_r &= 0.025(1 - cos((2\pi x - l_w)/2)), \end{aligned} \tag{2.19}$$

where h_f and h_r are functions of the travel distance x. In the numerical simulation environment, the PALS-retrofitted full car is driven over such a bump at a constant forward speed.

2.2.6.3 Random-road Porfiles

The ISO random roads are used to simulate road unevenness. The measured vertical surface data of different road profiles, such as streets, highways and off-road terrain, are usually described in terms of their power spectral density (PSD), which is defined in the frequency domain as follows [30]:

$$G_d(n) = 10^{-6} \cdot 2^{2k}(\frac{n}{n_0})^{-\omega}, \tag{2.20}$$

where n is the spatial frequency and $k = 2$ to 9 corresponds to the road roughness classes A to H respectively. Here, $n_0 = 0.1\,\text{cycles/m}$ is the reference spatial frequency and $\omega = 2$ is typically a constant. In the numerical simulation environment, the PALS-retrofitted full car is driven at a forward speed of 100 km/h, different road profiles (of same unevenness) against traveled distance are generated for the left and right side wheels respectively, and the traveled distance delay due to the wheelbase (α_f+α_r) occurs in the road profile seen by the rear axle as compared to the road profile seen by the front one. The PSD plots of the random-road profiles used in this thesis for nonlinear simulations are depicted in Figure 2.14.

2.3 Vehicle Suspension Control

Over the years, many active suspension control approaches have been proposed in the academic and industrial fields. Academic publications written about suspension systems show that the control methodologies can be classified into three categories: i) chassis attitude control; ii) vibration attenuation control; and iii) hybrid control.

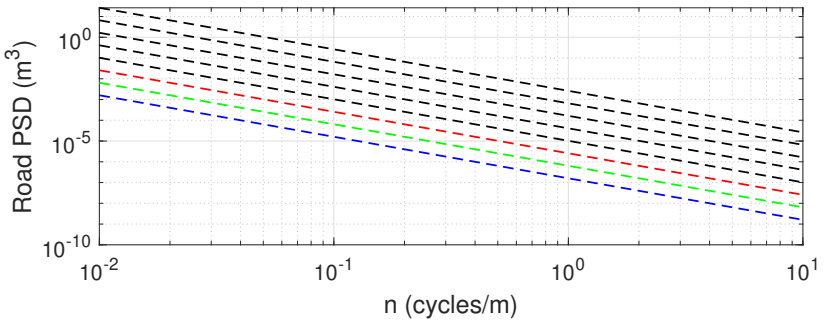


Figure 2.14: PSD estimate of the random-road profiles, with roughness A to C considered in this thesis shown in blue, green and red lines, corresponding to good, above average and average quality road.

2.3.1 Chassis Attitude Control

The most widely used control theories employed to cope with attitude motion mitigation are grouped into these families: i) PID control, ii) PID-based hybrid control, and iii) backstepping control. The following paragraphs will give some qualitative insights into each of these control techniques.

2.3.1.1 PID control

The multi-objective PID control methodology is used for the active suspension of SAVGS [2] and PALS [5] , with the aim being to control chassis attitude over a low-frequency range. The overall configuration is shown in Figure 2.15. As an example, at the front-left corner (i = 1), $C_{11}, C_{21} \ldots C_{N1}$ are given as a set of PID controllers that tackles the following problems: i) the heave motion; ii) the roll and pitch angle; iii) the overturning couple distribution (OCD) (and so on). The proportional, integral and derivative gains in $C_{11} \sim C_{N1}$ are tuned and updated by a higher logic controller, the purpose of which is to objectively improve the vehicle dynamics in various driving circumstances. Here, $s_{11}, s_{12} \ldots s_{N1}$ are the measurement feedback for the PID controllers. The single-link control outputs $\Delta\theta_{SL1}^{(1)*} \sim \Delta\theta_{SL1}^{(N)*}$

are constrained in angular limits and coordinated to adjust the chassis attitude.

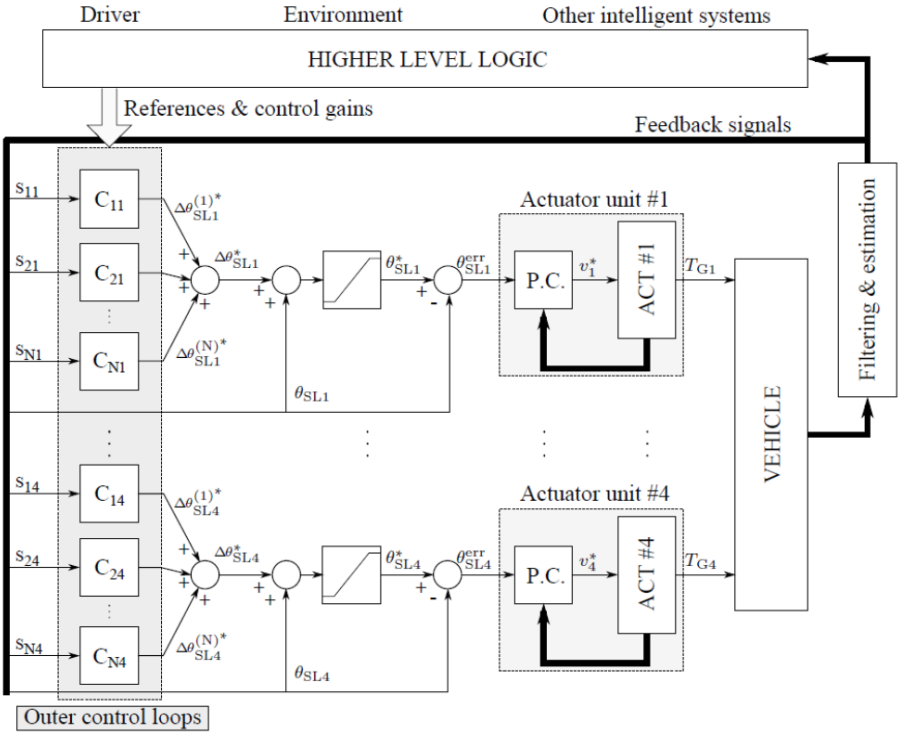


Figure 2.15: Multi-objective PID chassis attitude control scheme for the SAVGS full car [2].

2.3.1.2 PID-based Hybrid Control

Many control methodologies have been combined with PID control to synthesise an adaptive PID control that adjusts the PID gains using an adaptive tuning algorithm. In [31], the fuzzy PID algorithm is proposed to adjust the vehicle driving attitude; it does so by changing the speed of each wheel in real time for the purpose of optimising the driving stability of the vehicle and offering better adaptive ability. In [32], an adaptive PID control scheme is proposed with the aim of achieving ride comfort and vehicle's stability enhancement for a vehicle suspension system subjected to road disturbance. Here, the update parameters of adaptive PID are tuned online using the gradient descent method.

However, a conventional feedback control system such as PID, due to delays, finds it very difficult to regulate the roll and pitch behaviour and to stabilise the chassis attitude; this may result in roll over when the vehicle steers at a large longitudinal velocity.

2.3.1.3 Backstepping control

Backstepping control is preferred in active suspension, since it provides a systematic procedure for the construction of the Lyapunov functions and related feedback control laws, guaranteeing system stability in the chassis levelling. The adaptive backstepping control method is a modified form of this type of method that uses estimates for unknown system parameters. Despite these achievements, the backstepping control needs information about all system states and exists the steady state error. Moreover, it has calculation explosion when operating with several levels of recursion. In [33], an adaptive backstepping control method is proposed with the aim of stabilising the attitude of a vehicle in the presence of parameter uncertainties and hard constraints (including dynamic tire loads, actuator saturations and suspension spaces). In [34], a model-based adaptive backstepping control for semi-active suspension is proposed with the aim of managing the trade-off between the conflicting requirements of ride comfort and chassis attitude stabilisation in the presence of parameter uncertainties.

2.3.2 Vibration Attenuation Control

The ride comfort and road holding are the two main objectives in the vibration attenuation control. It is well known that these two aspects of suspension performance are commonly quantified through the vertical body acceleration of the sprung mass, and vertical tire deflections at each corner [21]. the vertical body acceleration

$\ddot{z}_s$ should be minimised to isolate passengers from vibrations and improve ride comfort. To achieve the desired road holding property, it is recommended to guarantee firm uninterrupted contact of the wheels with the road and keep the tire deflection Δl_t as small as possible. The control strategies for ride comfort and road-holding improvement are as follows: i) sky-hook control; ii) H_∞ control; iii) μ-synthesis control; iv) sliding mode control (SM); v) optimal control; vi) model predictive control; and vii) intelligent control.

The following paragraphs will offer insights into each of these control techniques.

2.3.2.1 Skyhook Control

Skyhook control is generally applied in semi-active suspension; it is easy to implement even with little information about the vehicle state [35]. As shown in Figure 2.16, skyhook control sets a virtual damper between the sprung mass and the inertial reference (or imaginary sky). The damper, emulated by the controlled force-producing elements, restricts the motion of the sprung mass and therefore enhances the ride comfort, as well as also achieving improved resonance damping compared to that of the SD system.

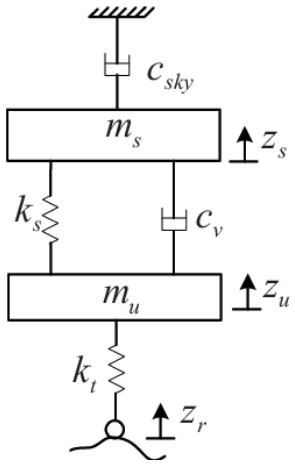


Figure 2.16: Skyhook control in a linear equivalent quarter-car model [36].

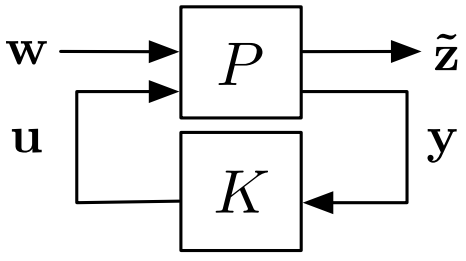


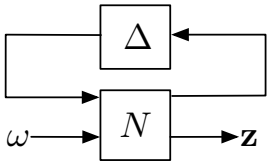
Figure 2.17: A generalised regulator. P corresponds to a time-invariant state-space representation of a linear plant, K to the related synthesised controller, w to exogenous disturbance signals, $\tilde{\mathbf{z}}$ to the error signals to be minimised, u to the control input, and y to the system measurements for feedback.

In recent years, H_∞ synthesis has been applied also more widely to active suspension controls. In [38], a non-fragile H_∞ static output feedback control is introduced to improve ride quality, at the same time satisfying control saturation constraint while being limited by the actuator power. The researchers proved that output feedback control is a robust methodology that can be used to deal with the disturbance attenuation problems presented by active suspensions. The H_∞ control scheme is designed for quarter- [1, 4, 39] and full-car [5, 26] models and affects ride comfort and road-holding improvement.

However, the vehicle parameter uncertainties are mainly ignored in the H_∞ control synthesised in SAVGS and PALS application, which may result in the deterioration of the their performance in the cases of increased payload, long stroke operation of the suspension dampers and so on.

2.3.2.3 μ-synthesis Control

μ-synthesis control allows the design of a multi-variable optimal robust controller for complex linear systems with any type of uncertainty in their structure. As shown in Figure 2.18, the objective of the μ-synthesis controller is to calculate a stabilising robust controller for the uncertain open-loop plant model via the $D-K$ algorithm for μ-synthesis [40]. Full-car models with active suspensions are employed and tested using μ-synthesis control and it is worth noting that the ride comfort and road-holding performance can be further improved while still satisfying the design specifications that the induced disturbances from uncertainties must remain below a certain level.



(b)

Figure 2.18: (*a*) An extended generalised regulator for μ-synthesis, and (*b*) the analysis framework [40]. Δ is a structured uncertainty block diagonal matrix.

2.3.2.4 Sliding-mode control

SM control is known as a powerful control tool that can enhance the robustness of a control system regardless of the external disturbances and/or parameter variations. A chattering-free terminal SM (TSM) control scheme for suspension systems has been proposed in [41]; this scheme is intended to tackle the issues of chattering and singularity. A proportional integral SM control scheme has been proposed in [42]; this will allow the active suspension system to assess the strong robustness of the control strategy. To improve performance issues other than robustness, the optimal control has been incorporated into the SM control in an effort to design a controllable suspension for vehicles that offers a nominal optimal performance. A feedforward optimal SM controller and a feedback optimal SM controller for active suspensions has been proposed in [43]. An improved optimal SM control method for non-linear active suspension systems has been proposed in [44] that hopes to obtain both the true nominal optimal suspension performance and better robustness.

2.3.2.5 Optimal Control

Optimal control laws for unconstrained active suspensions, including linear quadratic regulator (LQR) and linear quadratic Gaussian (LQG), have been studied with the objective of finding a controller that minimises the quadratic cost function

for a system's white noise inputs, subject to the linear system dynamics. When the LQR is applied to an active suspension, the objective (suspension performance) is expressed using quadratic indexes and is weighted through a cost function. In addition, since additional measurement noise and process noise within a suspension system cannot be neglected, a Kalman filter is introduced to estimate the true state when noise (as additive white Gaussian noise) is added to an uncertain linear system. This combination of an LQR control and a Kalman filter is known as a LQG regulator, which can design a linear feedback controller based on a non-linear uncertain system.

The authors in [45] make use of the analytic hierarchy process to optimise the weights of performance indices in the design of an active suspension LQG controller, based on a full-vehicle model with seven DOFs. In [46], an optimal design method for an active suspension based on LQG control without road input signal is proposed with the intention of comprehensively optimising ride comfort and road holding. The authors in [47] propose the LQR for a half-car active suspension, thereby providing the best possible performance while minimising the required actuator force.

2.3.2.6 Model Predictive Control

Model Predictive Control (MPC) is one of the most widely applied control methods in the manufacturing and industrial control fields and is one of the few approaches which can handle hard constraints and system changes in real-time. Briefly, the MPC method is also referred to as receding horizon control (RHC); it measures and applies the current state of the system as the initial state used to solve the online optimisation problem at each sampling instant before generating corresponding optimal control input sequences. To satisfy the relevant accuracy requirement for the optimal control input sequences thereby obtained, the method only utilises the first item in the generated optimal control sequence input into the system. Fol-

lowing this process, the above mentioned procedures are all operated repeatedly at the next sampling instant. The MPC method has a powerful ability to control a multivariable system in complex situations [48].

In a practical situation, the perturbation will appear in the system; this must be considered to guarantee robustness. Generally speaking, the perturbation can be separated into internal perturbation (such as structured uncertainties) and external perturbation (such as bounded disturbances). The corresponding MPC algorithm is then referred to as an RMPC and takes into account both disturbances and system uncertainties. The offline LMI-based RMPC proposed in [49, 50] overcomes the vehicle suspension problem through the use of offline optimisations prior to implementation, subject to the presence of uncertainties and disturbances.

2.3.2.7 Intelligent Control

An adaptive vibration control combines the intelligent control algorithms (fuzzy logic, neural networks and genetic algorithms) with the aforementioned robust control methods (H2/H_∞ and SM) as shown in Figure 2.19. A reliable fuzzy H_∞ control is proposed in [51, 52] for uncertain active suspension systems, thereby guaranteeing a better suspension performance under both sprung and unsprung mass variations, actuator delay and faults arising from the Takagi-Sugeno (T-S) fuzzy model approach. An adaptive neural network SM control is proposed in [53]; this provides the optimal control force and achieves a trade-off between the riding and handling performance offered by the active suspension system. In [54, 55], an adaptive SM control is proposed for the nonlinear uncertain vehicle active suspension systems via the T-S fuzzy approach improving the suspension performance and satisfying the suspension constraint.

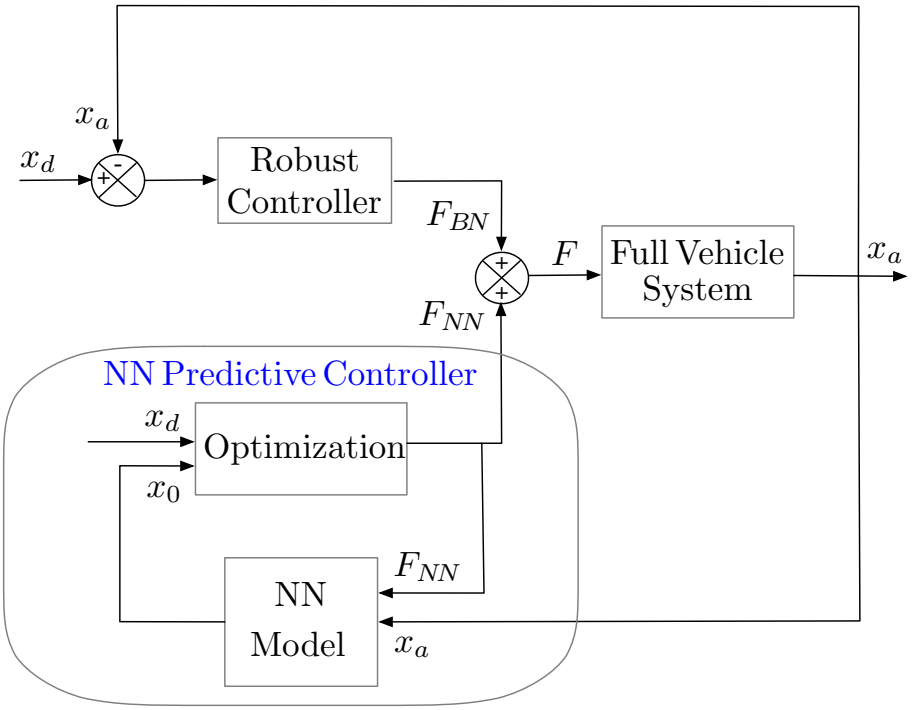


Figure 2.19: Configuration of the adaptive neural network-based robust control for active suspension.[53]

2.3.2.8 Preview Control

The idea of a preview was first proposed for vehicle suspension by Bender [56]; it provides the oncoming road height profile that enables the vehicle to prepare for future road inputs and to pass through abrupt road obstacles without suffering any severe impact. The most frequently used method used to collect information about the road ahead is equipping with the advanced camera or look-ahead sensor, as shown in Figure 2.20.

Most preview control methods are based on linear quadratic control theory [56, 58]. The unknown disturbances that commonly act on a car, however, are ignored in the design and implementation of the controller design. Nevertheless, a great many preview control strategies (based on H_∞ and MPC) have been reported; these do take disturbances into account in the control design to obtain a better performance.

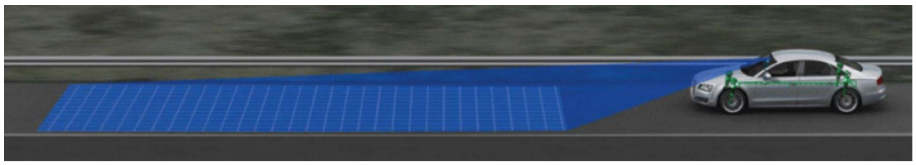


Figure 2.20: Preview control in active suspension, equipped with advanced camera [57].

An H_∞ preview controller for an active suspension has been proposed in [59]. In [60], a robust H_∞ preview control that assumes exact road inputs is proposed; this is intended to improve the road holding and stabilise the system, irrespective of the uncertainties. An MPC for a nonlinear full-car active suspension, equipped with an advanced camera that offers preview information about the upcoming road, is proposed in [61, 62, 63]; this is intended to improve the ride comfort and handling characteristics by utilising lookahead information.

2.3.3 Multi-objective Hybrid Control

To address the multiple objectives inherent in the vehicle suspension control problem, many publications contain studies that propose the use of blended control methodologies. These hybrid control methods can be categorised as follows: i) the combined H_∞-synthesis PID control scheme, which tackles the ride comfort, road holding and attitude control objectives; and ii) the multi-objective control, which improves the ride comfort, road holding and energy-harvesting performance.

2.3.3.1 Frequency-dependent Multi-objective Control Strategies

To enable the implementable synchronous control of both low-frequency signal tracking and high-frequency vibration attenuation, a frequency-dependent multi-objective control scheme is proposed for the PALS in [5]. As showin in Figure 2.21, the H_∞ control takes effect at high-frequency road events to enhance the ride comfort

and the road holding, while the multi-objective PID control stabilises the rocker torque at each corner in low-frequency road events to achieve the desirable chassis attitude.

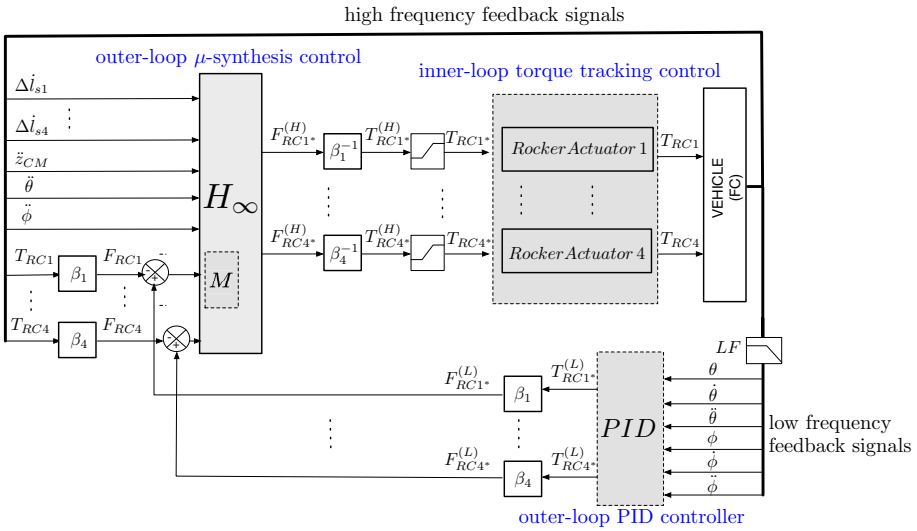


Figure 2.21: Configuration of the frequency-biased multi-objective control scheme in the PALS-retrofitted full car [5].

2.3.3.2 Multi-objective Control for comfort and Energy Harvesting

In the 1990s, researchers found that the electromagnetic damper that had replaced the traditional hydraulic damper added energy regeneration and adaptability to the suspension (as shown in Figure 2.22). Since then, many advanced control methodologies have been designed for suspension systems equipped with an electromagnetic damper to maximise the harvested energy. In [64], a multi-objective H_∞ controller has been designed and implemented on a quarter-car test rig to minimise sprung-mass acceleration and power requirements and to maximise energy harvesting. In [65], flexible multi-objective control design strategies have been proposed that are based on LMI formulations; these offer a suitable trade-off between the usual road handling and ride comfort performance and the amount of energy that

can be harvested. Multi-objective optimisation methodologies have been developed, using a genetic algorithm to improve the performance of the vehicle with respect to the ride comfort, road holding and energy harvesting in [66].

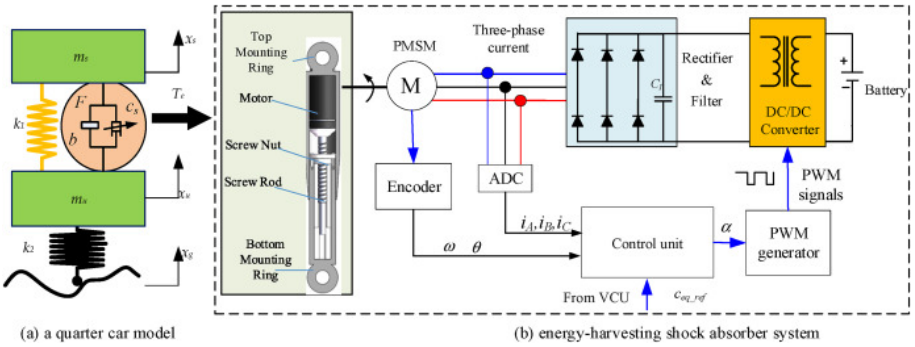


Figure 2.22: The structure of an energy-harvesting suspension system [65].

Overall, each of these control approaches can bring some useful perspective and insight. However, the performance of the PID and H_∞ control in the previous work is likely poor when dealing with uncertainties existing in the suspension system. Therefore, the present work will focus on the design of robust control schemes (i.e. μ-synthesis control and robust model predictive control) which takes the uncertainties of nonlinear suspension damping and variable payload into account.

2.4 Conclusion

This chapter has reviewed state-of-the-art of suspension structures and the control algorithms which is more concentrated on automotive suspension systems and state of the art closer to my work topic. As the basis of this thesis, the chapter contains descriptions of previous studies of the basic quarter-, half-, and full-vehicle SAVGS and PALS models. In the next chapter, the vehicle parameter uncertainties that have been ignored in previous control designs are investigated, and a μ-synthesis control is designed for a full car with SAVGS.

Chapter 3

Uncertainties Investigation and Mu-Synthesis Control Design for a Full Car

3.1 Introduction

In this chapter, a μ-synthesis-based control scheme [40] is proposed with the linear equivalent model of the SAVGS and the PALS full car, with the significant uncertainties of the sprung mass and the suspension damping considered. Numerical simulations with the high-fidelity GT and the SUV full car nonlinear models are further performed to evaluate their control robustness. More precisely, the objectives are: i) the identification and characterisation of structured uncertainties that are ignored during the linearisation of the SAVGS/PALS full car, ii) the design of a μ-synthesis-based robust controller for the SAVGS/PALS, and iii) numerical simulations as well as comprehensive comparisons (of the SAVGS/PALS μ-synthesis control results with results of the H_∞-controlled SAVGS and the passive suspension cases) for the evaluation of the control robustness, with the uncertainties effect

thoroughly investigated.

This chapter is organised as follows: Section 3.2 extracts significant uncertainties in the SAVGS and the PALS operation. Section 3.3 designs a μ-synthesis control scheme with the identified uncertainties accommodated in the control framework for the SAVGS and PALS, respectively. Section 3.4 performs numerical simulations to compare the μ-synthesis to the H_∞ control and the passive suspension case with the SAVGS and the PALS multi-body full-car model respectively, given selected uncertainties, with the ride comfort and road holding being the primary indexes. Finally, conclusions are drawn in Section 3.5.

3.2 Uncertainties Investigation

In this section, the identification and characterisation of the sprung mass and suspension damping uncertainties, resulting from actual system variance or approximations of nonlinear characteristics by linear counterparts, is provided for the SAVGS and the PALS respectively.

3.2.1 Uncertainties in linearisation of full car SAVGS

Uncertainties represent the discrepancy between the model used to design the controller and the actual system. With respect to the GT with SAVGS, the most significant and typical structured uncertainties include the sprung mass (M_s), and the suspension damping (c_{eqf}, c_{eqr}) for the front and rear axle spring-damper units, respectively. The M_s parameter variation is due to weight change in passenger load and/or cargo. In the present work $M_{\text{nom}} = 1375\,\text{kg}$ is the nominal sprung mass (one male passenger) and $M_{max} = 1525\,\text{kg}$ is the maximum sprung mass (two overweight male passengers). The variation of c_{eqf} and c_{eqr} is mainly caused by the considerable operational speed range of the dampers, which have nonlinear speed-

dependent characteristics.

The nonlinear characteristics of the actual dampers employed in this thesis are shown in Figure 3.1. The aim of the linearised characteristics utilised in the linear equivalent model, and also shown in Figure 3.1, are to provide the optimal compromise between the maximum and minimum slopes of the respective nonlinear characteristics [4, 21, 24].The present work represents the nonlinear damper as a nominal linear counterpart plus uncertainty. The possible ranges of values for the uncertain parameters are thus given as:

$$\begin{aligned} M_s &= (M_{\text{nom}} + \delta M_s)\,\text{kg}, \\ c_{eqf} &= (\bar{c}_{eqf} + \delta c_{eqf})\,\text{Ns/m}, \\ c_{eqr} &= (\bar{c}_{eqr} + \delta c_{eqr})\,\text{Ns/m}, \end{aligned} \tag{3.1}$$

where $M_{\text{nom}} = 1375\,\text{kg}$, $\bar{c}_{eqf} = 1492.7\,\text{Ns/m}$ and $\bar{c}_{eqr} = 2028\,\text{Ns/m}$. The perturbation parameters δM_s, δc_{eqf} and δc_{eqr} are defined as follows:

$$\begin{aligned} \delta M_s &\in [0, 0.11\,M_{\text{nom}}], \\ \delta c_{eqf} &\in [-0.3\,\bar{c}_{eqf}, 0.3\,\bar{c}_{eqf}], \\ \delta c_{eqr} &\in [-0.3\,\bar{c}_{eqr}, 0.3\,\bar{c}_{eqr}]. \end{aligned} \tag{3.2}$$

3.2.2 Uncertainties in linearisation of full car PALS

For the purposes of control design of the PALS-retrofitted SUV full car, in this thesis, the most typical and significant uncertainties considered are as in the SAVGS case the structured uncertainties of i) sprung mass (M_s), and ii) the suspension damping coefficients (c_{eq_f}, c_{eq_r}) for the front and rear axle spring-damper units respectively.

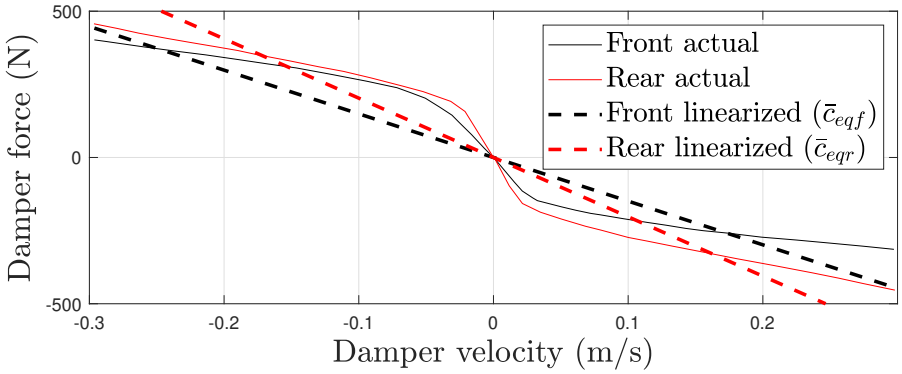


Figure 3.1: Nonlinear (solid) and linearised (dashed) characteristics of damper force versus damper velocity for the damper units installed at the front (black) and rear (red) axles for the GT with SAVGS full car[24].

The variation of parameter M_s arises from weight change in passengers and/or cargo, from the minimum (only driver), M_{min}, to the nominal (four male passengers), M_{nom}, to the maximum (seven male passengers), M_{max}, sprung mass. Furthermore, the operational speed range of the suspension dampers, which have nonlinear speed-dependent characteristics, leads to the variation of c_{eq_f} and c_{eq_r}.

The nonlinear damping characteristics in the real environment applied in this thesis for the SUV with PALS are shown in Figure 3.2 (from damper manufacturer datasheets). The purpose of the linearised characteristics utilised in the linear equivalent model, as shown in Figure 3.2, is to provide a suitable compromise between the maximum and minimum slopes of the respective nonlinear characteristics [21, 23]. The sprung mass and nonlinear dampers in the present work are therefore expressed as in the SAVGS case as a nominal linear counterpart plus uncertainty. The possible ranges of values for the uncertain parameters are thus given as:

$$\begin{aligned} M_s &= (M_{\text{nom}} + \delta M_s)\,\text{kg}, \\ c_{eq_f} &= (\bar{c}_{eq_f} + \delta c_{eq_f})\,\text{Ns/m}, \\ c_{eq_r} &= (\bar{c}_{eq_r} + \delta c_{eq_r})\,\text{Ns/m}, \end{aligned} \tag{3.3}$$

where $M_{\text{nom}} = 2700\,\text{kg}$, $\bar{c}_{eqf} = 1492.7\,\text{Ns/m}$ and $\bar{c}_{eqr} = 2028\,\text{Ns/m}$. The perturbation parameters δM_s, δc_{eqf} and δc_{eqr} are defined as follows:

$$\begin{aligned} \delta M_s &\in [-0.11 M_{\text{nom}}, 0.11 M_{\text{nom}}], \\ \delta c_{eq_f} &\in [-0.3\,\bar{c}_{eq_f}, 0.3\,\bar{c}_{eq_f}], \\ \delta c_{eq_r} &\in [-0.3\,\bar{c}_{eq_r}, 0.3\,\bar{c}_{eq_r}]. \end{aligned} \tag{3.4}$$

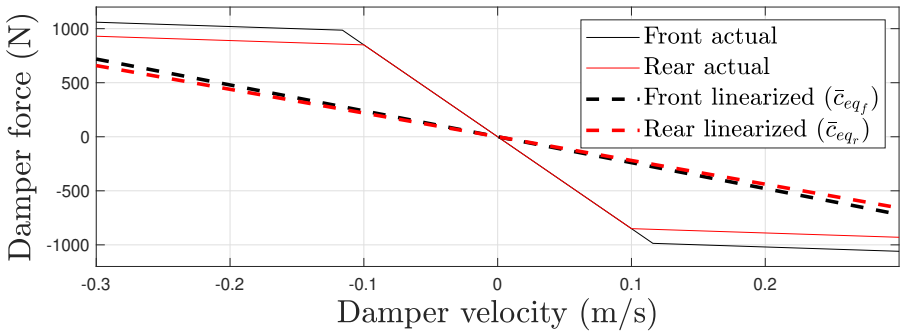


Figure 3.2: Nonlinear (solid) and linearised (dashed) characteristics of damper force versus damper velocity for the damper units installed at the front (black) and rear (red) axles for the SUV with PALS full car.

3.3 Robust Control Design

In this section, control strategies are designed and synthesised for the SAVGS and the PALS linear equivalent full-car models to improve the suspension performance in terms of the ride comfort and road holding, which are standard metrics for evaluating suspension vibration attenuation [67, 68, 69].

3.3.1 SAVGS Control Scheme

In this subsection, with the derived linear equivalent model of the SAVGS full car (Subsection2.2.2.2), a μ-synthesis control is developed with the ride comfort and road holding enhancement being the main objectives. It is also desired to stabilise

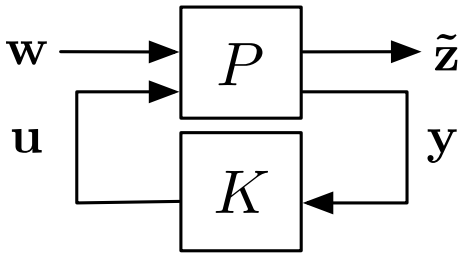


Figure 3.3: Generalised regulator. P **corresponds to a time-invariant state-space representation of a linear plant,** K **to the synthesised controller, w to exogenous disturbance signals,** $\tilde{\mathbf{z}}$ **to the cost signals to be minimised, u to manipulated variables, and y to the measurements feedback.**

The H_∞/H-2 control has been widely used in dealing with deterministic/stochastic excitation inputs to suspension systems [70, 71]. Though such mixed control studies exist, it is sufficient to design a H_∞ controller of the present work as the emphasis is towards the uncertainties in the system. The framework of the H_∞ control is used to synthesise controllers that achieve stabilisation with guaranteed performance. As shown in Figure 3.3, it intends to find a controller K such that the influence of exogenous disturbance ($\mathbf{w}$) to system performance objectives ($\tilde{\mathbf{z}}$) is minimised according to the H_∞ norm. The closed-loop transfer function matrix

$F_l(P,K)$ infinity norm is defined as:

$$\left\|F_l(P,K)\right\|_\infty = \sup_\omega \bar{\sigma}\left(F_l(P,K)(j\omega)\right), \tag{3.5}$$

where $\bar{\sigma}$ is the maximum singular value in the frequency domain. The H_∞ control design process involves the use of frequency-dependent weighting functions to tune the performance according to the ride comfort and road holding requirements. Figure 3.4 shows the closed-loop structure augmented with frequency weights for the H_∞ control synthesis ($P_{\mathbf{w}}$ is the augmented linear equivalent full car model, P), with disturbance signals, cost signals, manipulated variables, and measurements defined subsequently in (3.6)-(3.11).

The unweighted exogenous disturbance signals are defined as follows:

$$\tilde{\mathbf{w}} = [\tilde{\mathbf{w}}_\mathbf{a}, \tilde{\mathbf{w}}_\mathbf{b}] = [\tilde{\mathbf{w}}_\mathbf{I}, \tilde{\mathbf{w}}_\mathbf{II}, \tilde{w}_9, \tilde{w}_{10}, \tilde{\mathbf{w}}_\mathbf{III}, \tilde{w}_{15}, \tilde{w}_{16}, \tilde{w}_{17}]^T, \tag{3.6}$$

in which,

$$\tilde{\mathbf{w}}_\mathbf{a}^T = [\tilde{\mathbf{w}}_\mathbf{I}, \tilde{\mathbf{w}}_\mathbf{II}, \tilde{w}_9, \tilde{w}_{10}] = [(\mathbf{z}_\mathbf{lin}^\mathbf{(e)})^T, \dot{\boldsymbol{z}}_\boldsymbol{r}^T, T_p, T_r], \tag{3.7}$$

where $\mathbf{z}_\mathbf{lin}^\mathbf{(e)} = [z_{lin1}^{(e)}, z_{lin2}^{(e)}, z_{lin3}^{(e)}, z_{lin4}^{(e)}]^T$ are the exogenous commands of the linear equivalent actuator displacements, and

$$\tilde{\mathbf{w}}_\mathbf{b}^T = [\tilde{\mathbf{w}}_\mathbf{III}, \tilde{w}_{15}, \tilde{w}_{16}, \tilde{w}_{17}], \tag{3.8}$$

with $\tilde{\mathbf{w}}_\mathbf{III}$ corresponding to the suspension deflection sensor noise signals, and $\tilde{w}_{15}$, $\tilde{w}_{16}$ and $\tilde{w}_{17}$ to the CMC vertical, chassis pitch and chassis roll acceleration sensor noise signals.

The unweighted cost signal $\tilde{\mathbf{z}}$ is defined as follows:

$$\tilde{\mathbf{z}}^T = [(\dot{\boldsymbol{z}}_{\boldsymbol{lin}}^*)^T, \boldsymbol{e}_{\boldsymbol{z_{lin}}}^T, \boldsymbol{\Delta l}_{\boldsymbol{t}}^T, \ddot{z}_s, \ddot{\theta}, \ddot{\phi}], \tag{3.9}$$

where $\dot{\boldsymbol{z}}^*_{\boldsymbol{lin}}$ are the equivalent actuator reference speeds and $\boldsymbol{e}_{\boldsymbol{z}_{lin}} = \mathbf{z}^{(\mathbf{e})}_{\mathbf{lin}} - \boldsymbol{z}_{\boldsymbol{lin}}$ are the tracking errors of the linear equivalent actuator displacement.

The measurement signal $\mathbf{y}$ is defined as:

$$\mathbf{y}^T = [\mathbf{y_I}, \mathbf{y_{II}}, y_9, y_{10}, y_{11}] = [\boldsymbol{e}^T_{\boldsymbol{z}_{lin}}, \boldsymbol{\Delta l}^T_{\boldsymbol{s}}, \ddot{z}_s, \ddot{\theta}, \ddot{\phi}], \tag{3.10}$$

and the unweighted control signal $\tilde{\mathbf{u}}$ fed to the plant is defined as:

$$\tilde{\mathbf{u}} = \dot{\boldsymbol{z}}^*_{\boldsymbol{lin}}. \tag{3.11}$$

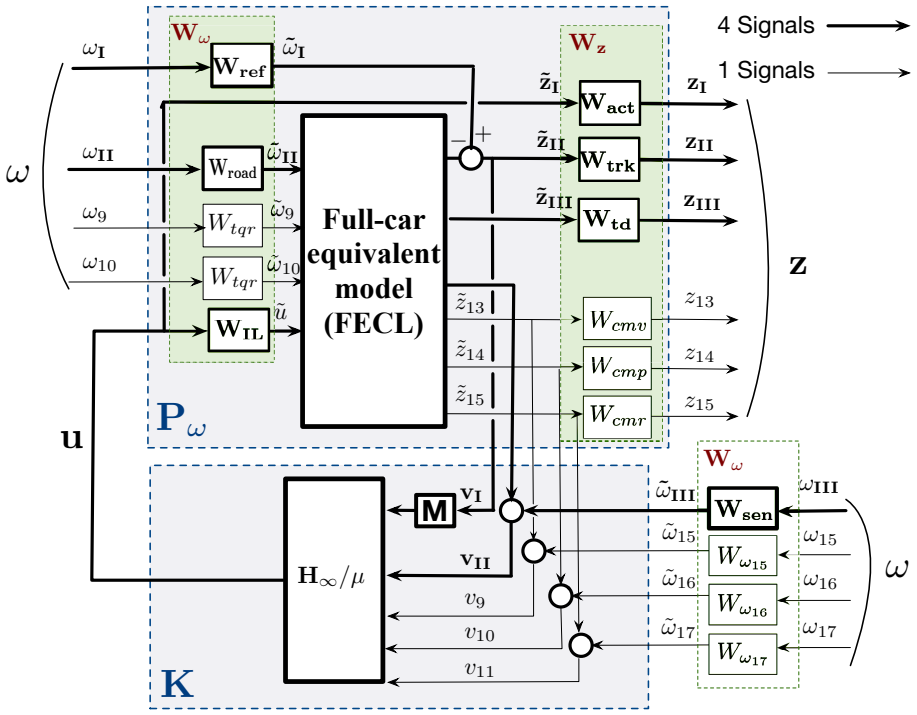


Figure 3.4: Interconnection for H_∞ control for the GT with SAVGS full car, where the signals and blocks are explained in (3.6)-(3.15)**.**

The unweighted signals already defined ($\tilde{\mathbf{w}}$, $\tilde{\mathbf{z}}$, and $\tilde{\mathbf{u}}$) are weighted by constant or frequency-dependent weighting functions, which are carefully tuned to achieve the desired performance objectives.

The weighting functions, described next, are parameterised in terms of their DC gain and cut-off frequencies, which scale the importance level between different objectives and filter the signals at their frequencies of interests, respectively.

3.3.1.1.1 Selection of input weighting functions

Input weights are related to the maximum expected value of the input signals, $\tilde{\mathbf{w}}$ and $\tilde{\mathbf{u}}$, shown in Figure 3.4. The constant weights selected for road height rate changes, and pitch and roll torques are:

$$\begin{aligned} W_{road,\,i} &= 0.25, \quad i = 1, \ldots, 4, \\ W_{tqp} &= 4050, \; W_{tqr} = 2700, \end{aligned} \tag{3.12}$$

where $i = 1, \ldots, 4$ represents the index of each vehicle corner, in the order: front left, front right, rear left and rear right. The frequency-dependent weights for exogenous references of the linear equivalent actuator displacements are selected as low pass filters with 1 Hz cut-off frequency and the DC gain is obtained by the their maximum value ($\approx 0.02\,\mathrm{m}$), related to the maximum single-link rotation ($\theta_{SL} = 0^\circ$ or 180°). Hence, the weights for the exogenous linear equivalent actuator displacements references are defined as:

$$W_{ref,\,i} = 0.02 \cdot \frac{1}{\frac{1}{(2\pi \cdot 1)}s + 1}, \quad i = 1, \ldots, 4. \tag{3.13}$$

Weighting functions for sensor noise, $W_{w_{15}}$, $W_{w_{16}}$, $W_{w_{17}}$, and $\mathbf{W_{sen}}$, are designed to account for the noise spectrum of the chassis acceleration and suspension deflection (displacement) sensors, which are:

$$\begin{aligned} W_{w_j} &= 0.5, \quad j = 15, 16, 17, \\ W_{sen,\,i} &= 0.01, \quad i = 1, \ldots, 4. \end{aligned} \tag{3.14}$$

Since the rapid change of the single-link angular velocity cannot be accurately tracked beyond a certain frequency (18 Hz), based on actuator limitations, a first-order transfer function is introduced to represent the nominal dynamics of the single-link actuators:

$$W_{IL,\,i} = \frac{1}{\frac{1}{(2\pi\cdot 17.8)}s + 1}, \quad i = 1, \ldots, 4. \tag{3.15}$$

3.3.1.1.2 Selection of output weighting functions

The output weights applied on the cost signals, $\tilde{\mathbf{z}}$, are chosen to shape the performance and objectives. $W_{act,\,i}$ are defined as high pass filters to penalise the high-frequency components of the linear equivalent actuator speeds and restrict the control bandwidth of the actuators:

$$W_{act,\,i} = \frac{1}{6.49} \cdot \frac{\frac{1}{(2\pi\cdot 10)^2}s^2 + \frac{2}{2\pi\cdot 10}s + 1}{\frac{1}{(2\pi\cdot 100)^2}s^2 + \frac{2}{2\pi\cdot 100}s + 1}, \quad i = 1, \ldots, 4. \tag{3.16}$$

$W_{trk,\,i}$ are defined as low pass filters, which ensure that the SL angles track the command positions at low or zero frequencies, without overlapping with the frequency ranges (2-10 Hz) of other higher frequency objectives, such as the control of chassis accelerations and tire deflections:

$$W_{trk,\,i} = 0.006 \cdot \frac{\frac{1}{(2\pi\cdot 120)}s + 1}{\frac{1}{(2\pi\cdot 0.3)}s + 1}, \quad i = 1, \ldots, 4. \tag{3.17}$$

In terms of the main control objectives, the cut-off frequencies of the ride comfort weighting functions, W_{cmv}, W_{cmp}, and W_{cmr}, are selected to be 5 Hz, 0.8 Hz, and 1 Hz respectively, according to the human body sensitivity to vibrations [72]. Road holding weights, W_{tdi}, are chosen as band pass filters to penalise the road

disturbances within 1-5 Hz:

$$\begin{aligned} W_{cmv} &= \frac{7}{\frac{1}{(2\pi\cdot 5)}s+1}\,,\; W_{cmp} = \frac{4.5}{\frac{1}{(2\pi\cdot 0.8)}s+1}, \\ W_{cmr} &= \frac{1.45}{\frac{1}{(2\pi\cdot 1)}s+1}, \\ W_{td3} &= W_{td4} = 2W_{td1} = 2W_{td2} = \frac{\frac{1.2}{(2\pi\cdot 0.001)}s+1.2}{\frac{1}{(2\pi)^2\cdot 5}s^2+\frac{4}{2\pi\cdot 3}+1}. \end{aligned} \tag{3.18}$$

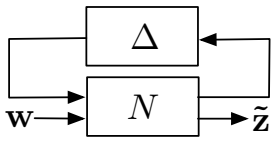
In addition, the integrator blocks (block **M** in Figure 3.4) are included to obtain a zero tracking error for the linear equivalent actuator displacement:

$$M_i = \frac{1}{s}, \quad i = 1, \ldots, 4. \tag{3.19}$$

With the tuned input and output weighting functions, the H_∞ control scheme can be synthesised by using the MATLAB command `hinfsyn`. However, H_∞ control only deals with the problem of finding a controller for a known system and produces more conservative controllers that might not be able to meet the design specifications. μ-synthesis extends the H_∞ control to the case when the system is uncertain and minimises the worst-case gain given the uncertainty description. Additionally, by using μ-synthesis, the performance of the system can be further improved while still satisfying the requirements that the induced disturbances from the uncertainty remain below a certain level.

3.3.1.2 μ-synthesis control

The μ-synthesis control allows to design a multi-variable optimal robust controller for complex linear systems with any type of uncertainty in their structure, such as structured or unstructured uncertainty. As shown in Figure 3.5, the objective of μ-synthesis is to calculate a robust controller for the uncertain open-loop plant model via the *D-K* algorithm [40]. In the present work, the variations of



(b)

Figure 3.5: μ-synthesis: (a) extended generalised regulator, and (b) analysis framework [40]. P is a time-invariant state-space representation of a linear plant, K is a μ-synthesis based controller, Δ is a structured uncertainty block diagonal matrix, w correspond to system exogenous disturbances, and $\tilde{z}$ to the cost signals to be minimised.

The system N in Figure 3.5 is defined as follows:

$$N(s) = F_l(P(s), K(s)) = \begin{bmatrix} N_{11}(s) & N_{12}(s) \\ N_{21}(s) & N_{22}(s) \end{bmatrix}, \tag{3.20}$$

where F_l denotes a lower linear fractional transform of control plant P and robust controller K.

Then the general framework is reduced to Figure 3.5(b), and the formulation becomes:

$$\tilde{\mathbf{z}} = F_u(N, \Delta)\cdot\mathbf{w} = [N_{22} + N_{21}\Delta(I - N_{11}\Delta)^{-1}N_{12}]\cdot\mathbf{w}, \tag{3.21}$$

where the upper linear fractional transformation, $F_u(N, \Delta)$, is the closed-loop system from exogenous disturbance ($\mathbf{w}$) to cost signals ($\tilde{\mathbf{z}}$) to be minimised.

The structured singular value, μ, is used to evaluate robust stability and performance of a system, N. Mathematically,

$$\mu(N)^{-1} \triangleq \min_{\Delta} \left\{ \bar{\sigma}(\Delta) | det(I - N\Delta) = 0 \right\}, \tag{3.22}$$

in which μ is defined as the inverse of the largest singular value $\bar{\sigma}$, and Δ is a structured uncertainty block diagonal matrix, which in the present work is defined as:

$$\Delta = \begin{bmatrix} \delta M_s & 0 & 0 \\ 0 & \delta c_{eqf} & 0 \\ 0 & 0 & \delta c_{eqr} \end{bmatrix}, \tag{3.23}$$

where the perturbation parameters δM_s, δc_{eqf} and δc_{eqr} are defined previously in (3.2). Δ is obtained to make the system N marginally stable.

In μ-synthesis control, the D-K iteration method integrates two optimisation problems and solves them by fixing either the variable $F(s)$ or the variable $D(s)$ by utilising H_∞ control and μ-synthesis approaches respectively. The upper bound of μ is given by:

$$\mu(N) \leq \min_{D \in \mathcal{D}} \bar{\sigma}(DND^{-1}), \tag{3.24}$$

where $\mathcal{D}$ is the scaling set of nonlinear matrices (D) that satisfy $D\Delta = \Delta D$ [40]. The control problem is to find a controller that minimises this aforementioned upper bound, which means solving the double minimisation given by:

$$\min_K \left(\min_{D \in \mathcal{D}} \left\| DN(K)D^{-1} \right\|_\infty \right). \tag{3.25}$$

The minimisation is solved alternately with respect to K and D. The D matrix is initialised to a transfer matrix with appropriate structure (i.e. identity matrix) and the D-K iteration algorithm is summarised by the following steps:

i. Fix the matrix $D(s)$, and the H_∞-optimal controller $K(s)$ that minimises γ can be synthesised:

$$\gamma = \min_K \left\| DN(K)D^{-1} \right\|_\infty. \tag{3.26}$$

ii. Hold $K(s)$ obtained from step i fixed and solve the following minimisation prob-

lem for $D(j\omega)$ at each frequency:

$$\min_{D} \bar{\sigma}(DN(K(s))D^{-1}). \tag{3.27}$$

iii. Construct a minimum phase system transfer function $D(s)$ by using the magnitude of the elements of $D(j\omega)$ and go to step i.

The stopping criteria of the D-K iteration are when $\left\|DN(K)D^{-1}\right\|_{\infty} \leq 1$ is met, or $\left\|DN(K)D^{-1}\right\|_{\infty}$ reaches its minimum value.

The interconnection and weights for the H_{∞} control synthesis shown in Figure 3.4 are applicable for the μ-synthesis as well. The weighting function parameter values chosen for the H_{∞} control synthesis in Section 3.3.1.1 are found to be beneficial and applied to the μ-synthesis also.

To perform a comprehensive comparison to the synthesised H_{∞} controller, three different μ-synthesis controllers are designed by means of the MATLAB command `dksyn`, with accommodating: i) only the sprung mass uncertainty (μ_{mass}), ii) only the suspension damping uncertainty ($\mu_{damping}$), and iii) both the sprung mass and the suspension damping uncertainties ($\mu_{combined}$).

3.3.2 PALS μ-synthesis-based control scheme

In this subsection, with the derived linear equivalent model of the PALS full car (Subsection 2.2.4.4), the μ-synthesis control (detailed in Subsection 3.3.1.2) is developed to attenuate the influence from external disturbances to the objective errors by synthesising a solution with stability and performance robustness. Figure 3.6 shows the μ-synthesis-based control configuration with the linear equivalent model of the PALS-retrofitted full car ($P_{\mathbf{w}}$ is the augmented linear equivalent full car model of P), with disturbance signals, cost signals, manipulated variables, and measurements defined subsequently. As in the SAVGS case, The unweighted normalised system

disturbance inputs $\mathbf{w} = [\tilde{\mathbf{w}}_\mathbf{I}, \tilde{\mathbf{w}}_\mathbf{II}, \tilde{\mathbf{w}}_\mathbf{9}, \tilde{\mathbf{w}}_\mathbf{10}] = [\tilde{\mathbf{w}}_\mathbf{I}, \bar{\mathbf{w}}]$ are: 1) $\tilde{\mathbf{w}}_\mathbf{I} = \boldsymbol{F}^{(\boldsymbol{L})}_{\boldsymbol{RC^*}}$, the exogenous commands of the linear equivalent actuation force reference signal at low frequency level, 2) $\tilde{\mathbf{w}}_\mathbf{II} = \dot{\mathbf{z}}_{\boldsymbol{r}}$, the vertical road velocity of each wheel, 3) $\tilde{w}_9 = T_p$, the equivalent pitch torque arising from load transfer due to braking/acceleration, and 4) $\tilde{w}_{10} = T_r$, the equivalent roll torque induced by load transfer when cornering. The unweighted cost signals $\tilde{\mathbf{z}} = [\tilde{\mathbf{z}}_\mathbf{I}, \tilde{\mathbf{z}}_\mathbf{II}, \tilde{\mathbf{z}}_\mathbf{III}, \tilde{z}_{13}, \tilde{z}_{14}, \tilde{z}_{15}]$ to be minimised are: 1) $\tilde{\mathbf{z}}_\mathbf{I} = \boldsymbol{F}^{(\boldsymbol{H})}_{\boldsymbol{RC^*}}$, are the high frequency linear equivalent actuation forces at each corner, 2) $\tilde{\mathbf{z}}_\mathbf{II} = \boldsymbol{F}^{(\boldsymbol{L})}_{\boldsymbol{RC^*}} - \boldsymbol{F}_{\boldsymbol{RC}}$, the tracking errors of the linear equivalent actuation force, 3) $\tilde{\mathbf{z}}_\mathbf{III} = \boldsymbol{\Delta l_t}$, the road holding related variables, which are the vertical tire deflections at each corner, and 4) the ride comfort related variables, $\tilde{z}_{13}$-$\tilde{z}_{15} = [\ddot{z}_s, \ddot{\theta}, \ddot{\phi}]$, which are the CMC vertical, chassis pitch and chassis roll accelerations. The measurement signals $\mathbf{y}^T = [\mathbf{y}_\mathbf{I}, \mathbf{y}_\mathbf{II}, y_9, y_{10}, y_{11}] = [\boldsymbol{F}^T_{\boldsymbol{RC}}, \boldsymbol{\Delta l}^T_{\boldsymbol{s}}, \ddot{z}_s, \ddot{\theta}, \ddot{\phi}]$ are selected based on the sensor availability and integration feasibility. The control signals are defined as $\mathbf{u} = \boldsymbol{F}^{(\boldsymbol{H})}_{\boldsymbol{RC^*}}$.

The input weighting functions relate to the maximum expected value of the input signals $\mathbf{w}$ and $\tilde{\mathbf{u}}$. Constant weights chosen for disturbance signals (rate of road height, pitch and roll torque) aim to normalise the inputs by removing the discrepancy of physical units:

$$\begin{aligned} W_{rd,\,i} &= 0.25, \quad i = 1, \ldots, 4, \\ W_{tqp} &= 4050, \;\; W_{tqr} = 2700, \end{aligned} \tag{3.28}$$

where as in the SAVGS case, $i = 1, \ldots, 4$ represents the index of each vehicle corner, in the order: front left, front right, rear left and rear right. The unit influence of $\boldsymbol{F}_{\boldsymbol{RC}}$ is normalised by introducing $W_{ref,\,i}$, which is tuned and adopted as follows:

$$W_{ref,\,i} = max\,|F_{RCi}| = 1800, \quad i = 1, \ldots, 4. \tag{3.29}$$

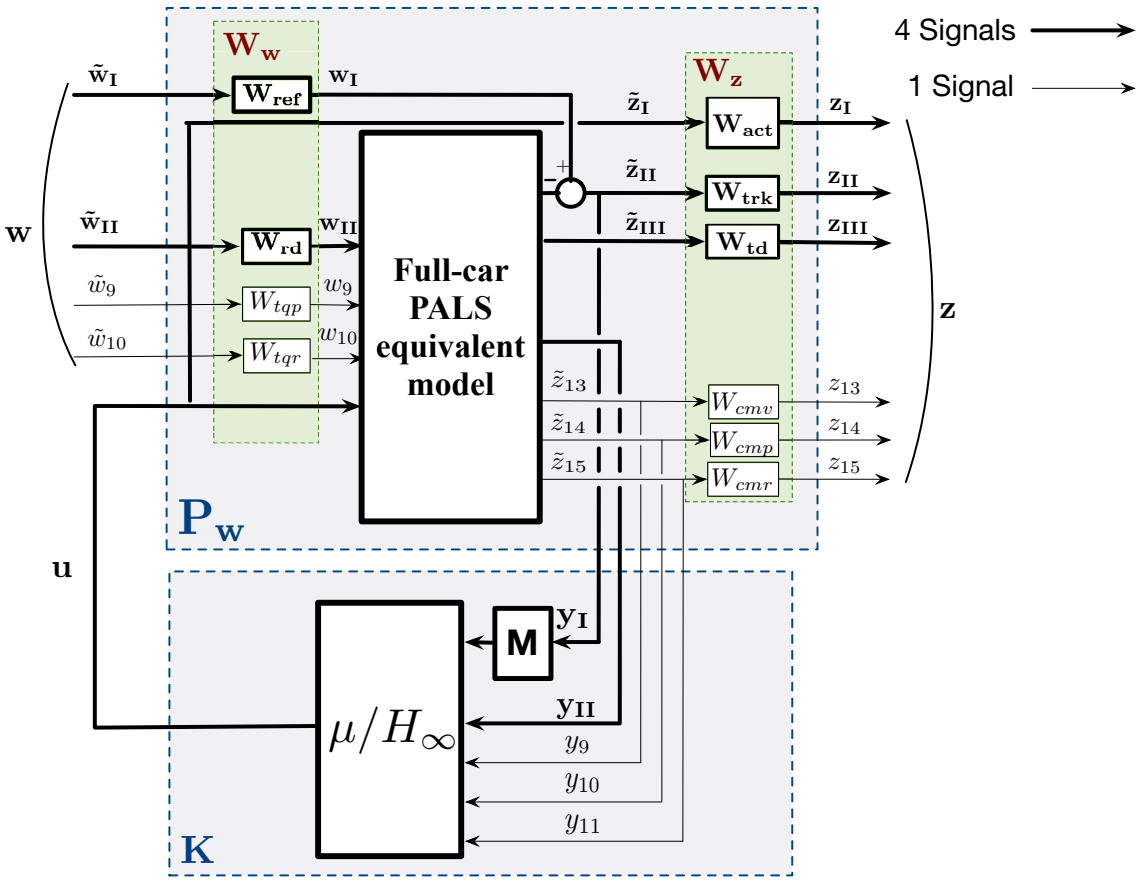


Figure 3.6: Interconnection for μ-synthesis control for the SUV with PALS full car.

$[W_{act,\,i}, W_{trk,\,i}, W_{tdi}, W_{cmv}, W_{cmp}, W_{cmr}]$ are the weighting functions working on the cost signals $\tilde{\mathbf{z}}$, which indicate the relative importance among different objectives. To penalise the high speeds (frequencies) for the linear equivalent actuators, $W_{act,\,i}$ are defined as high pass filters, thus ensuring the power and torque limits of the actuators are not exceeded:

$$W_{act,\,i} = \frac{1}{700} \cdot \frac{\frac{1}{(2\pi\cdot 10)^2}s^2 + \frac{2}{2\pi\cdot 10}s + 1}{\frac{1}{(2\pi\cdot 100)^2}s^2 + \frac{2}{2\pi\cdot 100}s + 1}, \quad i = 1, \ldots, 4. \tag{3.30}$$

$W_{trk,\,i}$ are defined approximately as integrators (with a pole at a very low frequency for better tuning). These guarantee that the desired reference signals are followed

by the actuation force of the rotary actuators at low or zero frequencies, for merging with the low frequency attitude control by the PID controller, as will be described in the next Section, without overlapping with other higher frequency (2-10 Hz) objectives including the chassis acceleration and tire deflections control:

$$W_{trk,\,i} = \frac{1}{0.1} \cdot \frac{1}{\frac{1}{(2\pi \cdot 0.001)}s + 1}, \quad i = 1, \ldots, 4. \tag{3.31}$$

As in the SAVGS case, two of the main control objectives in this subsection are to enhance ride comfort and road holding. In terms of ride comfort, the major target is to minimise the CMC vertical, chassis pitch and chassis roll accelerations, while for road holding, the aim is to penalise the dynamic tire deflections at a certain frequency range. More specifically, according to the human body sensitivity bandwidth in the vertical direction (0.5 - 8 Hz) and rotational direction (0.5 - 4 Hz), respectively, detailed in [72], the cut-off frequencies of the ride comfort weighting functions, W_{cmv}, W_{cmp}, and W_{cmr}, are selected to be 20 Hz, 1 Hz, and 1 Hz respectively. The frequency weights, W_{tdi}, representing road holding performance are defined (after some tuning) as band pass filters to penalise the road disturbances within 1-5 Hz. The tuning of these weights is based on trial and error at the level of simulating with the nonlinear model after implementing the synthesised controller.

$$\begin{aligned} W_{cmv} &= \frac{50(\frac{1}{(2\pi \cdot 160)}s + 1)}{\frac{1}{(2\pi \cdot 20)}s + 1}\,, \; W_{cmp} = \frac{25}{\frac{1}{(2\pi \cdot 1)}s + 1}, \\ W_{cmr} &= \frac{25}{\frac{1}{(2\pi \cdot 1)}s + 1}, \\ W_{td1} &= W_{td2} = W_{td3} = W_{td4} = \frac{\frac{10}{(2\pi \cdot 0.001)}s + 10}{\frac{1}{(2\pi)^2 \cdot 3}s^2 + \frac{8}{2\pi \cdot 4} + 1}. \end{aligned} \tag{3.32}$$

In addition, block **M** in Figure 3.6 is introduced to include a free integrator to obtain a zero tracking error for the linear equivalent actuation force [40], and it is

tuned as

$$M_i = \frac{\frac{1}{(2\pi\cdot 20)}s + 1}{s}, \quad i = 1, \ldots, 4. \tag{3.33}$$

3.4 Numerical Simulations and analysis

In this section, numerical simulations are performed with the nonlinear multi-body full-car SAVGS/PALS model. The performance of the μ-synthesis controllers proposed in Section 3.3.1.2 is tested with the nonlinear full-car model for a group of typical road profiles. For comparison purposes, the passive and H_∞-controlled multi-body model cases are also simulated. The typical ISO driving manoeuvres selected to be tested are speed bump road and random class C road.

3.4.1 SAVGS Multi-body Full-car

With the multi-body PALS full-car model built in Subsection 2.2.3.1 and control scheme synthesised in Section 3.3.1.2, nonlinear simulations are performed with the multi-body model with a forward speed of 100 km/h, a nominal angle offset of $\theta_{SL} = 90^\circ$ and a maximum driving power of 500 W for each SL actuator. The typical random class C road (as defined in [30]) is tested only for SAVGS.

Numerical simulations are performed to evaluate two aspects of performance: the benefits of accounting for the suspension damping nonlinearity (aspect A) and for the sprung mass variation due to payload changes (aspect B) as parametric uncertainties in the linear control synthesis. Three simulation cases are performed, each with a different case of sprung mass, M_s: a) nominal sprung mass ($M_s = M_{\text{nom}}$) to evaluate aspect A, b) maximum sprung mass ($M_s = M_{\text{max}}$) to evaluate both aspects A and B, and c) swept sprung mass ($M_s = M_{\text{nom}}$ to M_{max}) to evaluate aspect B. The ride comfort related variables of the CMC vertical acceleration ($\ddot{z}_s$), the chassis pitch

($\ddot{\theta}_s$) and roll ($\ddot{\phi}_s$) accelerations, and the road holding related variables of the tire deflections (Δl_{ti}) are considered as the evaluation indexes.

3.4.1.1 Evaluation of aspect A (nominal sprung mass)

The PSD plots of $\ddot{z}_s$, $\ddot{\theta}_s$ and $\ddot{\phi}_s$, and Δl_{t1} and Δl_{t3} in the case of $M_s = M_{\text{nom}}$ are shown in Figs. 3.7 and 3.8 respectively, and their root mean square (RMS) and peak-to-peak (PTP) values in the time domain are listed in Tables 3.1 and 3.2 respectively. Due to the symmetry of the chassis geometry, the responses of Δl_{t2} and Δl_{t4} are respectively similar to those of Δl_{t1} and Δl_{t3}, and are not shown here. It can be seen that the ride comfort and the road holding are significantly improved by all the active control cases as compared to the passive system, while the μ-synthesis controller μ_{mass} has nearly the same performance as that of the H_∞ controller (for example, 6 dB reduction at 2 Hz in the case of CMC vertical acceleration, with respect to the passive system) as would be expected.

In this simulation there is no variation of the sprung mass from its nominal value and neither of the H_∞ and μ_{mass} controllers take the suspension damping uncertainty into account. In contrast, the $\mu_{damping}$ and $\mu_{combined}$ controllers, which both account for the damping uncertainty, achieve a better performance than the H_∞ controller. This can be observed in all the PSD plots in Figs. 3.7 and 3.8 in the range 1-4 Hz, especially in the case of $\ddot{z}_s$ for which they achieve a reduction of 9 dB and 10 dB respectively at 2Hz, as compared to the passive case, and consequently 3-4 dB reduction as compared to the H_∞ control case. The improvement offered by $\mu_{combined}$ over the passive and H_∞ controller cases, in terms of time-domain RMS and peak-to-peak values, is further observed in Tables 3.1 and 3.2.

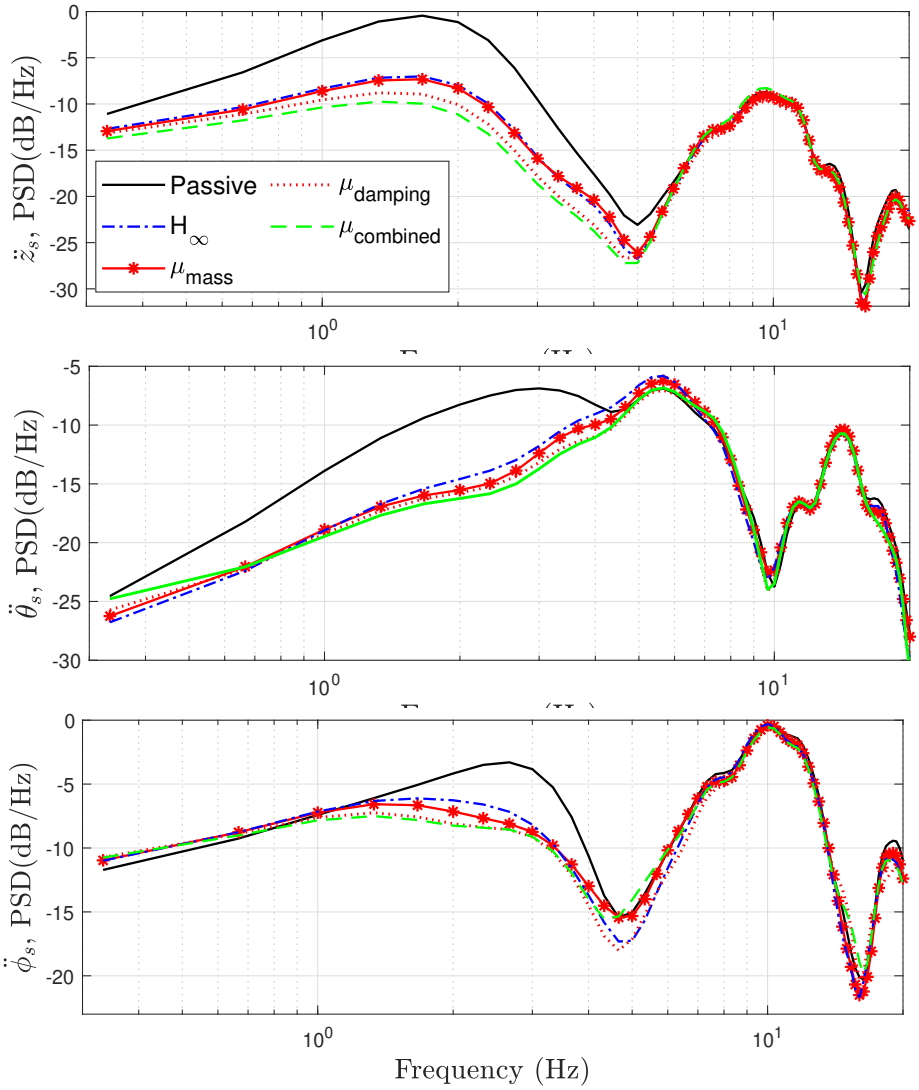


Figure 3.7: Numerical simulation results in the case of $M_s = M_{\text{nom}}$ for the GT with SAVGS full car: the PSD of $\ddot{z}_s$, $\ddot{\theta}_s$ and $\ddot{\phi}_s$ with the H_∞ and different μ-synthesis controllers when the vehicle is running over ISO random road class C at a constant forward speed of 100 km/h.

3.4.1.2 Evaluation of both aspects A and B (maximum sprung mass)

Figures 3.9 and 3.10 illustrate the PSDs of $\ddot{z}_s$, $\ddot{\theta}_s$ and $\ddot{\phi}_s$, and Δl_{t1} and Δl_{t3} in the case of $M_s = M_{\text{max}}$.

As it can be seen, in this case the performance improvement of the H_∞ scheme as compared to the passive system (for example, 4.3 dB reduction at 2 Hz in terms

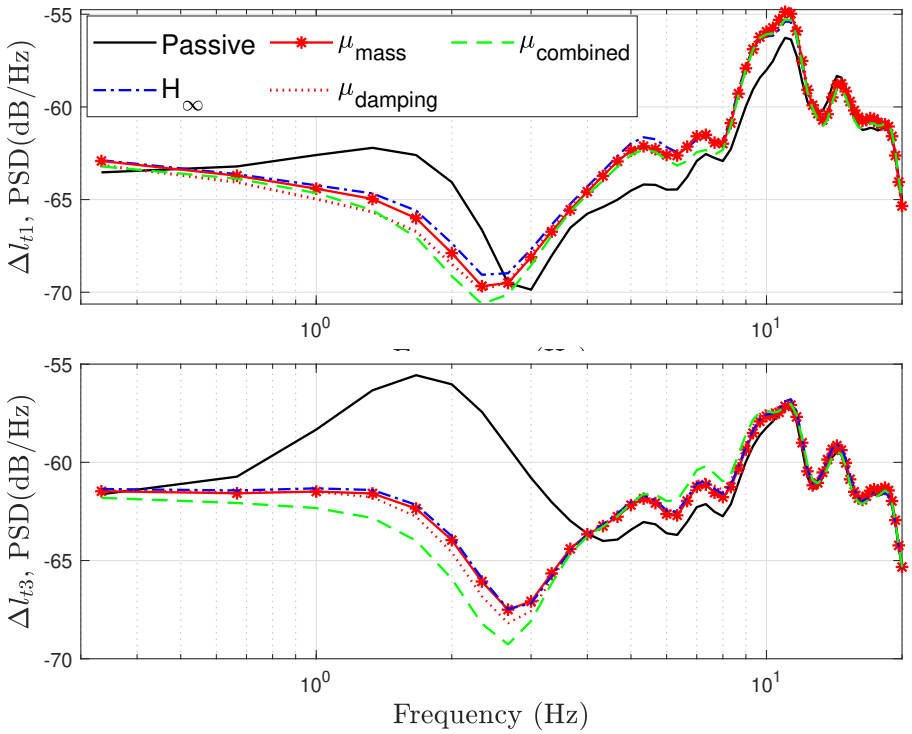


Figure 3.8: Numerical simulation results in the case of $M_s = M_{\text{nom}}$ for the GT with SAVGS full car: the PSD of Δl_{t1} and Δl_{t3} with the H_∞ and different μ-synthesis controllers when the vehicle is running over ISO random road class C at a constant forward speed of 100 km/h.

Table 3.1: RMS and peak-to-peak values of the $\ddot{z}_s$, $\ddot{\theta}_s$ and $\ddot{\phi}_s$ with different controllers, $M_s = M_{\text{nom}}$ for the GT with SAVGS full car, when the vehicle is running over ISO random road class C at a constant forward speed of 100 km/h.

	Parameter	Passive	H_∞	$\mu_{combined}$
RMS	$\ddot{z}_s$	1.3603	0.9507(-30%)	0.8932(-34%)
	$\ddot{\theta}_s$	1.1694	1.0768(-8%)	1.0051(-14%)
	$\ddot{\phi}_s$	2.4712	2.3030(-8%)	2.2106(-10%)
PTP	$\ddot{z}_s$	3.8553	2.7168(-29%)	2.5445(-34%)
	$\ddot{\theta}_s$	2.7243	2.5107(-8%)	2.2595(-17%)
	$\ddot{\phi}_s$	7.1284	6.5581(-8%)	6.3443(-11%)

of CMC vertical acceleration) is not as great as when $M_s = M_{\text{nom}}$ (see Section 3.4.1.1), due to the lack of robustness of this scheme to variations in the sprung mass. However, in the case of $M_s = M_{\text{max}}$ both the uncertainties of the sprung mass and the suspension damping are presented; for increased M_s the damper is forced

Table 3.2: RMS and peak-to peak values of the Δl_{t1} and Δl_{t3} with different controllers, $M_s = M_{\mathbf{nom}}$ for the GT with SAVGS full car, when the vehicle is running over ISO random road class C at a constant forward speed of 100 km/h.

	Parameter	Passive	H_∞	$\mu_{combined}$
RMS	$\lvert\Delta l_{t1}\rvert$	0.0043	0.0043(+0%)	0.0044(+2%)
	$\lvert\Delta l_{t3}\rvert$	0.0046	0.0044(-4%)	0.0042(-8%)
PTP	$\lvert\Delta l_{t1}\rvert$	0.0146	0.0149(+2%)	0.0140(+4%)
	$\lvert\Delta l_{t3}\rvert$	0.0143	0.0139(-3%)	0.0130(-9%)

to operate in a wider range of damper speeds, whereby the damper experiences more nonlinear behavior. As such, significant reductions are clearly observed for the μ_{mass} controller (-7.3 dB at 2 Hz for $\ddot{z}_s$ as compared to the passive case), and for the $\mu_{damping}$ controller (-8.7 dB at 2 Hz for $\ddot{z}_s$ as compared to the passive case). The best attenuation of all control schemes is achieved by the $\mu_{combined}$ controller (-10 dB at 2 Hz for $\ddot{z}_s$ as compared to the passive case). Similar conclusions can be drawn from the time domain comparison of RMS and peak-to-peak values of the passive, H_∞-controlled and $\mu_{combined}$-controlled systems, as shown in Tables 3.3 and 3.4.

Table 3.3: RMS and peak-to-peak values of the $\ddot{z}_s$, $\ddot{\theta}_s$ and $\ddot{\phi}_s$ with different controllers, $M_s = M_{\mathbf{max}}$ for the GT with SAVGS full car, when the vehicle is running over ISO random road class C at a constant forward speed of 100 km/h.

	Parameter	Passive	H_∞	$\mu_{combined}$
RMS	$\ddot{z}_s$	1.3692	1.0680(-22%)	0.8218(-37%)
	$\ddot{\theta}_s$	1.1672	1.0971(-6%)	1.0472(-10%)
	$\ddot{\phi}_s$	2.4602	2.3340(-5%)	2.2703(-8%)
PTP	$\ddot{z}_s$	3.6165	2.8967(-20%)	2.2944(-37%)
	$\ddot{\theta}_s$	2.6946	2.5781(-4%)	2.4103(-11%)
	$\ddot{\phi}_s$	7.0830	6.8417(-3%)	6.4502(-9%)

Time histories of $\ddot{z}_s$ for the passive and two cases of controlled system are presented in Figure 3.11. It can be seen that the H_∞ controller attenuates $\ddot{z}_s$ considerably as compared to the passive case, while the $\mu_{combined}$ controller provides further enhancement over the H_∞ controller.

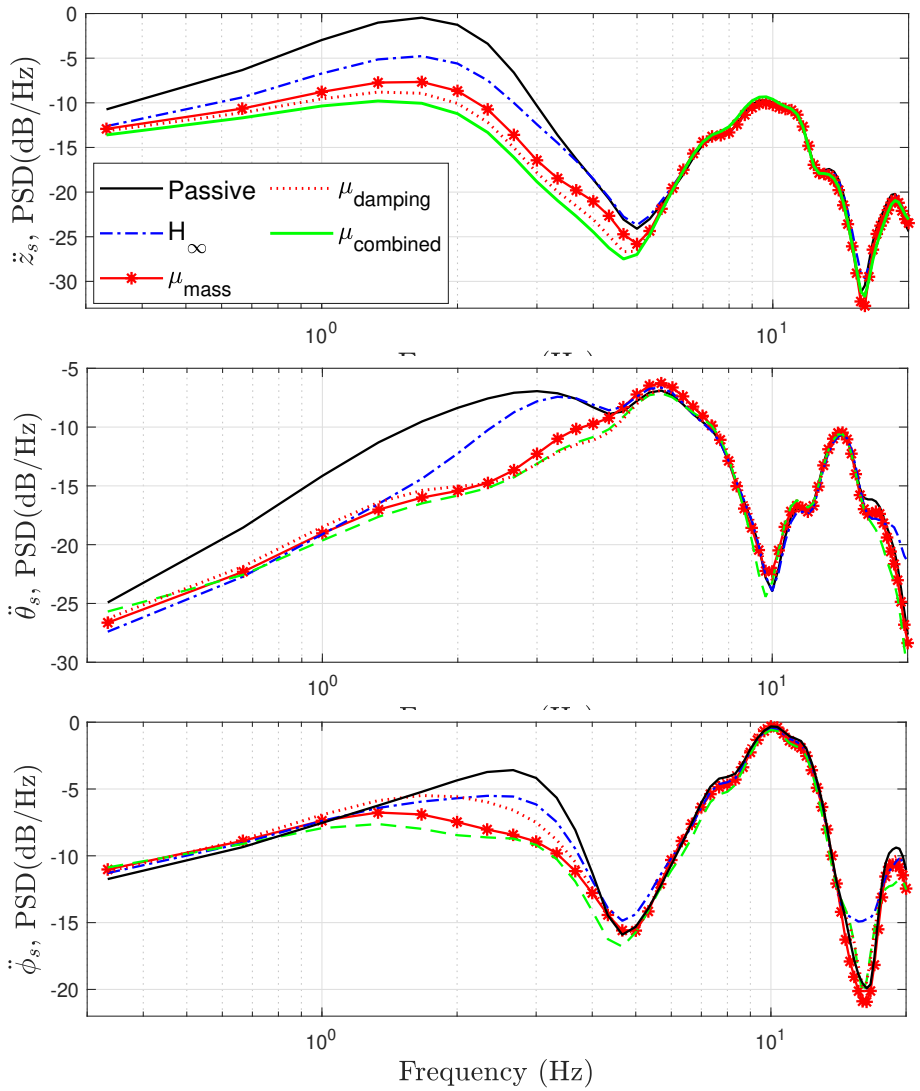


Figure 3.9: Numerical simulation results in the case of $M_s = M_{\max}$ for the GT with SAVGS full car: the PSD of $\ddot{z}_s$, $\ddot{\theta}_s$ and $\ddot{\phi}_s$ with the H_∞ and different μ-synthesis controllers when the vehicle is running over ISO random road class C at a constant forward speed of 100 km/h.

3.4.1.3 Evaluation of aspect B (swept sprung mass)

Figure 3.12 shows the PSD values of the $\ddot{z}_s$ at the fixed frequency of 2 Hz for M_s swept from M_{nom} to $M_{\max}$ in steps of 30 kg. Thus, the ride comfort performance difference between the H_∞ and two μ-synthesis controllers (μ_{mass} and $\mu_{combined}$), as the sprung mass is varied, is indicated. As compared to the passive case and for the whole M_s range, the μ-combined controller maintains the largest ride comfort

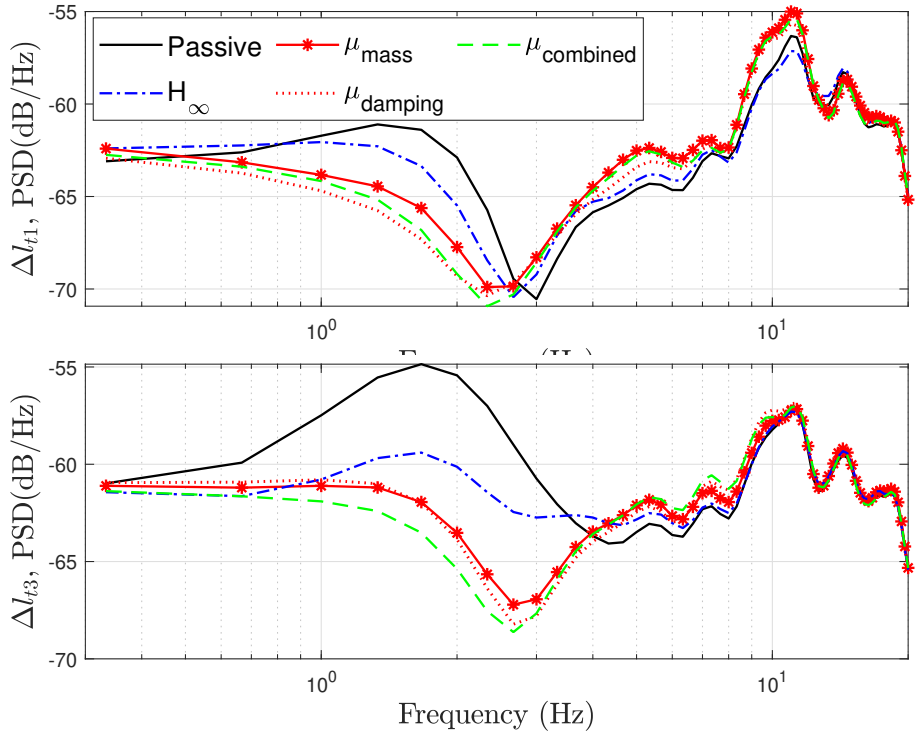


Figure 3.10: Numerical simulation results in the case of $M_s = M_{\max}$ for the GT with SAVGS full car: the PSD of Δl_{t1} and Δl_{t3} with the H_∞ and different μ-synthesis controllers when the vehicle is running over ISO random road class C at a constant forward speed of 100 km/h.

Table 3.4: RMS and peak-to-peak values of the Δl_{t1} and Δl_{t3} with different controllers, $M_s = M_{\max}$ for the GT with SAVGS full car, when the vehicle is running over ISO random road class C at a constant forward speed of 100 km/h.

	Parameter	Passive	H_∞	$\mu_{combined}$
RMS	$\lvert\Delta l_{t1}\rvert$	0.0043	0.0043(+0%)	0.0044(+2%)
	$\lvert\Delta l_{t3}\rvert$	0.0046	0.0044(-4%)	0.0042(-8%)
PTP	$\lvert\Delta l_{t1}\rvert$	0.0146	0.0149(+2%)	0.0140(+4%)
	$\lvert\Delta l_{t3}\rvert$	0.0143	0.0139(-3%)	0.0130(-9%)

performance enhancement (-10 dB), followed by the μ_{mass} controller (-7 dB). The H_∞ controller achieves the least improvement over the passive case and becomes less performing as M_s increases; it has the same performance as with the μ_{mass} scheme of -7 dB at $M_s = M_{\text{nom}}$, deteriorating almost linearly to -4 dB when $M_s = M_{\max}$. These results illustrate the improved robustness of the μ-synthesis control schemes

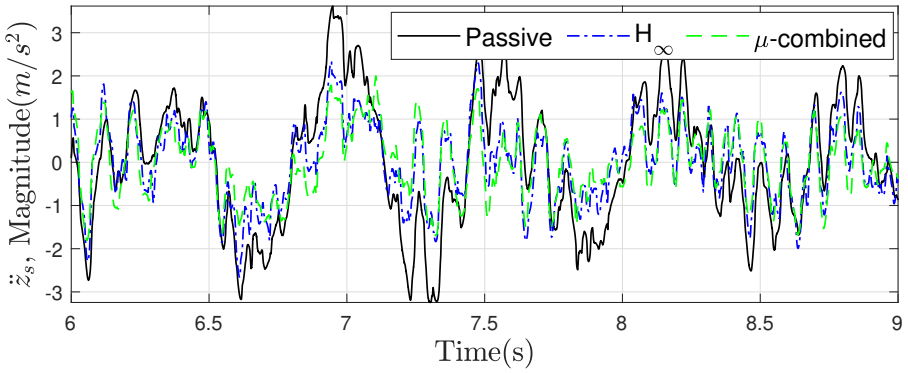


Figure 3.11: Numerical simulation results in the case of $M_s = M_{\max}$ for the GT with SAVGS full car: $\ddot{z}_s$ time histories for the passive, H_∞-controlled and $\mu_{combined}$-controlled systems when the vehicle is running over ISO random road class C at a constant forward speed of 100 km/h.

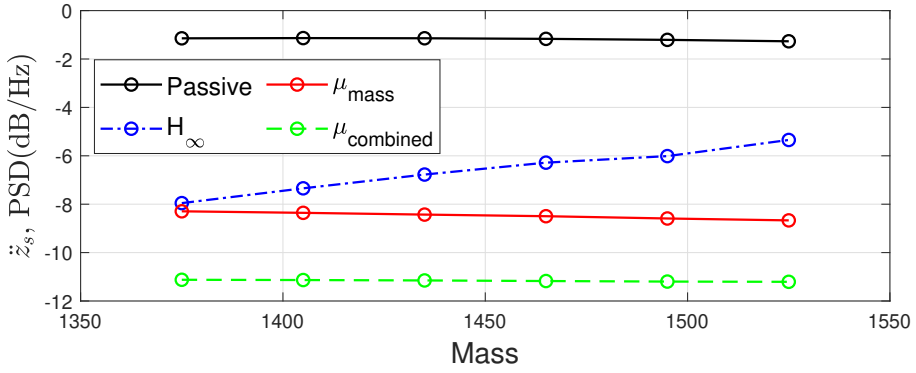


Figure 3.12: The PSD gain of $\ddot{z}_s$ at the frequency of 2 Hz for different values of M_s (swept from M_{nom} to $M_{\max}$ in 30 kg increments) for the GT with SAVGS full car when the vehicle is running over ISO random road class C at a constant forward speed of 100 km/h. The passive system, and H_∞ and different μ-synthesis control performances are compared.

as compared to the H_∞ scheme, for variations in the sprung mass.

3.4.2 PALS Multi-body Full-car

In this section, the multi-body PALS full-car model (built in Subsection 2.2.3.2) and control scheme (proposed in Section 3.3.1.2) are utilised. The ISO driving manoeuvres, containing random road class C and speed bump are utilised for the

investigation of high frequency vehicle vibration control in terms of ride comfort and road holding improvement.

The numerical simulations are therefore performed to evaluate the performance comparison: the benefits of accounting for the suspension damping nonlinearity and sprung mass variation as parametric uncertainties in the linear control synthesis, with high frequency case studies comparison between H_∞ control ('PALS-H_∞') and μ-synthesis-based control ('PALS-μ').

3.4.2.1 Nonlinear Simulations with Random Road

In the numerical simulation environment, the PALS-retrofitted full car is driven with a forward speed of 100 km/h, different road profiles (of same unevenness) against traveled distance are generated for the left and right side wheels respectively, and the traveled distance delay due to the wheelbase ($\alpha_f+\alpha_r$) occurs in the road profile seen by the rear axle as compared to the road profile seen by the front one. In the present work, Class C road is selected for simulation to validate the improvement of the ride comfort and road holding.

Figure. 3.13 shows numerical simulation results with three different sprung mass cases of a) nominal sprung mass ($M_s = M_{\text{nom}}$), b) maximum sprung mass ($M_s = M_{\text{max}}$), and c) minimum sprung mass ($M_s = M_{\text{min}}$), for ISO random road Class C. The evaluation indexes are selected as ride comfort related variables of the CMC vertical acceleration ($\ddot{z}_s$), the chassis pitch ($\ddot{\theta}_s$) and roll ($\ddot{\phi}_s$) accelerations, and the road holding related variables of the tire deflections (Δl_{t1}) at the human sensitive frequencies (1-8 Hz).

Figure 3.13 top-left reveals the PSDs of $\ddot{z}_s$, $\ddot{\theta}_s$ and $\ddot{\phi}_s$, and Δl_{t1} with the PALS-retrofitted full car in the case of $M_s = M_{\text{nom}}$. As it can be seen, all the active controllers give a notably improved performance in terms of the ride comfort and

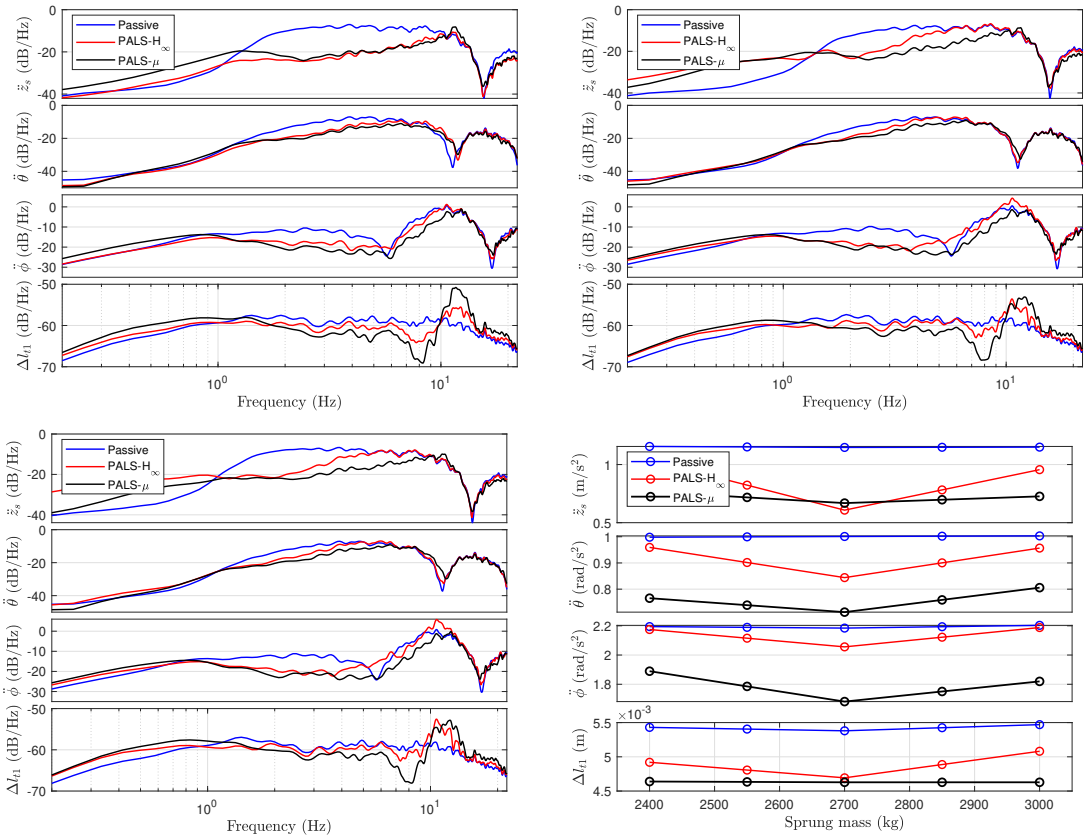


Figure 3.13: Numerical simulation results: the PSD gain of CMC vertical acceleration ($\ddot{z}_s$), pitch acceleration ($\ddot{\theta}_s$), roll acceleration ($\ddot{\phi}_s$) and tire deflection (Δl_{t1}) with the passive, 'PALS-H_∞' and 'PALS-μ' controllers in the sprung mass, M_s, cases of $M_{\mathbf{nom}}$ (top-left), $M_{\mathbf{min}}$ (top-right), and $M_{\mathbf{max}}$ (bottom-left), and the RMS value variation of $\ddot{z}_s$, $\ddot{\theta}_s$, $\ddot{\phi}_s$ and Δl_{t1} with the passive, 'PALS-H_∞' and 'PALS-μ' controllers for M_s swept from $M_{\mathbf{min}}$ to $M_{\mathbf{max}}$ in 150kg increments (bottom-right) when the vehicle is running over ISO random road class C at a constant forward speed of 100 km/h.

the road holding as compared to the passive system, in which the μ-synthesis controller 'PALS-μ' performs nearly the same as the 'PALS-H_∞' controller (for example, 12.4 dB and 14.1 dB reduction respectively at 4 Hz in the case of CMC vertical acceleration). The reason for the marginally better performance of the 'PALS-H_∞' controller in the present case is that it is designed based on nominal conditions, as compared to the 'PALS-μ' controller that is designed to be more conservative to address a wider range of conditions, as will be shown next.

The PSD plots of $\ddot{z}_s$, $\ddot{\theta}_s$ and $\ddot{\phi}_s$, and Δl_{t1} in the cases of $M_s = M_{\min}$ and $M_s = M_{\max}$

are respectively shown in Figure 3.13 top-right and Figure 3.13 bottom-left. It can be seen that with the variation of the sprung mass, the performance enhancement of the 'PALS-H_∞' controller as compared to the passive case (for example, 4.8 dB and 4.5 dB reduction in terms of $\ddot{z}_s$ at 4 Hz in the cases of $M_s = M_{\min}$ and $M_s = M_{\max}$, respectively) is not as great as when $M_s = M_{\text{nom}}$ due to the lack of robustness of the 'PALS-H_∞' controller in these case. In contrast, both sprung mass and suspension damping uncertainties take effect in these cases, in which the damper is forced to operate in a wider range of damper speeds, whereby the damper experiences more nonlinear behavior.

Therefore, as compared to 'PALS-H_∞' the reductions of $\ddot{z}_s$, $\ddot{\theta}_s$ and $\ddot{\phi}_s$, and Δl_{t1} for the 'PALS-μ' controller, which offers robustness against the uncertainties, can be observed (for example, -12.3 dB and -12.4 dB at 4 Hz for $\ddot{z}_s$ as compared to the passive case for the minimum and maximum sprung mass cases, respectively).

Similar conclusions can be drawn from the root mean square (RMS) quantities in the time domain with varied sprung mass, as detailed in Figure 3.13 bottom-right. It can be seen that $\ddot{z}_s$, $\ddot{\theta}_s$, $\ddot{\phi}_s$ and Δl_{t1} with 'PALS-μ' provide the largest performance enhancement when the sprung mass is varied to its upper and lower limit, while the improvement is marginal in the nominal mass case as compared to 'PALS-H_∞'. In particular, although the PSD plots in Figure 3.13 show that Δl_{t1} deteriorates at about 10 Hz with 'PALS-μ', the RMS value demonstrates that overall there is improvement. Moreover, Figure 3.14 shows the PSD value of the $\ddot{z}_s$ at the fixed frequency of 4 Hz for M_s swept from $M_{\min}$ to $M_{\max}$ in steps of 150 kg, which demonstrates the improved robustness of the μ-synthesis control scheme as compared to the H_∞ scheme for variations in the sprung mass.

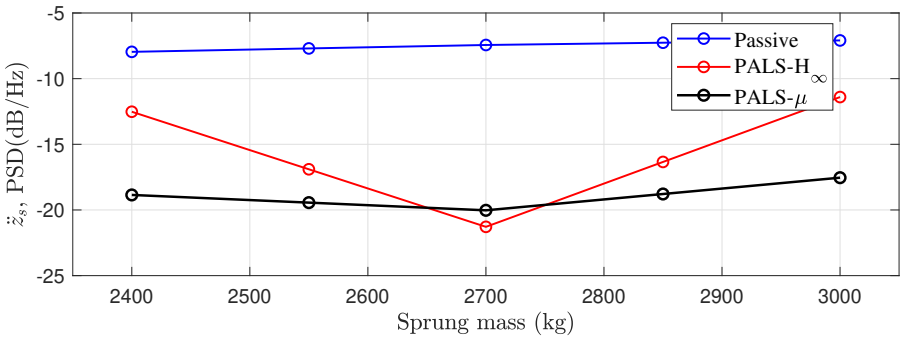


Figure 3.14: Numerical simulation results: the PSD gain of CMC vertical acceleration ($\ddot{z}_s$), at the frequency of 4 Hz for different values of M_s (swept from M_{min} to M_{max} in 150 kg increments) when the vehicle is driven over an ISO random road Class C at 100 km/h, for different cases of suspension control.

3.4.2.2 Nonlinear Simulations with Speed Bump

The ride comfort is mainly revealed by the CMC vertical and chassis pitch acceleration, as the roll motion is barely affected due to simultaneous excitation occurring on the two wheels of the same axle in the speed bump road profile.

Numerical simulation results with the PALS-retrofitted full car at a driving speed of 20 km/h over a speed bump with different cases of sprung mass are shown in Figure 3.15. Similarly to the random road cases, the 'PALS-H_∞' controller achieves its best improvement in the case of $M_s = M_{\text{nom}}$, which contributes 70% and 41% reduction in the peak-to-peak (PTP) value of $\ddot{z}_s$ and Δl_{t1}, respectively, as compared to the passive suspension, and becomes less performing as M_s is varied. The PTP values of $\ddot{z}_s$ and Δl_{t1} deteriorate to 28%, 17% and 22%, 18% in the cases of $M_s = M_{\text{min}}$ and $M_s = M_{\text{max}}$, respectively, as compared to passive suspension. 'PALS-μ' maintains the largest ride comfort and road holding performance enhancement for the whole M_s range cases, which for example reduces the PTP value of $\ddot{z}_s$ and Δl_{t1} by approximately 71% and 39% for the M_{nom} case (top-left plot in Figure 3.15), 73% and 40% for the M_{min} case (top-right plot in Figure 3.15), and 69% and 38% for the M_{max} case (bottom-left plot in Figure 3.15), which further illustrate the significant

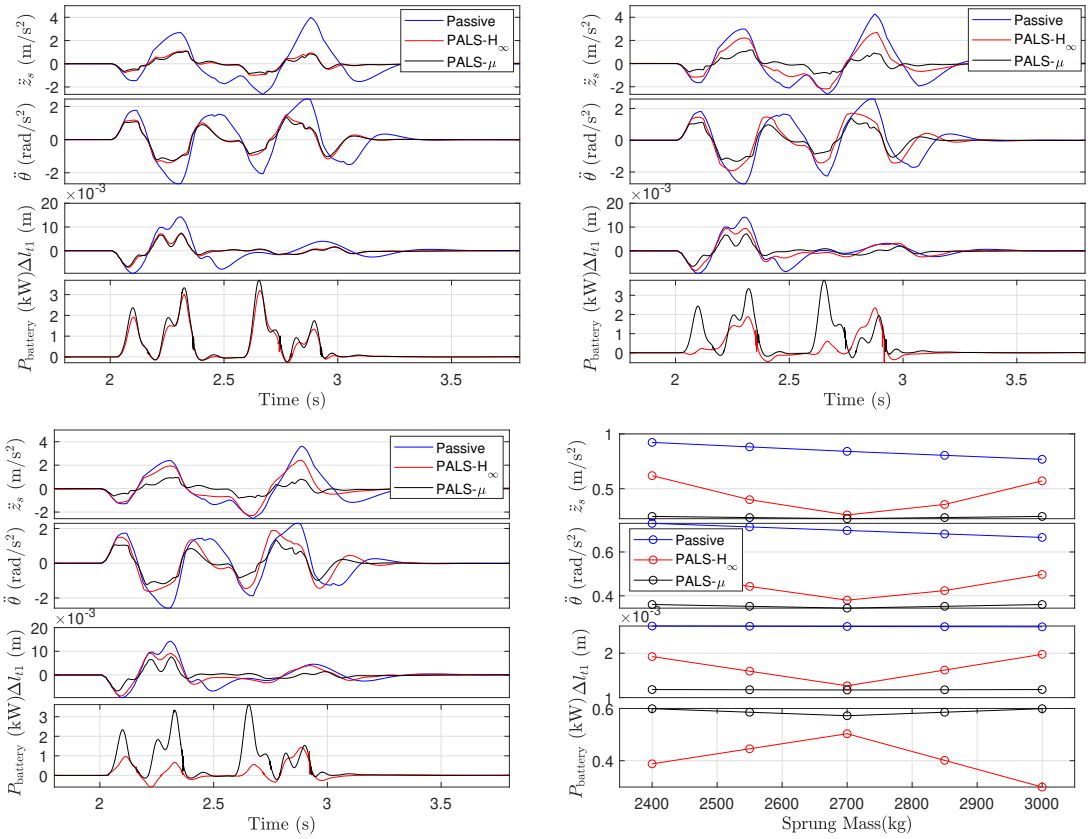


Figure 3.15: Numerical simulation results: the variation of CMC vertical acceleration ($\ddot{z}_s$), pitch acceleration ($\ddot{\theta}_s$), tire deflection (Δl_{t1}) and power consumption in the DC batteries ($P_{battery}$) with the passive, 'PALS-H_∞' and 'PALS-μ' controllers in the sprung mass, M_s, cases of $M_{\mathbf{nom}}$ (top-left), $M_{\mathbf{min}}$ (top-right), and $M_{\mathbf{max}}$ (bottom-left), and the RMS value variation of $\ddot{z}_s$, $\ddot{\theta}_s$, Δl_{t1} and $P_{battery}$ with the passive, 'PALS-H_∞' and 'PALS-μ' controllers for M_s swept from $M_{\mathbf{min}}$ to $M_{\mathbf{max}}$ in 150kg increments (bottom-right) when the vehicle is running over a bump of 0.05 m height and 2 m length at a constant forward speed of 20 km/h.

enhancement of μ-synthesis controller over the H_∞ controller. The improvement offered by PALS-μ over the passive and H_∞ controller cases, in terms of time-domain RMS values, is further observed in Figure 3.15 bottom-right. The RMS value of total power consumption in the DC batteries for 'PALS-H_∞' is 0.39 kW, 0.51 kW and 0.30 kW in the M_{min}, M_{nom} and M_{max} cases, respectively. The 'PALS-μ' dissipates similar power in the M_{nom} case as compared to 'PALS-H_∞' and in order to achieve its better performance for the masses away from M_{nom}, the 'PALS-μ' dissipates more power with 0.58 kW and 0.59 kW in the M_{min} and M_{max} cases,

respectively (referring to top-right and bottom-left plots in Figure 3.15).

3.5 Conclusion

The control for ride comfort and road holding performance enhancement of a full car with the SAVGS and the PALS is investigated in this chapter, with uncertainties of the sprung mass and suspension damping taken into account. Linear equivalent models are utilised to design linear robust controllers using H_∞ and μ-synthesis frameworks, which are then simulated with a representative high-fidelity nonlinear full car multi-body model. Selected uncertainties of the suspension damping (representing the damper characteristic nonlinearity) and sprung mass are considered in the μ-synthesis design process for SAVGS and PALS respectively. Essential improvement over the passive suspension system case can be observed with the H_∞ controller, in terms of both ride comfort and road holding at the human comfort frequency range (1-8 Hz). Moreover, the μ-synthesis controller realises significant enhancement over the H_∞ controller performance, especially when the sprung mass deviates away from its nominal value due to variable cargo or passengers. The results demonstrate the effective robustness of the μ-synthesis control framework and its suitability for realistic applications of the SAVGS and the PALS.

Chapter 4

Hybrid Control of Full-Car with PALS Under Variable Payload

4.1 Introduction

In this chapter, a hybrid control with a combination of μ-synthesis and PID, that enhances the control system in chapter 3 has been addressed to demonstrate a more complete control system only in PALS since such hybrid control with H_∞ instead of μ-synthesis has been taken into account in [24] for SAVGS. The existing μ-synthesis control scheme is better than the conventional H_∞ control, for the PALS, in terms of ride comfort and road holding (higher frequency dynamics) with important realistic uncertainties taken into account (see detail in chapter 3). The developed PID control method is applied to guarantee good chassis attitude control capabilities and minimisation of pitch and roll motions (low frequency dynamics). A multi-objective control method, which merges the aforementioned PID and μ-synthesis-based controls is also introduced to achieve simultaneously the low frequency mitigation of attitude motions and high frequency vibration suppression of the vehicle. A high-fidelity SUV full car nonlinear model is used to test the syn-

thesised controller by nonlinear simulations with different ISO-defined road events and variable vehicle payload. The results demonstrate the control scheme's high robustness without sacrificing the suspension performance, given the widely ranged vehicle payload considered in the investigation.

The main contributions of the this chapter are therefore summarised as follows: i) the integration of the proposed μ-synthesis control scheme with a PID scheme addressing the control of low frequency chassis attitude motions, to achieve effective multi-objective blended control for general (low and high frequency) motions under variable payload, and ii) numerical simulations with the adapted nonlinear multi-body model of the PALS-retrofitted full car to assess the effectiveness and efficiency of the proposed control scheme, as compared to the conventional passive suspension and the actively controlled PALS by combined H_∞ PID control that does not explicitly account for uncertainties, while the vehicle undergoes different ISO-defined road events and variable payload.

The chapter is organised as follows: Section 4.2 designs a multi-objective control scheme with the contributions of μ-synthesis and PID controls for the PALS denoted as 'PALS-PID-μ'. Section 4.3 performs numerical simulations to assess the performance of the proposed control schemes by comparing the proposed combined μ-synthesis PID control, 'PALS-PID-μ', and a conventional combined H_∞ PID control denoted as 'PALS-PID-H_∞', with respect to both the high frequency performance improvement as well as the low frequency chassis pitch and roll angle minimisation. Finally, concluding remarks are discussed in Section 4.4

4.2 Control Methodologies Development

In this section, as part of the new scheme, an existing multi-objective PID control scheme ('PALS-PID') for a PALS-retrofitted full car, proposed in [5], is utilised

for the control of chassis attitude motions, particularly aiming at minimisation of both pitch and roll angles. Then, a frequency-dependent multi-objective control scheme ('PALS-PID-μ') with the contributions of both 'PALS-PID' and μ-synthesis based control scheme ('PALS-μ', developed in chapter 3), is introduced to realise simultaneously 0-1 Hz chassis leveling control, 1-8 Hz vibration attenuation control and the control gains mitigation over 10 Hz, thus to control the whole range of frequencies the vehicle operates in.

4.2.1 Multi-objective blended control scheme

A novel multi-objective blended control scheme ('PALS-PID-μ') is introduced to enable both low-frequency chassis attitude control and high frequency vibration mitigation, with the 'PALS-μ' combined seamlessly with the previously proposed (see [5]) multi-objective PID control scheme ('PALS-PID'). The configuration of the proposed 'PALS-PID-μ' control scheme in the PALS-retrofitted full car is shown in the overall Figure 4.1, which provides ride comfort and road holding enhancement during high frequency road manoeuvres, given practical uncertainties, (similarly to 'PALS-μ') and takes effect at the stabilisation of the desired chassis attitude during low frequency manoeuvres (similarly to 'PALS-PID'). It is notable that the PID parameters should be retuned in 'PALS-PID-μ' (listed in Table 4.1) as compared to those in 'PALS-PID' due to the effect of the high frequency μ-synthesis based control. Additionally, conversion functions 'β_i' shown in Figure 2.12 are applied to bridge the linear equivalent model actuation forces ($F_{RCi}^{(H)}$) and the nonlinear multi-body model rocker torques ($T_{RCi}^{(H)}$). Then the inner loop rocker torque tracking control (from T_{RCi^*} to T_{RCi}) links the μ-synthesis-based control and the mechanical system of the PALS full car, where d-q transformation and zero d-axis current control proposed in [40, 5] are utilised such that the three-phase PMSMs behave as DC equivalent motors, with the produced torques proportional solely to the q-axis currents.

4.2.2 Benchmark control schemes

Based on the H_∞ control design in subsection 3.3.1.1, the conventional H_∞ controller, 'PALS-H_∞' is also synthesised (using the diagram in Figure 3.6), which does not take into account uncertainties, for bench-marking purposes. The same weighting functions as those described in Subsection 3.3.2 for the μ-synthesis control are found to also be beneficial and applied to the H_∞ control synthesis.

Moreover, the conventional H_∞ controller is integrated with 'PALS-PID' to provide the blended control 'PALS-PID-H_∞', for further bench-marking purposes with the tuning weights listed in Table 4.1. To perform a comprehensive comparison to the state-of-the-art of 'PALS-PID-H_∞', the μ-synthesis-based controller 'PALS-PID-μ' is defined with the structured uncertainties of sprung mass and suspension damping taken into account and synthesised by means of the MATLAB command `dksyn`.

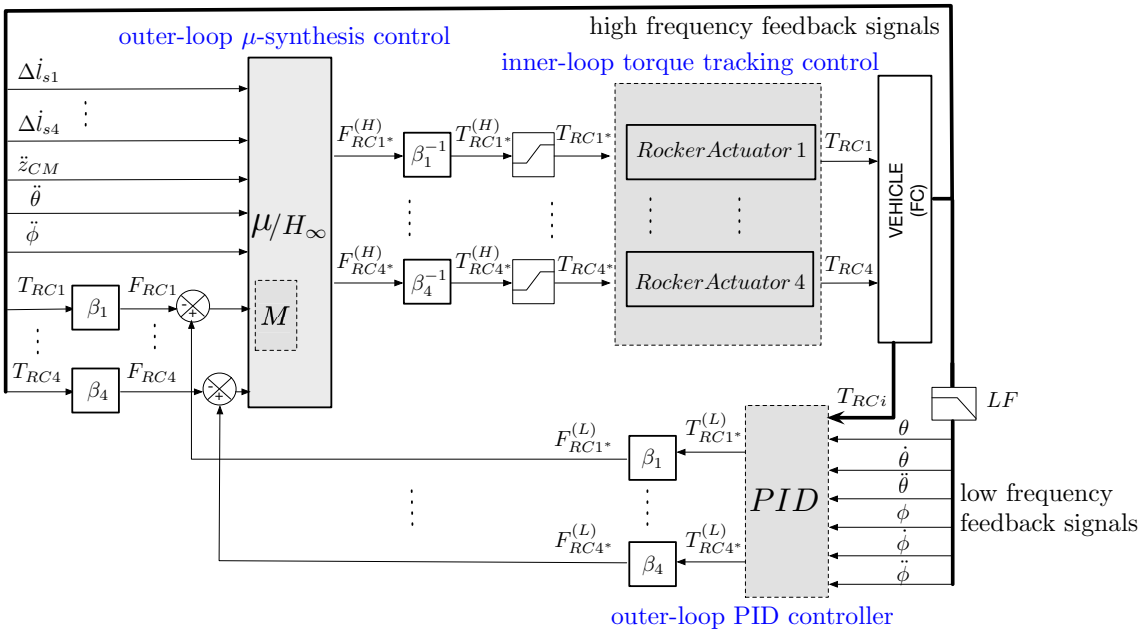


Figure 4.1: Configuration of the multi-objective blended control scheme ('PALS-PID-μ') in the PALS-retrofitted full car.

Table 4.1: PID tuning parameters in 'PALS-PID' 'PALS-PID-H_∞' and 'PALS-PID-μ' control schemes

Controller	Aim	Axle	P	I	D
'PALS-PID'	pitch	F&R	1000	20000	4
	roll	F&R	500	5000	4
'PALS-PID-H_∞'	pitch	F&R	1000	5000	4
	roll	F&R	500	2500	4
'PALS-PID-μ'	pitch	F&R	1000	6000	4
	roll	F&R	2000	2500	4

4.3 Numerical Simulations and analysis

In this section, with the nonlinear multi-body model described in Subsection 2.2.3.2 and PALS μ-synthesis-based control scheme and multi-objective blended control scheme proposed in Subsection 3.3.2 and 4.2.1 respectively, a group of ISO driving manoeuvres, containing, i) random road class C, ii) speed bump, iii) steady-state cornering, iv) step steer and v) brake in a turn, are tested to evaluate the PALS potential in terms of suspension performance and robustness of the synthesised controllers.

Among the above driving manoeuvres, the last three are investigation cases for low frequency chassis leveling, which give rise to the control strategies of 'PALS-PID', 'PALS-PID-H_∞' and 'PALS-PID-μ'. The other two manoeuvres are utilised for the investigation of high frequency vehicle vibration control in terms of ride comfort and road holding improvement, hence a set of control strategies 'PALS-PID-H_∞' and 'PALS-PID-μ', is employed.

The numerical simulations are therefore performed to evaluate the performance comparison: the benefits of combining low frequency signal tracking and high frequency vibration attenuation, given selected uncertainties, with both low frequency and high frequency investigation studies comparison between 'PALS-PID-H_∞' and

'PALS-PID-μ'.

4.3.1 Case Study on steady-state cornering

The open-loop test methods defined in [73] determine how the vehicle behaves in a steady-state circular driving condition. In the nonlinear simulation environment, the PALS-retrofitted full car is driven with a constant forward speed of 100 km/h, with the steering wheel angle increased linearly from 0 to 60 degrees over a time period of 400s.

The variation of the roll angle ϕ against the lateral acceleration a_y is shown in Figure 4.2, where the 'PALS-PID' achieves chassis leveling when cornering with a_y up to approximately 4 m/s^2. The 'PALS-PID-H_∞' and 'PALS-PID-μ' control strategies present the same performance enhancement over the passive suspension as compared to 'PALS-PID', due to the successful tracking of the saturating reference actuation forces, $F_{RCi^*}^{(L)}$, at low frequencies coming from the PID part of both hybrid controls.

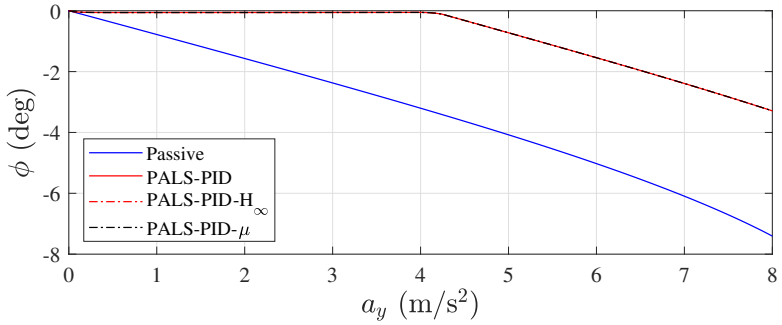


Figure 4.2: Numerical simulation results for the SUV with PALS full car nonlinear model: the chassis roll angle (ϕ) for the $M_{\mathbf{nom}}$ case when the vehicle is undergoing an ISO steady-state cornering at 100 km/h, for different cases of active suspension control.

4.3.2 Case Study on Step Steer

The open-loop test methods defined in [74] investigate the transient response behavior of passenger vehicles. Here, the PALS-retrofitted full car is driven at a constant forward speed of 100 km/h, with the steering wheel angle increasing at a constant rate of 500 deg/s from 0 to 48.6 deg such that the vehicle stabilises at a lateral acceleration of $a_y = 8\,\mathrm{m/s^2}$. The variation of roll angle ϕ and the total power consumption in the DC batteries, $P_{battery}$, is indicated in Figure 4.3, where the 'PALS-PID' provides 42% mitigation of roll angle over the passive suspension, with the peak value of $P_{battery}$ being approximately 2.5 kW. The 'PALS-PID-H_∞' produces slightly less performing results of roll angle RMS value attenuation than 'PALS-PID' with a 1.5 kW $P_{battery}$ peak value and 40% RMS value attenuation of the roll angle as compared to the passive suspension. However, the 'PALS-PID-μ' presents similar roll angle RMS value reduction as compared to 'PALS-PID' (41.87% reduction as compared to passive case) but with lower battery power (2 kW $P_{battery}$ peak value).

4.3.3 Case Study on Brake in a Turn

The open-loop test methods defined in[75] determine how the steady-state circular response of a vehicle is altered by a braking action. Here, the PALS-retrofitted full car is initially driven in a circular path of 100 m radius at a constant lateral acceleration of $5\,\mathrm{m/s^2}$, corresponding to a constant forward speed of 80 km/h, then the steering wheel is fixed and brakes applied to enable the vehicle to slow down at a constant deceleration of $a_x = \text{-}5\,\mathrm{m/s^2}$.

The variations of the roll angle, ϕ, and pitch angle, θ, are shown in Figure 4.4. It can be seen that as compared to the passive suspension, the 'PALS-PID' has less overshoot but it takes a longer time to stabilise in terms of roll angle performance,

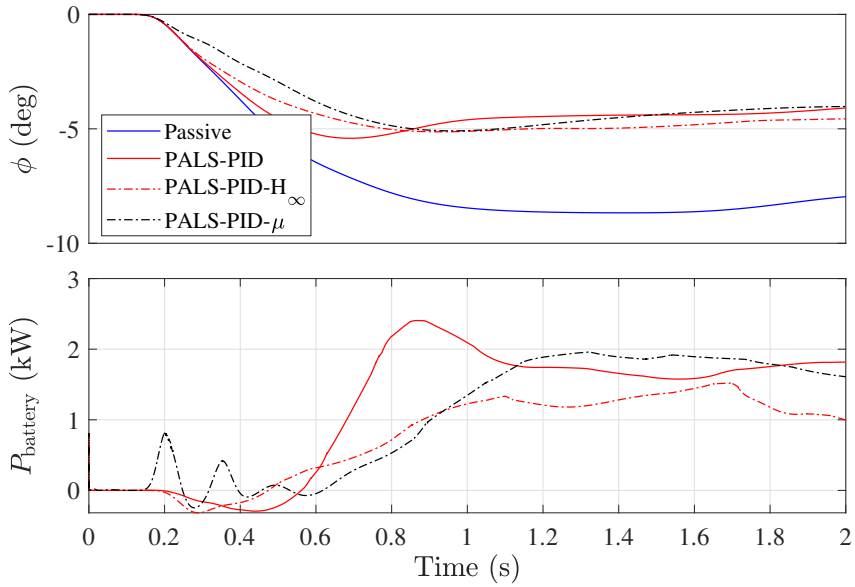


Figure 4.3: Numerical simulation results for the SUV with PALS full car nonlinear model: the chassis roll angle (ϕ) and total power consumption in the DC batteries ($P_{battery}$) for the M_{nom} case when the vehicle is undergoing an ISO step steer at 100 km/h, for different cases of active suspension control.

and its average pitch angle is reduced from -1.5 ° to -0.4 ° with a larger overshoot at approximately 5 s before it comes to a stop. 'PALS-PID-H_∞' has a similar performance to that of 'PALS-PID' for the whole time except for marginally larger pitch and smaller roll angle overshoots in the time period of 1 s-2 s. 'PALS-PID-μ' provides pitch angle response close to that of 'PALS-PID' and 'PALS-PID-H_∞', which indicates the improvement over the passive suspension. In terms of roll angle performance, 'PALS-PID-μ' shows a similar response from 1 s to 3.5 s as compared to the other two active cases, while after 3.5 s, it follows the passive suspension response ending at 5 s which is faster than the other two active cases in that time period.

4.3.4 Case Study on high-frequency driving manoeuvres

The two multi-objective blended control strategies 'PALS-PID-H_∞' and 'PALS-PID-μ' are tried while following the previously defined high frequency driving manoeuvres (speed bump and random road Class C) and compared to 'PALS-H_∞' and

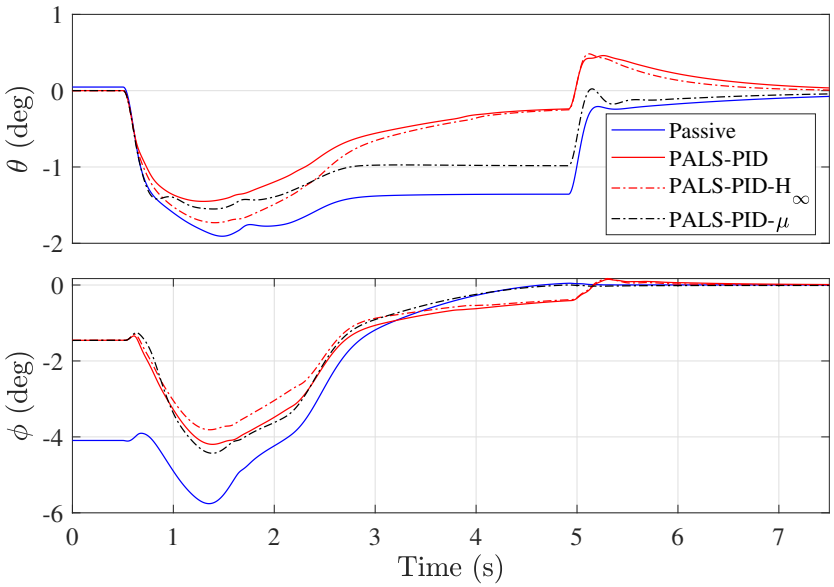


Figure 4.4: Numerical simulation results: the chassis pitch angle (θ) and chassis roll angle (ϕ) for the M_{nom} case when the vehicle is undergoing an ISO brake in turn at initial longitudinal speed 80 km/h, for different cases of active suspension control.

'PALS-μ' for the same manoeuvres to demonstrate the effectiveness and efficiency of the proposed 'PALS-PID-μ' control.

Numerical simulation results of the speed bump case for the nominal sprung mass case, M_{nom}, are shown in Figure 4.5, where 'PALS-H_∞' and 'PALS-μ' achieve the best performance in terms of ride comfort and road holding (as seen by the vertical and pitch acceleration, and tire deflection responses) as compared to the passive case, with their performance and power consumption being very similar. Due to the compromise of the high frequency performance because of the influence of the PID control part in 'PALS-PID-H_∞', it performs worse than 'PALS-H_∞' especially for the pitch acceleration, while also consuming less power than 'PALS-H_∞'. In contrast, 'PALS-PID-μ' offers nearly the same significant improvement in terms of ride comfort and road holding with slightly less power consumption as compared to 'PALS-μ', as shown in the $P_{battery}$ plot of Figure 4.5, which indicates that the compromise in the performance of 'PALS-PID-μ' at higher frequencies due to its

low frequency-intended PID control aspect, is much less than the corresponding compromise for 'PALS-PID-H_∞'.

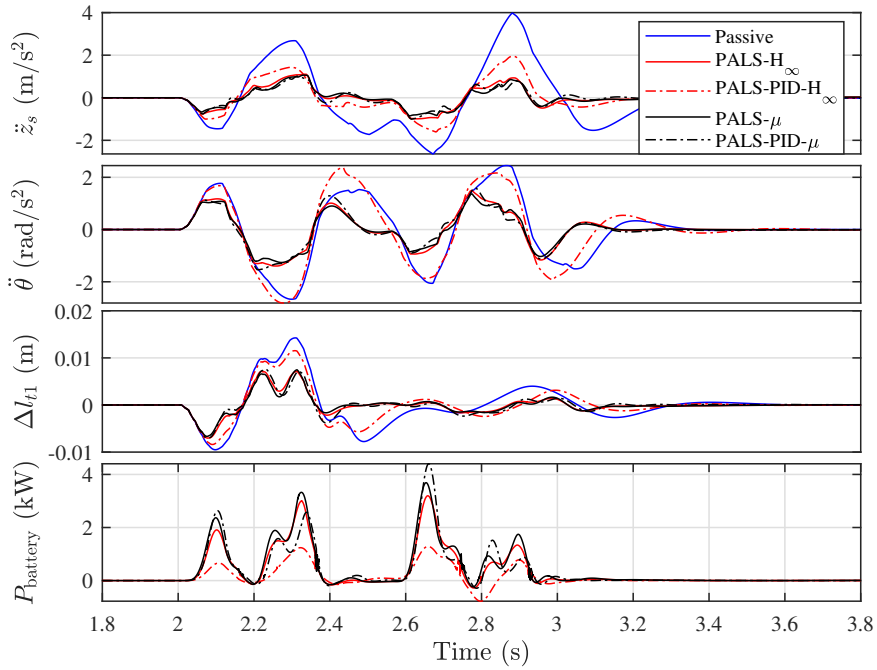


Figure 4.5: Numerical simulation results: the time-domain value of CMC vertical acceleration ($\ddot{z}_s$), pitch acceleration ($\ddot{\theta}$), tire deflection Δl_{t1} and power consumption in the DC batteries ($P_{battery}$) for the M_{nom} case when the vehicle is driven over an ISO speed bump at 20 km/h, for different cases of suspension control.

Similar conclusions can be drawn from Figure 4.6 of the PSD plot in road Class C manoeuvre, where again 'PALS-H_∞' and 'PALS-μ' achieve the best performance in terms of ride comfort and road holding (reduction of PSD gains for all variables in Figure 4.6 in the frequency range of interest), with the 'PALS-μ' having an edge as compared to 'PALS-H_∞' in some of the metrics in Figure 4.6 and therefore being the ultimate best case. Also similarly, 'PALS-PID-H_∞' produces less ride comfort and road holding improvement than 'PALS-H_∞' as compared to the passive case. On the other hand, 'PALS-PID-μ' still provides similar ride comfort and road holding performance as compared to 'PALS-μ', which indicates the significant improvement over 'PALS-PID-H_∞'. The total power consumption in the batteries for the M_{nom}

case with different active suspension controllers is shown in Figure 4.7, where it can be seen that the μ-synthesis controllers consume more power than the H_∞ controllers in order to provide the edge in the performance illustrated in Figure 4.6 over the H_∞ controllers. It is also clear that the power consumption of 'PALS-PID-μ' is similar to that of 'PALS-μ', further indicating their similar behavior at high frequencies.

Figure 4.8 further illustrates the average value of $P_{battery}$ for M_s swept from $M_{\min}$ to $M_{\max}$. It is clear that 'PALS-PID-μ' consumes slightly less power as compared to 'PALS-μ', which is also consistent with providing slightly less control performance, as seen, for example, in Figure 4.6. These two μ-synthesis controllers provide in a similar manner performance improvement (see Figure 4.9) and power consumption change (see Figure 4.8) with varied sprung mass, while the 'PALS-H_∞', which is overall somewhat less power consuming that both the μ-synthesis controllers, becomes even less power consuming (and consistently less performing) as M_s is increased or decreased away from M_{nom}.

The performance improvements alluded to above are demonstrated in Figure 4.9 in terms of body accelerations and tire deflection RMS values as percentage improvements over the passive case, for different cases of sprung mass. It can be clearly seen that even in the nominal sprung mass case 'PALS-μ' universally outperforms 'PALS-H_∞', marginally in most cases but significantly in roll acceleration, while in the case of the multi-objective schemes, 'PALS-PID-μ' performs significantly better than 'PALS-PID-H_∞' in all metrics. It is therefore clear that the performance deterioration suffered by combining the low and high frequency objectives is much less in 'PALS-PID-μ' with respect to 'PALS-μ', as compared to 'PALS-PID-H_∞' with respect to 'PALS-H_∞'. This can be attributed to the robustness of the μ-synthesis approach to a more realistic class of perturbations in comparison to the H_∞ control methodology. The benefits of μ-synthesis over H_∞ control approaches when the sprung mass is different from the nominal one are even higher as compared to the

nominal sprung mass case and are clearly demonstrated in the middle and bottom plots of Figure 4.9.

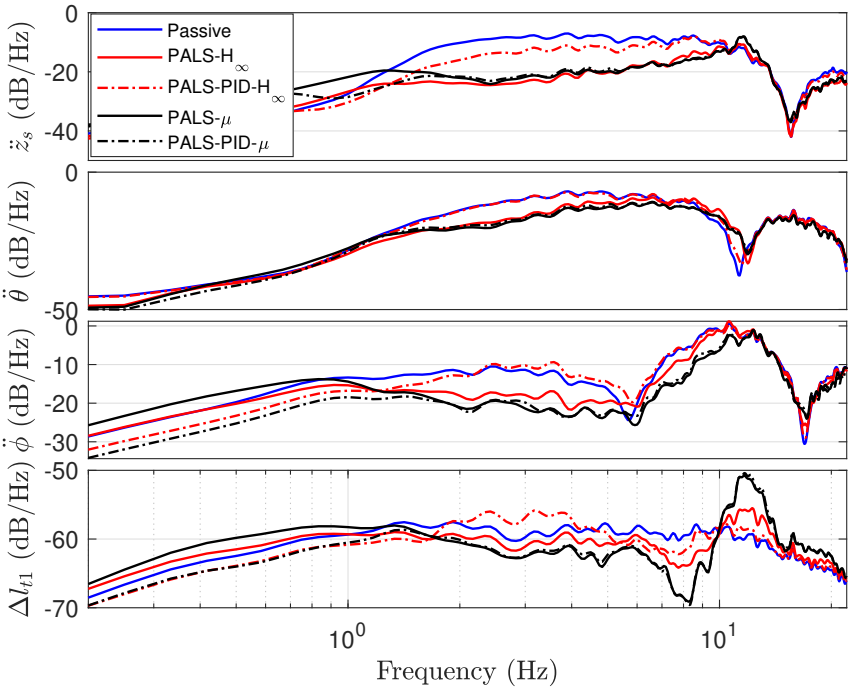


Figure 4.6: Numerical simulation results: the PSDs of CMC vertical acceleration ($\ddot{z}_s$), pitch acceleration ($\ddot{\theta}$), roll acceleration ($\ddot{\phi}$) and tire deflection Δl_{t1} for the M_{nom} case when the vehicle is driven over an ISO random road Class C at 100 km/h, for different cases of suspension control.

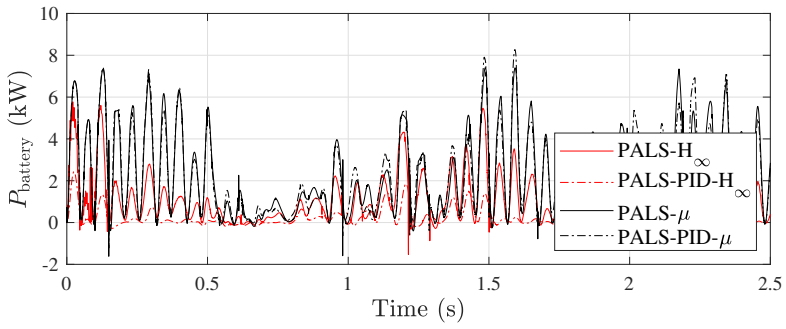


Figure 4.7: Numerical simulation results: the total power consumption in the DC batteries ($P_{battery}$) in a 2.5 s time history for the M_{nom} case when the vehicle is driven over an ISO random road Class C at 100 km/h, for different cases of active suspension control.

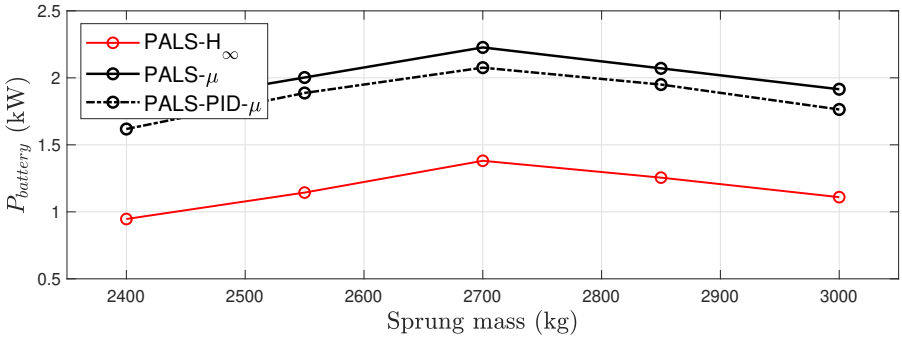


Figure 4.8: The average value variation of total power consumption in the DC batteries when the vehicle is driven over an ISO random road Class C at 100 km/h and M_s is swept from $M_{\min}$ to $M_{\max}$ in 150 kg increments, for the cases of 'PALS-H_∞','PALS-μ' and 'PALS-PID-μ' controllers.

4.4 Conclusions

The recently proposed mechatronic suspension of the Parallel Active Link Suspension (PALS) is investigated in the application to a SUV full car, with sprung mass and suspension damping uncertainties taken into consideration in the suspension control design, revealing promising potential for both low frequency chassis leveling and high frequency ride comfort and road holding improvement under variable payload.

The proposed multi-objective PID and μ-synthesis control schemes are further merged to enable all functions of the PALS in practice, given selected uncertainties. As compared to the conventional hybrid control of multi-objective PID and H_∞ control for nominal payload, the combined multi-objective PID μ-synthesis control preserves the high frequency ride comfort and road holding improvement, without deteriorating the low frequency chassis leveling performance. In addition, when the payload is varied, the proposed multi-objective PID μ-synthesis control significantly outperforms the conventional hybrid control scheme, especially at high frequencies. In terms of a comparison between the two proposed schemes of μ-synthesis control and the multi-objective PID μ-synthesis control, the latter is offering a sim-

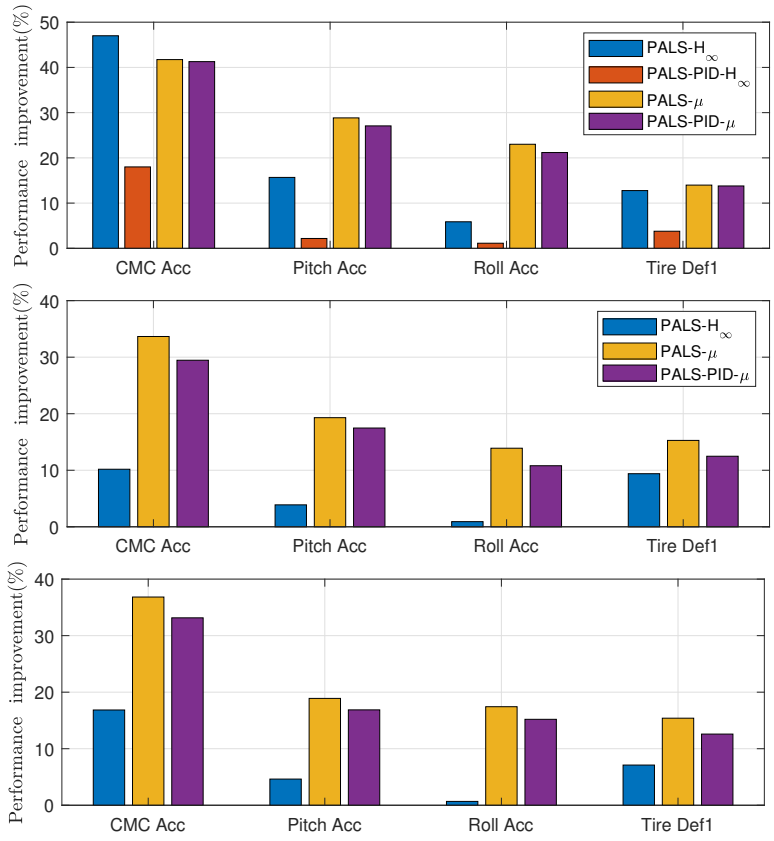


Figure 4.9: Numerical simulation results: the RMS value performance improvement of CMC vertical acceleration ($\ddot{z}_s$), pitch acceleration ($\ddot{\theta}$), roll acceleration ($\ddot{\phi}$) and tire deflection (Δl_{t1}), as a percentage of the passive case performance, in the sprung mass, M_s, cases of $M_{\mathbf{nom}}$ (top), $M_{\mathbf{min}}$ (middle), and $M_{\mathbf{max}}$ (bottom) when the vehicle is driven over an ISO random road Class C at 100 km/h, for different cases of suspension control. The precise calculation of the height of the bars is $\frac{\mathbf{metric_{passive}} - \mathbf{metric_{active}}}{\mathbf{metric_{passive}}}$, where 'metric' is the RMS value of one of $\ddot{z}_s$, θ, ϕ, and Δl_{t1}, and 'active' is one of the active suspension controller cases.

ilar performance as the former in almost all cases of driving manoeuvres (at high frequencies), while at the same time, it can also effectively control low frequency dynamics that μ-synthesis control does not cover. Numerical simulations of various ISO manoeuvres, such as steady-state cornering, step steer, brake in turn, speed bump and random road C with a high fidelity model of the vehicle with PALS, have been provided to illustrate the effectiveness of the proposed methods.

Chapter 5

Feedforward PID Control of Full-Car with PALS for Improved Chassis Attitude stabilisation

5.1 Introduction

This chapter proposes a feedforward control strategy to combine with a previously developed PID control scheme [5] in the recently introduced Parallel Active Link Suspension (PALS), to address the problem of the feedback delays in chassis attitude stabilisation. The contributions of the chapter are threefold: i) development of two compensation models based on full car steady state analysis and nonlinear simulation fitting, respectively, and selection of the best performing compensation model by comparison of their fitting accuracy, ii) design of 'feedforward-PID' control that combines the nonlinear simulation fit based compensation model developed above with regular PID control, iii) numerical simulations with a nonlinear multibody model of the PALS-retrofitted SUV full car to assess the effectiveness and robustness of the proposed control scheme, as compared to the passive suspension

and the actively controlled PALS by conventional robust control, while the vehicle undergoes different ISO-defined road events.

The rest of the chapter is organised as follows: Section 5.2 illustrates the derivation of the feedforward normal load compensation with polynomial fitting method applied in the nonlinear simulation environment, and with steady state analysis of the full car. Section 5.3 introduces a feedforward PID control scheme based on nonlinear simulation fit based compensation model. Section 5.4 performs numerical simulations to assess the performance of the proposed control scheme by comparing the proposed feedforward-PID scheme with conventional PID control in terms of pitch and roll angle minimisation. Finally, concluding remarks are discussed in Section 5.5.

5.2 Development of tire force compensation model

In this subsection, the mathematical steady-state model of the PALS-retrofitted full car described in section 2.2.5 is used to motivate the proposal of one of the feedforward compensation models. The major parameters are given previously in Table 2.3. The other feedforward compensation model is introduced based on the relationship obtained by applying polynomial fitting through simulation of nonlinear full car model.

For the feedback control system, the controller does not work well until the deviation of the roll angle reaches an ultimate value. However, it is hard to regulate the system when the roll angle deviation is large or the roll rate is increasing which may result in rollover. Therefore, the vehicle's longitudinal and lateral acceleration are estimated according to the steering wheel angle, longitudinal speed, gas pedal and brake pedal position. Then, the active suspension produces the vertical tire force in advance to ensure that both roll and pitch angle are minimised.

5.2.1 Nonlinear simulation fit based compensation model

In addition to the steady state model described in section 2.2.5, a new practical approach is introduced in this subsection which uses a polynomial fitting method in the nonlinear simulation of a high fidelity nonlinear multi-body model developed in [5] to establish the relationship between longitudinal acceleration (a_x), lateral acceleration (a_y) and the vertical tire force increments (ΔF_{tzi}) at each corner. The approach is detailed as follows: i) the steady state cornering manoeuvre is selected to find the relationship between ΔF_{tzi} and a_y only, due to the linear growth of a_y with constant v_x; ii) similarly, with initial longitudinal speed $v_x = 100\,\text{km/h}$, the straight line constant deceleration manoeuvre is applied to establish the relationship between ΔF_{tzi} and a_x. The plots of the aforementioned ΔF_{tzi} with regards to a_y and a_x are shown in Figs. 5.1 and 5.2, respectively.

To achieve the best fitting, $\Delta F_{tzi}^{(a_y)}$ is selected as a third order polynomial fitting and $\Delta F_{tzi}^{(a_x)}$ is chosen as first order polynomial fitting. Hence, the total vertical tire force increment of the selected compensation model is derived as follows:

$$\Delta F_{tzi} = \Delta F_{tzi}^{(a_x)} + \Delta F_{tzi}^{(a_y)}. \tag{5.1}$$

The comparison of vertical tire force increments ΔF_{tzi} between the steady state model and the nonlinear simulation fit model in terms of steady state cornering and brake in turn ISO manoeuvres are shown below in Figure 5.3 and Figure 5.4. As it can be seen in these two plots, although the steady state model provides the information on ΔF_{tzi}, the nonlinear simulation fit model offers more accurate results for ΔF_{tzi}. Therefore, the nonlinear simulation fit model is selected as the ΔF_{tzi} compensation model.

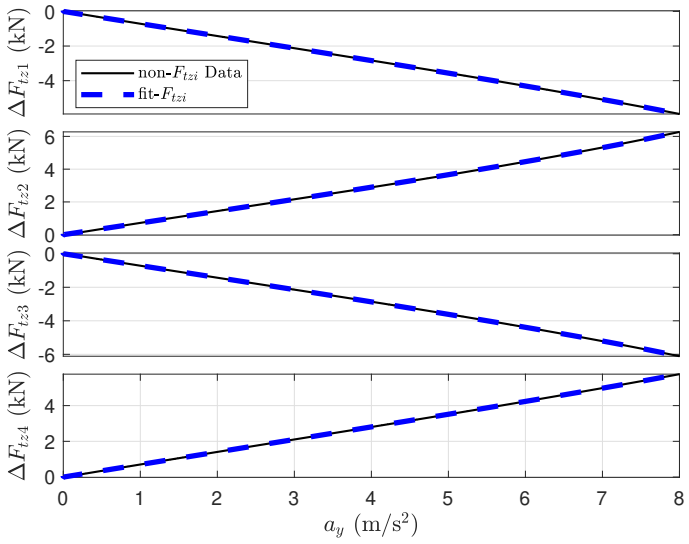


Figure 5.1: Vertical tire force increment (ΔF_{tzi}) polynomial fitting with respect to the lateral acceleration (a_y) in the steady state cornering manoeuvre, where the black solid line corresponds to the nonlinear simulation ΔF_{tzi} data and the blue dashed line to the third order polynomial fitting line.

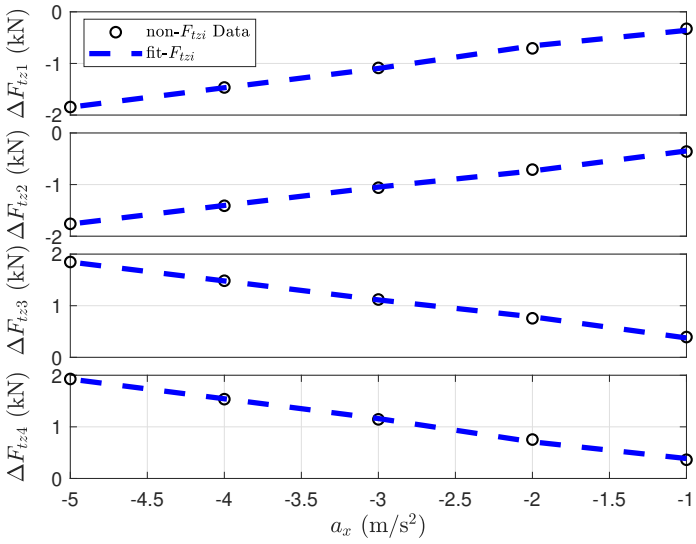


Figure 5.2: Vertical tire force increment (ΔF_{tzi}) linear fitting with respect to the longitudinal acceleration (a_x) in the constant deceleration manoeuvre, where the black circles correspond to the nonlinear simulation ΔF_{tzi} data and the blue dashed line to the first order polynomial fitting line

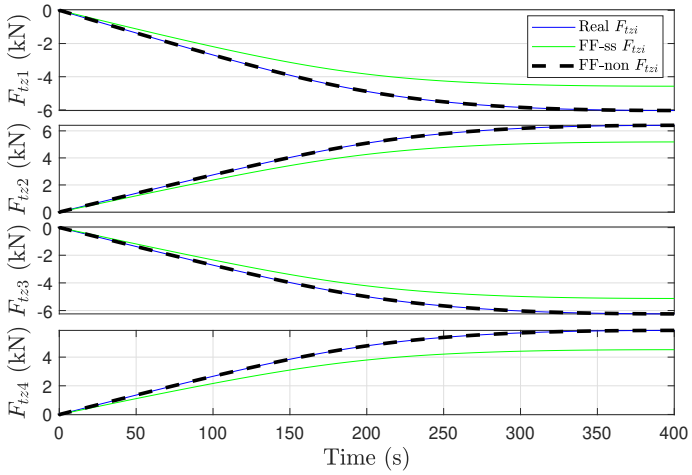


Figure 5.3: Vertical tire force increment (F_{tzi}) in the ISO steady-state cornering manoeuvre as compared to initial state (100 km/h straight line driving manoeuvre) versus time: the blue line depicts the case without using compensation model, the green line depicts the case with steady state compensation model and the black dashed line depicts the case with nonlinear simulation fit model.

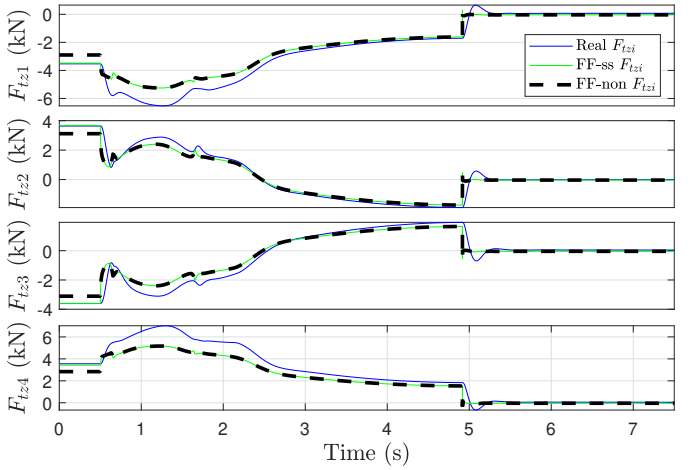


Figure 5.4: Vertical tire force increment (F_{tzi}) in the ISO brake in turn manoeuvre as compared to initial state (80 km/h straight line driving manoeuvre) versus time: the blue line depicts the case without using compensation model, the green line depicts the case with steady state compensation model and the black dashed line depicts the case with nonlinear simulation fit model.

5.3 Control Methodology Development

This subsection describes the synthesis of the two control schemes with PALS for the chassis leveling: A) the previously proposed multi-objective PID control [5],

and B) the newly proposed feedforward PID control based on nonlinear simulation fit, which is detailed in sec. 5.2.1.

5.3.1 PID control ('PALS-PID')

To achieve desirable chassis attitude and driving dynamics, the multi-objective PID control scheme ('PALS-PID') is adapted to the PALS-retrofitted full car [5]. As it can be seen in Figure 5.5, a group of PID controllers at each corner i, are synthesised to deal with pitch and roll angle control, with θ_i and ϕ_i denoting feedback signals. The reference rocker torque T_{RCi^*} with pitch angle minimisation, at each corner is obtained as follows:

$$\begin{aligned} T^{(1)}_{RC1^*} &= T^{(1)}_{RC2^*} = -K^{(1)}_{p,f}\theta - K^{(1)}_{i,f}\int\theta - K^{(1)}_{d,f}\dot{\theta}, \\ T^{(1)}_{RC3^*} &= T^{(1)}_{RC4^*} = K^{(1)}_{p,r}\theta + K^{(1)}_{i,r}\int\theta + K^{(1)}_{d,r}\dot{\theta}, \end{aligned} \tag{5.2}$$

and the reference rocker torque with roll angle minimisation is:

$$\begin{aligned} T^{(2)}_{RC1^*} &= -T^{(2)}_{RC2^*} = -K^{(2)}_{p,f}\phi - K^{(1)}_{i,f}\int\phi - K^{(2)}_{d,f}\dot{\phi}, \\ T^{(2)}_{RC3^*} &= -T^{(2)}_{RC4^*} = -K^{(2)}_{p,r}\dot{\phi} - K^{(2)}_{i,r}\int\phi - K^{(2)}_{d,r}\dot{\phi}, \end{aligned} \tag{5.3}$$

with the PID tuning parameters detailed in Table 5.1. The overall reference rocker torque feeding the rotary rocker actuator at each corner is:

$$T_{RCi^*} = T^{(1)}_{RCi^*} + T^{(2)}_{RCi^*}. \tag{5.4}$$

Through the inner-loop tracking control at each corner, the T_{RCi^*} is transformed to T_{RCi} and then fed to the vehicle system which is detailed in [5].

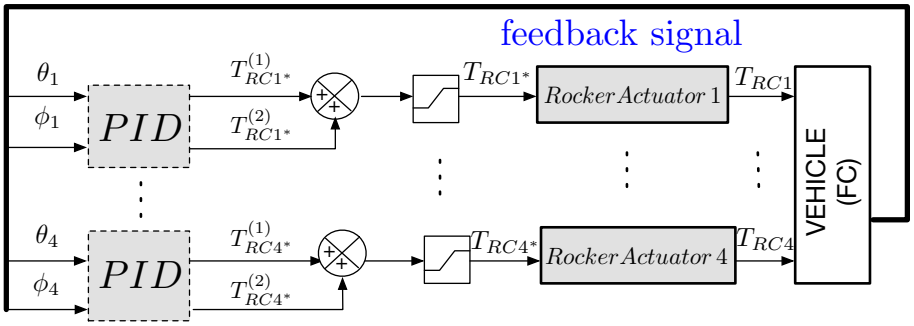


Figure 5.5: Multi-objective PID control implementation in the PALS-retrofitted full car. [5, 21]

5.3.2 Nonlinear Feedforward PID ('FF-PID-non')

The previous multi-objective PID control loop regulates the output pitch and roll angle of the vehicle plant employing negative feedback. On the other hand, as shown in Figure 5.6, with both longitudinal and lateral acceleration measured from the vehicle, the nonlinear Feedforward PID control approach utilises the feedforward compensation model, proposed in subsection 5.2.1.A, to calculate the vertical tire force F_{tz_i}. Through the conversion block β_i in (2.18), the $T^{(FF)}_{RC_i}$ are obtained to achieve major compensation of the actuation torques of the rotary actuators. Usually, the feedforward control cannot directly compensate the full information of the output rocker torque T_{RCi} and therefore requires combining with the PID feedback control loops. Then the inner loop rocker torque tracking control links the feedforward control and the mechanical system of the PALS full car, where d-q transformation and zero d-axis current controls proposed in [5] are utilised, such that the three-phase PMSMs behave as DC equivalent motors, with the produced torques proportional solely to the q-axis currents.

It is notable that the PID parameters should be retuned in nonlinear feedforward PID control (listed in Table 5.1) as compared to those in 'PALS-PID' control due to the effect of the feedforward control. However, this tuning for PID is time-efficient

since feedforward control accounts for nearly 90% of the total T_{RC_i}, making the PID

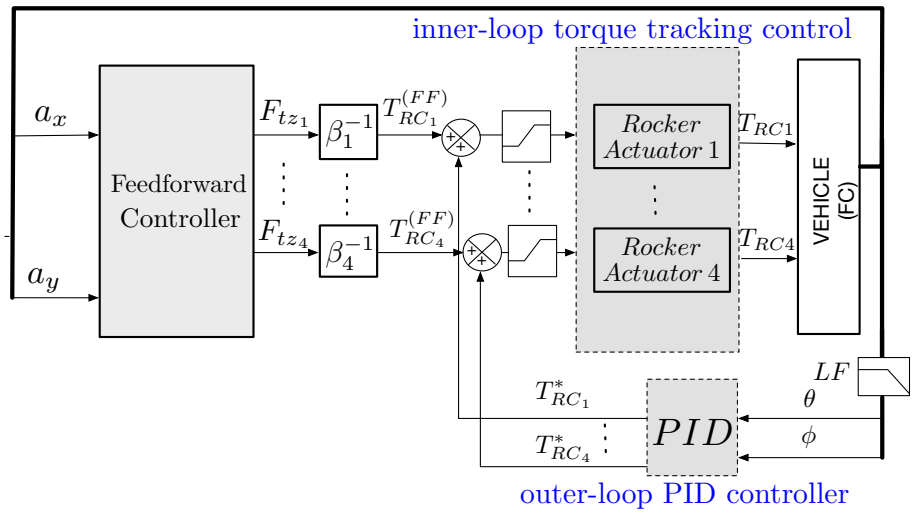


Figure 5.6: 'FF-PID-non' control implementation in the PALS-retrofitted full car with PID block defined in Figure 5.5.

Table 5.1: PID tuning parameters in 'PALS-PID' and 'FF-PID-non' control schemes

Controller	Aim	Axle	P	I	D
'PALS-PID'	pitch	F&R	1000	20000	4
	roll	F&R	500	5000	4
'FF-PID-non'	pitch	F&R	100	2500	2
	roll	F&R	50	1500	2

5.4 Numerical Simulations with nonlinear multi-body model and analysis

In this subsection, with the nonlinear multi-body model described in previous subsection 2.2.3.2 and the control strategies proposed in subsection 5.3, a group of ISO driving manoeuvres, containing, A) step steer, B) steady-state cornering, C) brake in a turn, D) pure longitudinal braking and acceleration, E) fishhook, and

F) continuous sinusoid steer, manoeuvres are tested to evaluate the efficiency and robustness of the synthesised controllers ('PALS-PID' synthesised in subsection 5.3.1 and 'FF-PID-non' synthesised in subsection 5.3.2).

5.4.1 Step Steer

ISO 7401:2011 details an open-loop test method to determine the transient response behavior of passenger vehicles [74]. Here, the PALS-retrofitted full car is driven at a constant forward speed of 100 km/h, with the steering wheel angle increasing at a constant rate of 500 deg/s from 0 ° to 48.6 ° (from 0.1 s to 0.197 s) such that the vehicle stabilises at a lateral acceleration of $a_y = 8\,\mathrm{m/s^2}$. The reduction in roll angle ϕ achieved thanks to the synthesised controllers is presented in Figure 5.7, where 'PALS-PID' provides 42% mitigation of roll angle RMS value over the passive suspension. The 'FF-PID-non' produces even better performance in terms of roll angle RMS value attenuation than 'PALS-PID', with 52% mitigation of roll angle over the passive suspension. Furthermore, it does not suffer as the 'PALS-PID' does from a positive roll angle slope at approximately 0.7 s, and as Figure 5.7 shows, the response of 'FF-PID-non' is much faster than that of 'PALS-PID' in terms of front-left corner rocker torque T_{RC_1}.

5.4.2 Steady State Cornering

ISO 4138:2004 defines an open-loop test method to assess the potential of the passenger vehicles for roll mitigation in steady-state circular driving [73].

The vehicle is driven at a constant longitudinal speed of 100 km/h, with the angle of the steering wheel linearly increased from 0 ° to 60 ° in 400 s. Figure 5.8 depicts that the roll angle is completely neutralised up to lateral accelerations of approximately $4\,\mathrm{m/s^2}$ for 'PALS-PID'. The 'FF-PID-non' control strategy presents

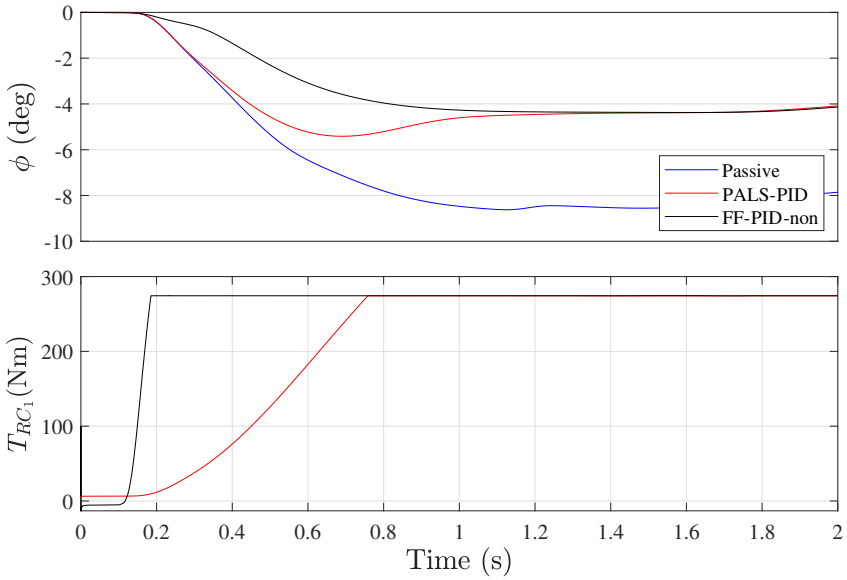


Figure 5.7: Numerical simulation results for the SUV with PALS full car: the chassis roll angle (ϕ) and front left corner rocker torque (T_{RC_1}) when the vehicle is undergoing an ISO step steer at 100 km/h, for different methods of suspension control.

the same performance enhancement over the passive suspension as 'PALS-PID', due to the feedforward compensation of the saturating actuation forces.

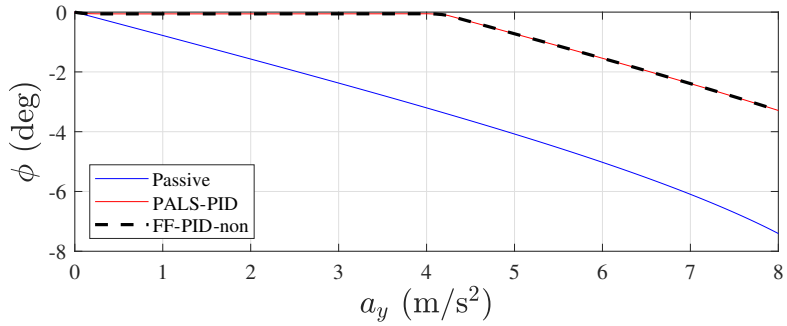


Figure 5.8: Numerical simulation results for the SUV with PALS full car: the chassis roll angle (ϕ) when the vehicle is undergoing an ISO steady-state cornering, for different cases of active suspension control.

5.4.3 Brake in a turn

ISO 7975:2006 presents an open-loop test method for determining the steady-state circular response of a vehicle that is altered by a sudden braking. As defined in [75], the PALS-retrofitted full car is initially driven in a circular path of 100 m radius at a constant lateral acceleration of 5 m/s^2, corresponding to a constant forward speed of 80 km/h, then the steering wheel is fixed and brakes applied to enable the vehicle to slow down at a constant deceleration of a_x =-5 m/s^2.

The variations of the roll angle, ϕ, and pitch angle, θ, are shown in Figure 5.9. It can be seen that, as compared to the passive suspension, the 'PALS-PID' has less overshoot but it takes a longer time to settle in terms of roll angle performance, and its average pitch angle is reduced from -1.5 ° to -0.4 ° with a larger overshoot at approximately 5 s before it comes to a stop. 'FF-PID-non' has a similar performance to that of 'PALS-PID' with slightly smaller overshoot over an initial time period of 0-2 s in terms of pitch angle performance, but then it converges much faster to zero without suffering as the 'PALS-PID' does from a positive pitch angle spike at approximately 5 s when the car comes to a stop and restores its equilibrium position, Furthermore, its roll angle is reduced with a much smaller overshoot at approximately 1.5 s and shorter time to settle as compared to 'PALS-PID'. Figure 5.9 also shows the plots of the rocker torque of front left corner (T_{RC_1}) and rear left corner (T_{RC_3}). As it can be seen, the response of 'FF-PID-non' is much faster than that of 'PALS-PID' in terms of stopping the vehicle.

5.4.4 Pure longitudinal acceleration and braking

The pure longitudinal accelerating and braking manoeuvre is used to assess the ability of the controlled system for pitch mitigation. In this manoeuvre, a hard acceleration process starts from 1 km/h to 100 km/h in 6.5 s, which is then followed

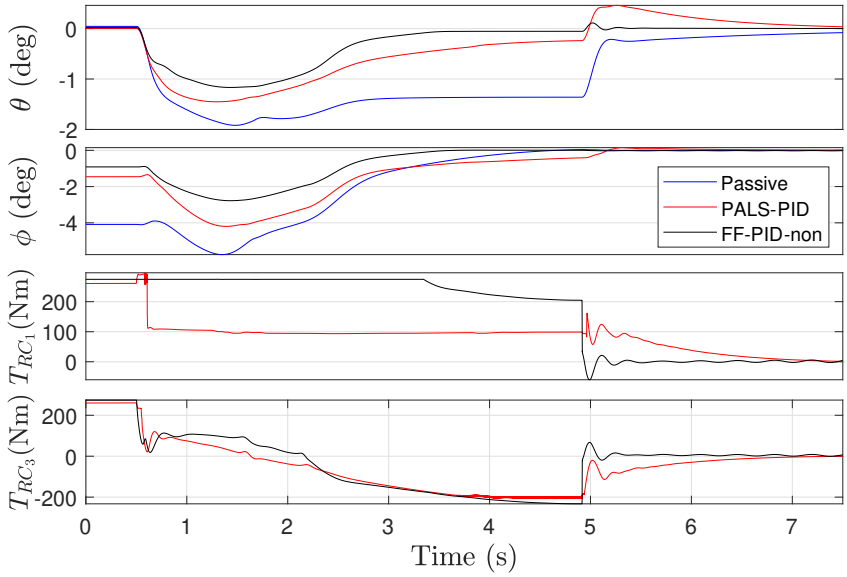


Figure 5.9: Numerical simulation results: the chassis pitch angle (θ), chassis roll angle (ϕ), rocker torque of front left corner (T_{RC_1}) and rear left corner (T_{RC_3}) when the vehicle is undergoing an ISO brake in turn at initial longitudinal speed 80 km/h, for different methods of suspension control.

by a 2 s constant speed period and an emergency stop. Time responses for the PALS full car in this manoeuvre are shown in Figure 5.10. In the top row, the reference and actual speed profiles are compared. As it can be seen, the car follows the acceleration profile closely, and the resulting deceleration rates remain within the 1.05 g to 1.25 g band during the emergency stop. Pitch angle simulation results for different controllers are displayed in the bottom row of Figure 5.10, which shows that the 'PALS-PID' is capable of maintaining an overall flat pitch angle during the acceleration phase and achieves approximately 35% pitch angle correction during the emergency stop. The 'FF-PID-non' outperforms the 'PALS-PID' and achieves almost $\frac{1}{3}$ of the average pitch angle during the acceleration phase and marginally better response during emergency stop as compared to 'PALS-PID'.

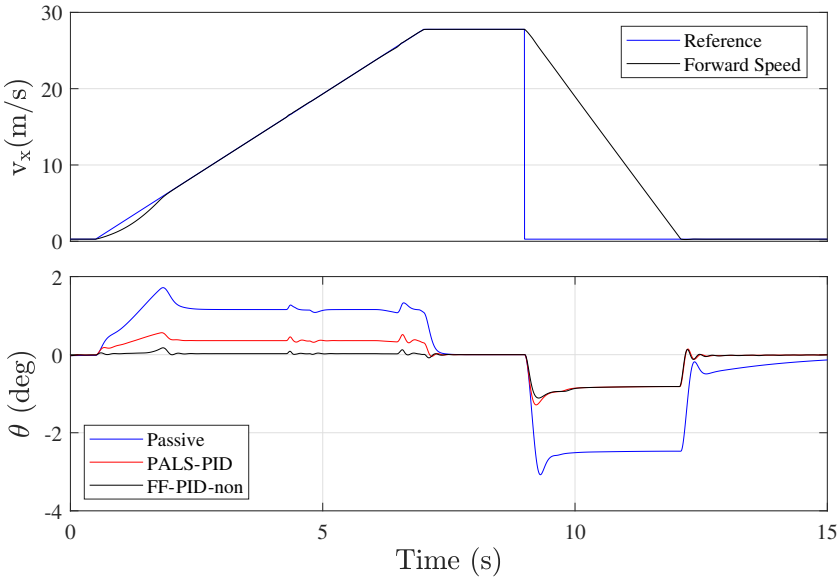


Figure 5.10: Numerical simulation results: the forward speed (v_x) and the chassis pitch angle (θ) when the vehicle is undergoing an ISO longitudinal acceleration/deceleration manoeuvre for different methods of suspension control.

5.4.5 Fishhook

The fishhook defines an open-loop test procedure to evaluate the vehicle dynamic rollover propensity [76].

The test procedure consists of two stages. In the first one, the PALS-retrofitted full car is driven at a forward speed of 50 miles per hour (mph), while a slow turning manoeuvre is performed to determine the steering wheel angle δ_{ini} required to reach a lateral acceleration of 0.3 g. In the second stage, the vehicle is driven in a straight line at a certain manoeuvre Entrance Speed (MES). Then, the throttle pedal is released, and the steering-wheel angle is rotated up to $\delta_{fh} = 6.5\,\delta_{ini}$. The steering wheel angle is reversed to - δ_{fh} when the roll rate reduces below 1.5 deg/s, staying there for 3 s, after which it reverts to zero over a time period of 2 s. The first manoeuvre is performed with MES=35 mph, then it is repeated with MES=40, 45 and 50 mph.

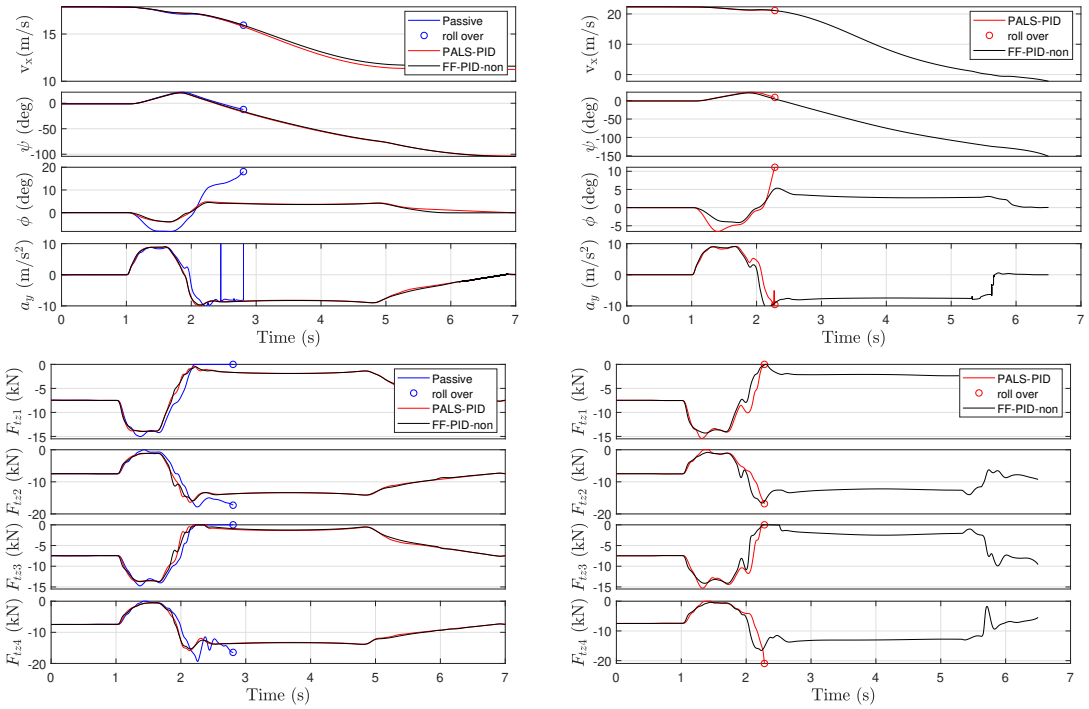


Figure 5.11: Numerical simulation results: the forward speed (v_x), chassis yaw angle (ψ), roll angle (ϕ) and lateral acceleration (a_y) with MES=40 mph (top-left), and MES=50 mph (top-right); and the vertical tire force (F_{tzi}) with with MES=40 mph (bottom-left), and MES=50 mph (bottom-right) when the vehicle performs fishhook manoeuvres for different methods of suspension control.

The passive car survives the fishhook with MES = 35mph, but suffers from rollover at MES = 40mph. The PALS-retrofitted full car with 'PALS-PID' control manages to avoid rollover at MES = 40mph and MES = 45mph, while it cannot maintain the roll angle stability at MES = 50mph. In contrast, the feedforward control strategy 'PALS-PID-non' is capable of presenting robust and stable performance for all four test values of MES.

Results for MES = 40mph are presented in the first column of Figure 5.11 for the passive and active configurations. In the top-left plot of Figure 5.11, both active controllers keep the roll angle below 5 deg in the first steering phase, and the roll angle peaks at around 5 deg in the second. The forward speed, yaw angle and lateral acceleration are also included in the plots to help understand the overall performance. The results of vertical tire force at each corner with different controllers

are shown in the bottom-left plot of Figure 5.11. The passive suspension displays two-wheel lift at the point indicated by blue circles, and eventually rolls over. The other two active controllers also display two-wheel lift at t = 2.23 s, but regain contact with the ground quickly at t = 2.29 s and remain stable throughout the manoeuvre.

Results for MES = 50mph are shown in the second column of Figure 5.12 for active configurations only. The chassis parameters including forward speed, yaw angle, roll angle and lateral acceleration are displayed in the top-right plot of Figure 5.11. It is clear that 'PALS-PID-non' keeps the roll angle below 5 deg throughout the manoeuvre. Two-wheel lift occurs at time t = 2.26s, but contact with the ground is reclaimed at time t = 2.38s and the vehicle remains stable until the end of the manoeuvre which can be verified in the bottom-right plot of Figure 5.11. However, 'PALS-PID' displays two-wheel lift at t = 2.28s and finally rolls over.

5.4.6 Continuous sinusoid steer

The continuous sinusoid steer defines an open-loop test procedure to understand the performance of the PALS at various frequencies. A continuous steering-wheel sinusoid is applied when the vehicle is driven in a straight line at 100 km/h as defined in [74]. Steering frequencies from 0.2 Hz to 1 Hz in 0.2 Hz steps are applied and results obtained with different cases of active suspension are compared with the passive suspension. The ratios of the RMS roll angle obtained with the two active suspension methods over the one computed with the passive suspension are shown in Figure 5.12. This ratio remains around 50% in most of the cases for 'PALS-PID', while the ratio for the feedforward controller remains below 20% in most cases with lateral acceleration $a_y \leqslant 6\, m/s^2$ and rises to 40% at a_y=8 m/s^2 at the whole steering frequency range, which indicate better performance in terms of chassis leveling than 'PALS-PID'.

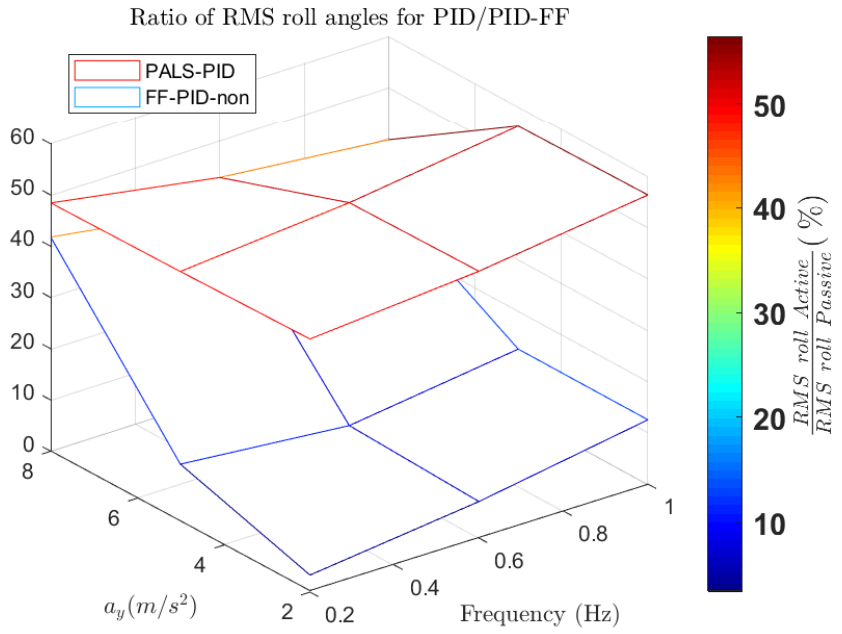


Figure 5.12: Numerical simulation results: Ratio of RMS roll angles obtained with different cases of active and passive suspensions when the vehicle performs a sinusoid steering-wheel manoeuvre.

5.5 Conclusion

The recently proposed mechatronic suspension of the Parallel Active Link Suspension (PALS) is investigated in the application to a SUV full car [5], with feedforward compensation taken into consideration in the suspension control design, revealing promising potential for chassis leveling and stabilisation.

The proposed feedforward PID control strategy with nonlinear polynomial fitting method applied is proposed for PALS low-frequency application, with essential improvement over the passive suspension system and decent enhancement as compared to 'PALS-PID' in terms of chassis leveling and speed of response over a set of ISO driving manoeuvres.

In future work, the PALS performance in higher-frequency road events (i.e. speed

bump and random road) is to be tested for the integration of H_∞ control (μ-synthesis control) described in section 3 and the proposed feedforward PID control. The ride comfort and road holding related variables (CMC vertical acceleration and the tire deflection) require a more comprehensive assessment of the PALS performance before any on-road experiments.

Chapter 6

Improved ride comfort and road holding through LMI-based robust MPC for a quarter-car model with SAVGS

6.1 Introduction

In this chapter, the LMI-based robust model predictive control is employed based on the result in [77] for a linear equivalent model of the SAVGS quarter car, considering physical constraints on the robust MPC formulation to guarantee robustness. Importantly, to reduce the aforementioned conservativeness due to offline calculation in [78], the feedback gain and control perturbation in the proposed RMPC scheme are considered decision variables and are computed online at each time iteration to improve performance.

The main contributions of this chapter are: i) the development of the uncertain system to capture the model mismatch between linear equivalent model and nonlin-

ear high fidelity model, ii) development of embedded online robust MPC together with PID control considering constraints to improve suspension performance while guaranteeing the robustness and stability, and iii) numerical simulations with a nonlinear multi-body model of the SAVGS quarter car to assess the effectiveness and robustness of the proposed control scheme, as compared to the passive suspension and the actively controlled SAVGS by H_∞ control.

The rest of the chapter is structured as follows: Section 6.2 illustrates the nonlinear and linearised model and describes how the uncertainties are employed in those models. Section 6.3 designs a robust control scheme with the bounded disturbance and structured uncertainties taken into consideration. Section 6.4 combines the robust MPC scheme detailed in section 6.3 with a PID scheme to develop the overall scheme to improve suspension performance. Section 6.5 performs numerical simulations to compare the developed schemes to the H_∞ control and the passive suspension case, with the ride comfort and road holding being the primary indexes. Finally, concluding remarks are discussed in Section 6.6.

6.1.1 Notation

$\mathbb{R}$ denotes the set of real numbers, $\mathbb{R}^n$ denotes the space of n-dimensional real (column) vectors, $\mathbb{R}^{n\times m}$ denotes the space of $n \times m$ real matrices. $\mathcal{H}(A) \coloneqq A+A^T$ for $A \in \mathbb{R}^{n\times n}$ and A^T denotes the transpose of A. If $\boldsymbol{V} \subseteq \mathbb{R}^{p\times q}$ is a subspace, then $\mathcal{B}\boldsymbol{V} = \{V \in \boldsymbol{V} : VV^T \preceq 1\}$ denotes the unit ball of $\boldsymbol{V}$.

6.2 Suspension model and design requirements

In this section, the high fidelity nonlinear multi-body quarter car SAVGS model described in subsection 2.2.2.1 is applied for nonlinear simulations and evaluation first. In addition, the linear equivalent model of the quarter car SAVGS derived in

subsection 2.2.4.1 is proved to be accurate enough to control the vehicle suspension problem. Finally, by characterising the uncertainties in the linear equivalent model, the uncertain system is first derived to capture the dynamics and nonlinearity of the actual system.

6.2.1 Quarter Car SAVGS linear equivalent model

As described in subsection 2.2.4.1, a linear equivalent model of the SAVGS quarter car shown in Figure2.5 is utilised to enable the linear robust control synthesis. The state space equations of the quarter car SAVGS linear equivalent model are listed as follows:

$$\begin{aligned} \dot{x} &= Ax + Bu \\ y &= Cx + Du \end{aligned} \tag{6.1}$$

where the the system state and the outputs and inputs can be referred to (2.4).

The matrices in (6.1) are

$$A = \begin{bmatrix} -\frac{c_{eq}}{m_s} & \frac{c_{eq}}{m_s} & \frac{k_{eq}}{m_s} & 0 & -\frac{k_{eq}}{m_s} \\ -\frac{c_{eq}}{m_u} & -\frac{c_{eq}+c_t}{m_u} & -\frac{k_{eq}}{m_u} & \frac{k_t}{m_u} & \frac{k_{eq}}{m_u} \\ -1 & 1 & 0 & 0 & 0 \\ 0 & -1 & 0 & 0 & 0 \\ 0 & 0 & 0 & 0 & 1 \end{bmatrix}, B = \begin{bmatrix} -\frac{c_{eq}}{m_s} & 0 \\ \frac{c_{eq}}{m_u} & \frac{c_t}{m_u} \\ 0 & 0 \\ 0 & 1 \\ 1 & 0 \end{bmatrix}, \tag{6.2}$$

6.2.2 Quarter Car SAVGS Uncertain system

It is believed that by considering the uncertainties in the linearised system for designing a controller, nonlinearities and unmodeled dynamics for the actual suspension system can be approximately captured, which provides a more reliable basis for designing a robust controller [79]. Therefore, in this study, one of the main objectives

is to close the gab between the nonlinear system and its equivalent linear version presented in Section 6.2.1. The first step for doing so, it is to consider the variable $\dot{z}_r$ as a disturbance signal ($d = \dot{z}_r$) instead of an input signal, since the road profile and its deviation cannot be controlled. d is a symmetric bounded signal where the upper and lower bound of the signal are $\bar{d}$ and $-\bar{d}$ indicating the maximum and minimum vertical road velocity given the road profile known in advance. As in the mu-synthesis control case in subsection 3.2.1, the suspension damping coefficient c_{eq} is described as a (time-invariant) uncertain parameter due to the relationship of operating speed range and the damping ratio, which have nonlinear speed-dependent characteristics. But instead of using the structured uncertainty in the form of block diagonal matrix in (3.23), now the suspension damping variation from the nominal value can be captured by the introduction of the time-invariant norm-bounded structured uncertainty operator Δ and the uncertain input and output signals $p(t)$ and $q(t)$, respectively [80], where the $p(t)$ and $q(t)$ are used to describe the uncertain system in a feedback way (see below in (6.3). Therefore, the new suspension system subject to additive disturbances and structured feedback uncertainties can be described as follows:

$$\begin{aligned} \dot{x}(t) &= Ax(t) + B_u u(t) + B_p p(t) + B_d d(t), \\ q(t) &= C_q x(t) + D_{qu} u(t), \\ p(t) &= \Delta_t q(t). \end{aligned} \tag{6.3}$$

The matrices in (6.3) are:

$$
\begin{aligned}
A &= \begin{bmatrix} -\frac{c_{eq}^{(nom)}}{m_s} & \frac{c_{eq}^{(nom)}}{m_s} & \frac{k_{eq}}{m_s} & 0 & -\frac{k_{eq}}{m_s} \\ -\frac{c_{eq}^{(nom)}}{m_u} & -\frac{c_{eq}^{(nom)}+c_t}{m_u} & -\frac{k_{eq}}{m_u} & \frac{k_t}{m_u} & \frac{k_{eq}}{m_u} \\ -1 & 1 & 0 & 0 & 0 \\ 0 & -1 & 0 & 0 & 0 \\ 0 & 0 & 0 & 0 & 1 \end{bmatrix}, B_u = \begin{bmatrix} -\frac{c_{eq}^{(nom)}}{m_s} \\ \frac{c_{eq}^{(nom)}}{m_u} \\ 0 \\ 0 \\ 1 \end{bmatrix}, \\
B_d^T &= \begin{bmatrix} 0 & \frac{c_t}{m_u} & 0 & 1 & 0 \end{bmatrix}, \quad B_p^T = \begin{bmatrix} \frac{1}{m_s} & -\frac{1}{m_u} & 0 & 0 & 0 \end{bmatrix}, \\
C_q &= \begin{bmatrix} -c_{eq}^{(dev)} & c_{eq}^{(dev)} & 0 & 0 & 0 \end{bmatrix}, \quad D_{qu} = \begin{bmatrix} -c_{eq}^{(dev)} \end{bmatrix},
\end{aligned}
\tag{6.4}
$$

where $c_{eq}^{(nom)}$ and $c_{eq}^{(dev)}$ denote the nominal value and the maximum deviation of suspension damping coefficient c_{eq}, respectively, which can be shown as:

$$
c_{eq} = c_{eq}^{(nom)} \pm c_{eq}^{(dev)} \tag{6.5}
$$

Taking into account the operational speed range, it is assumed that the value c_{eq}, presented on the linear equivalent model, can be within a $\pm 10\%$ range of its nominal value ($c_{eq}^{(min)} \leq c_{eq} \leq c_{eq}^{(max)}$), where $c_{eq}^{(max)} = 1.1 c_{eq}^{(nom)}$ and $c_{eq}^{(min)} = -1.1 c_{eq}^{(nom)}$. Based on this bounds, the maximum deviation of the damping coefficient is defined as $c_{eq}^{(dev)} = 0.5(c_{eq}^{(max)} - c_{eq}^{(min)})$. Since we have only one uncertainty parameter which is the damping coefficient c_{eq}, the uncertainty operator has the form $\Delta := \{\Delta \in \mathbb{R} : \Delta^T \Delta \leq 1\}$ and the disturbances set is bounded $\mathcal{D} := \{d \in \mathbb{R}^{n_d} : -\bar{d} \leq d_k \leq \bar{d}\}$.

Since the robust control design presented subsequently in Section 6.3 is developed using a discrete-time model, the continuous-time model in (6.3) is discretised using

a zero-order hold method, where the discrete model is defined as:

$$\begin{aligned} x_{k+1} &= Ax_k + B_u u_k + B_p p_k + B_d d_k, \\ q_k &= C_q x_k + D_{qu} u_k, \\ p_k &= \Delta_k q_k. \end{aligned} \tag{6.6}$$

Note here that the distribution matrices A, B_u, B_p and etc. in (6.6) are the discretised version of those in (6.3) and the same notation is used for simplicity.

6.2.3 Objectives and constraints requirements

In this study, the ride comfort and road holding are selected as the two main control objectives in suspension design [67, 68, 69]. As described in subsection 2.3.2, the vertical body acceleration $\ddot{z}_s$ and the tire deflection Δl_t should be kept as small as possible. In contrast, due to structural limitations and the physical capabilities of the actuators, the three hard constraints in this study are the single-link angle θ_{SL}, the single-link angular velocity (which is the control input) ω_{SL} and low speed shaft torque T_{lss}. In other words, these three variables should not exceed their predefined limits. To achieve an acceptable performance, the root mean square (RMS) values of the vertical body acceleration and the tire deflection need to be minimised, with the values of θ_{SL}, ω_{SL} and T_{lss} satisfying their expected bounds.

6.3 Robust Model Predictive Control Design

In this section, the causal state-feedback RMPC methodology employed for the SAVGS quarter car control problem is summarised (see [77] for further details). The general form of a system description including control dynamics, constraints and cost signal are first provided. Then the algebraic formulation of an online and

offline controller, which are applied to steer a system to an admissible reference signal is explained. Considering a causal state feedback control law, the optimisation problem aims to compute a state-feedback gain and a control perturbation by solving linear matrix inequalities, where the the computational burden is substantially reduced without adversely affecting the tracking performance. An offline strategy to guarantee feasibility of the RMPC problem is also introduced. Finally, the overall RMPC algorithm utilised in this paper is presented to summarise the control strategy that is followed.

6.3.1 System Description

Following the representation described in section (6.2.2), the general form of the linear discrete-time system, subject to bounded disturbances and norm-bounded structured uncertainty is illustrated as [80]:

$$\begin{bmatrix} x_{k+1} \\ q_k \\ f_k \\ z_k \end{bmatrix} = \begin{matrix} n \\ n_q \\ n_f \\ n_z \end{matrix} \overset{\begin{matrix} n & n_u & n_p & n_d \end{matrix}}{\begin{bmatrix} A & B_u & B_p & B_d \\ C_q & D_{qu} & 0 & 0 \\ C_f & D_{fu} & D_{fp} & D_{fd} \\ C_z & D_{zu} & D_{zp} & D_{zd} \end{bmatrix}} \begin{bmatrix} x_k \\ u_k \\ p_k \\ d_k \end{bmatrix}, p_k = \Delta_k q_k,$$
$$\begin{bmatrix} q_N \\ f_N \\ z_N \end{bmatrix} = \begin{bmatrix} \hat{C}_q & 0 \\ \hat{C}_f & \hat{D}_{fp} \\ \hat{C}_z & \hat{D}_{zp} \end{bmatrix} \begin{bmatrix} x_N \\ p_N \end{bmatrix}, \qquad p_N = \Delta_N q_N, \tag{6.7}$$

where $x_k \in \mathbb{R}^n$, $u_k \in \mathbb{R}^{n_u}$, $d_k \in \mathbb{R}^{n_d}$, $f_k \in \mathbb{R}^{n_f}$, $z_k \in \mathbb{R}^{n_z}$, $p_k \in \mathbb{R}^{n_p}$ and $q_k \in \mathbb{R}^{n_q}$ are the state, input, disturbance, constraint, cost, and input and output uncertainty vectors, respectively, with $k \in \mathcal{N} := \{0, 1, \ldots, N-1\}$, where N is the horizon length. It is assumed that all the states are measurable in this study and the description

includes terminal cost and state constraints to ensure closed-loop stability [81]. $\Delta_k \in \boldsymbol{\mathcal{B}\Delta}$ where $\boldsymbol{\Delta} \subseteq \mathbb{R}^{n_p \times n_q}$ is a subspace that captures the uncertainty structure. Finally, the disturbance d_k is assumed to belong to the set $\mathcal{D}_k = \{d_k \in \mathbb{R}^{n_d} \colon -\bar{d}_k \leq d_k \leq \bar{d}_k\}$, where the disturbance's upper bound is $\bar{d}_k > 0$ and assumed known or approximated by the application specification (see Section 6.5 for example).

6.3.2 Problem formulation

Given the initial state x_0, the design of the robust model predictive controller for all $k \in \mathcal{N}$ leads to the problem of finding a feedback law u_k all for $k \in N$ such that the cost function

$$J = \max_{d \in \mathcal{D}_k, \Delta \in \boldsymbol{\mathcal{B}\Delta}} \sum_{k=0}^{N} (z_k - \bar{z}_k)^T (z_k - \bar{z}_k), \tag{6.8}$$

is minimised, while the future predicted outputs satisfy the constraints $f_k \leq \bar{f}_k$ and $f_N \leq \bar{f}_N$ for all $d_k \in \mathcal{D}_k$ and all $\Delta \in \boldsymbol{\mathcal{B}\Delta}$ and for all $k \in N$. The parameter $\bar{z}_k$ defines the reference trajectory and $\bar{f}_k$ and $\bar{f}_N$ are chosen to include polytopic constraints on input, state and output signals, and terminal signals respectively.

To simplify the presentation, the disturbance is re-parameterised as uncertainty by redefining $\mathcal{D}_k := \{\Delta_k^d \bar{d}_k \colon \Delta_k^d \in \boldsymbol{\mathcal{B}\Delta}^d\}$, where $\boldsymbol{\Delta}^d = \mathbb{D}^{n_d}$ and,

$$B_p := \begin{bmatrix} B_p & B_d \end{bmatrix}, C_q := \begin{bmatrix} C_q \\ 0 \end{bmatrix}, D_{qu} := \begin{bmatrix} D_{qu} \\ 0 \end{bmatrix}, \bar{d}_k := \begin{bmatrix} 0 \\ \bar{d}_k \end{bmatrix}, p_k := \begin{bmatrix} p_k \\ d_k \end{bmatrix},$$

$q_k := C_q x_k + D_{qu} u_k + \bar{d}_k$ and $n_p := n_p + n_d, n_q := n_q + n_d$.

By defining the stacked vectors,

$$\mathbf{u} = \begin{bmatrix} u_0 \\ \vdots \\ u_{N-1} \end{bmatrix} \in \mathbb{R}^{N_u},\ \mathbf{x} = \begin{bmatrix} x_1 \\ \vdots \\ x_N \end{bmatrix} \in \mathbb{R}^{N_n},\ \boldsymbol{\zeta} = \begin{bmatrix} \zeta_0 \\ \vdots \\ \zeta_N \end{bmatrix} \in \mathbb{R}^{N_\zeta},$$

where $\boldsymbol{\zeta}$ stands for $\mathbf{f}, \bar{\mathbf{f}}, \mathbf{p}, \mathbf{q}, \mathbf{z}, \bar{\mathbf{z}}$ or $\bar{\mathbf{d}}$ and $N_n = Nn$, $N_u = Nn_u$ and $N_\zeta = (N+1)n_\zeta$, we get

$$\begin{bmatrix} \mathbf{x} \\ \mathbf{q} \\ \mathbf{f} \\ \mathbf{z} \end{bmatrix} = \begin{matrix} N_n \\ N_q \\ N_f \\ N_z \end{matrix} \overset{\begin{matrix} n & N_u & N_p & 1 \end{matrix}}{\begin{bmatrix} \mathbf{A} & \mathbf{B}_u & \mathbf{B}_p & 0 \\ \mathbf{C}_q & \mathbf{D}_{qu} & \mathbf{D}_{qp} & \bar{\mathbf{d}} \\ \mathbf{C}_f & \mathbf{D}_{fu} & \mathbf{D}_{fp} & 0 \\ \mathbf{C}_z & \mathbf{D}_{zu} & \mathbf{D}_{zp} & 0 \end{bmatrix}} \begin{bmatrix} x_0 \\ \mathbf{u} \\ \mathbf{p} \\ 1 \end{bmatrix}, \quad \mathbf{p} = \hat{\Delta}\mathbf{q}, \tag{6.9}$$

with $\hat{\Delta} \in \boldsymbol{\mathcal{B}}\hat{\boldsymbol{\Delta}} \subset \mathbb{R}^{N_p \times N_q}$ where,

$$\hat{\boldsymbol{\Delta}} = \{\mathrm{diag}(\Delta_0, \Delta_0^w, \ldots, \Delta_{N-1}, \Delta_{N-1}^w, \Delta_N) : \Delta_k \in \boldsymbol{\Delta}, \Delta_k^w \in \boldsymbol{\Delta}^w\},$$

and where the stacked matrices in (6.9) (shown in bold) have the indicated dimensions and are readily obtained from iterating the dynamics in (6.7).

The input signal u_i is considered as a causal state feedback that depends only on states $x_0, \ldots, x_i$ (see e.g. [82]). Thus

$$\mathbf{u} = K_0 x_0 + K\mathbf{x} + \boldsymbol{v}, \tag{6.10}$$

where $\boldsymbol{v} \in \mathbb{R}^{N_u}$ is the (stacked) control perturbation vector and K_0, K are the current and predicted future state feedback gains. Causality is preserved by restricting $[K_0\ K] \in \mathcal{K} \subset \mathbb{R}^{N_u \times N_n}$, where $\mathcal{K}$ is lower block diagonal with $n_u \times n$ blocks and

$\boldsymbol{v} \in \mathbb{R}^{N_u}$ is the (stacked) control perturbation vector.

Using the definition of $\mathbf{x}$ in equation (6.9) the control law in (6.10) can be rewritten as:

$$\mathbf{u} = \hat{K}_0 x_0 + \hat{K}\mathbf{B}_p\mathbf{p} + \hat{v}, \tag{6.11}$$

where

$$\begin{bmatrix} \hat{K}_0 & \hat{K} & \hat{v} \end{bmatrix} = (I - K\mathbf{B}_u)^{-1} \begin{bmatrix} K_0 + K\mathbf{A} & K & \boldsymbol{v} \end{bmatrix}. \tag{6.12}$$

Note that $(I - K\mathbf{B}_u)$ is invertible due to the lower-triangular structure and that $\mathbf{u}$ is affine in $\hat{K}_0, \hat{K}$ and $\hat{\boldsymbol{v}}$ which have the same structure as K_0, K and $\boldsymbol{v}$. A standard feedback re-parameterisation gives

$$\begin{bmatrix} K_0 & K & \boldsymbol{v} \end{bmatrix} = (I + \hat{K}\mathbf{B}_u)^{-1} \begin{bmatrix} \hat{K}_0 - \hat{K}\mathbf{A} & \hat{K} & \hat{\boldsymbol{v}} \end{bmatrix}, \tag{6.13}$$

and so $\begin{bmatrix} \hat{K}_0 & \hat{K} & \hat{v} \end{bmatrix}$ will be used as the decision variables instead. Using (6.11) to eliminate $\mathbf{u}$ from (6.9) and re-arranging x_0 gives

$$\begin{aligned} \begin{bmatrix} \mathbf{q} \\ \mathbf{f} \\ \mathbf{z} - \bar{\mathbf{z}} \end{bmatrix} &= \left[\begin{array}{c|c} \mathbf{D}_{qp}^{\hat{K}} & \mathbf{D}_{q}^{\hat{K}_0,\hat{v}} \\ \hline \mathbf{D}_{fp}^{\hat{K}} & \mathbf{D}_{f}^{\hat{K}_0,\hat{v}} \\ \hline \mathbf{D}_{zp}^{\hat{K}} & \mathbf{D}_{z}^{\hat{K}_0,\hat{v}} \end{array}\right] \begin{bmatrix} \mathbf{p} \\ 1 \end{bmatrix}, \\ &:= \left[\begin{array}{c|c} \mathbf{D}_{qp} + \mathbf{D}_{qu}\hat{K}\mathbf{B}_p & \mathbf{D}_{qu}\hat{v} + (\mathbf{C}_q + \mathbf{D}_{qu}\hat{K}_0)x_0 + \bar{d} \\ \hline \mathbf{D}_{fp} + \mathbf{D}_{fu}\hat{K}\mathbf{B}_p & \mathbf{D}_{fu}\hat{v} + (\mathbf{C}_f + \mathbf{D}_{fu}\hat{K}_0)x_0 \\ \hline \mathbf{D}_{zp} + \mathbf{D}_{zu}\hat{K}\mathbf{B}_p & \mathbf{D}_{zu}\hat{v} + (\mathbf{C}_z + \mathbf{D}_{zu}\hat{K}_0)x_0 - \bar{z} \end{array}\right] \begin{bmatrix} \mathbf{p} \\ 1 \end{bmatrix}. \end{aligned} \tag{6.14}$$

Note that all the coefficient matrices in (6.14) are affine in $\hat{K}_0$, $\hat{K}$ and $\hat{v}$. Finally, eliminating $\mathbf{p}$ using $\mathbf{p} = \hat{\Delta}\mathbf{q}$ we get

$$\begin{bmatrix} \mathbf{f} \\ \mathbf{z} - \bar{\mathbf{z}} \end{bmatrix} = \begin{bmatrix} \mathbf{D}_{f}^{\hat{K}_0,\hat{v}} + \mathbf{D}_{fp}^{\hat{K}}\hat{\Delta}(I - \mathbf{D}_{qp}^{\hat{K}}\hat{\Delta})^{-1}\mathbf{D}_{q}^{\hat{K}_0,\hat{v}} \\ \mathbf{D}_{z}^{\hat{K}_0,\hat{v}} + \mathbf{D}_{zp}^{\hat{K}}\hat{\Delta}(I - \mathbf{D}_{qp}^{\hat{K}}\hat{\Delta})^{-1}\mathbf{D}_{q}^{\hat{K}_0,\hat{v}} \end{bmatrix}. \tag{6.15}$$

For convenience, constraint and cost signals can be written as $\mathbf{f} = \mathcal{F}(\hat{K}_0, \hat{K}, \hat{v}, \hat{\Delta})$ and $(\mathbf{z}-\bar{\mathbf{z}})^T(\mathbf{z}-\bar{\mathbf{z}}) = \mathcal{Z}(\hat{K}_0, \hat{K}, \hat{v}, \hat{\Delta})$ to emphasise dependence on the variables.

By following the procedure presented by [83], the RPMC problem can be transformed to a min-max problem [84], where the objective is to find a feasible triple $(\hat{K}_0, \hat{K}, \hat{v})$ that solves

$$\mathbf{J} = \min_{(\hat{K}_0, \hat{K}, \hat{v}) \in \mathcal{U}} \max_{\hat{\Delta} \in \boldsymbol{\mathcal{B}}\boldsymbol{\Delta}} \mathcal{Z}(\hat{K}_0, \hat{K}, \hat{v}, \hat{\Delta}), \tag{6.16}$$

The set $\mathcal{U}$ is defined as shown in [77] to be the set of all feasible control variables $(\hat{K}_0, \hat{K}, \hat{v})$ such that all the problem constraints are satisfied:

$$\mathcal{U} := \{([\hat{K}_0 \ \hat{K}], \hat{v}) \in \mathcal{K} \times \mathbb{R}^{N_u} : \mathcal{F}(\hat{K}_0, \hat{K}, \hat{v}, \hat{\Delta}) \leq \bar{\mathbf{f}}, \forall \hat{\Delta} \in \boldsymbol{\mathcal{B}}\hat{\boldsymbol{\Delta}}\}. \tag{6.17}$$

Since the optimisation in (6.16) is nonconvex, the semidefinite relaxation procedure presented in[83, Lemma 1], is used by introducing an upper bound on the cost function (6.16), defined by γ^2. After some matrix manipulations the inequality, $\mathcal{Z}(\hat{K}_0, \hat{K}, \hat{v}, \hat{\Delta}) \leq \gamma^2$ and $\mathcal{F}(\hat{K}_0, \hat{K}, \hat{v}, \hat{\Delta}) \leq \bar{\mathbf{f}}$ holds for all $\hat{\Delta} \in \boldsymbol{\mathcal{B}}\hat{\boldsymbol{\Delta}}$ if there exists a solution to the nonlinear matrix inequalities: [77]

$$T_1 + \mathcal{H}(T_2 \hat{K} \mathbf{B}_p T_3) \succ 0, \tag{6.18}$$

$$T_1^i + \mathcal{H}(T_2^i \hat{K} \mathbf{B}_p T_3^i) \succ 0, \ i = 1, \ldots, N_f, \tag{6.19}$$

where

$$\begin{bmatrix} T_1 & T_2 \\ T_3 & 0 \end{bmatrix} = \begin{array}{c} \\ N_z \\ 1 \\ N_q \\ N_p \\ N_p \end{array} \begin{array}{c} \begin{array}{cccc} N_z & 1 & N_q & N_p \end{array} \\ \left[\begin{array}{cccc|c} I & \mathbf{D}_z^{\hat{K}_0,\hat{v}} & \mathbf{D}_{zp}G^T & \mathbf{D}_{zp}S & \mathbf{D}_{zu} \\ * & \gamma^2 & (\mathbf{D}_q^{\hat{K}_0,\hat{v}})^T & 0 & 0 \\ * & * & R+\mathcal{H}\big(\mathbf{D}_{qp}G^T\big) & \mathbf{D}_{qp}S & \mathbf{D}_{qu} \\ * & * & * & S & 0 \\ \hline 0 & 0 & G^T & S & 0 \end{array}\right] \end{array} \begin{array}{c} \\ N_u \end{array},$$

$$\begin{bmatrix} T_1^i & T_2^i \\ T_3^i & 0 \end{bmatrix} =$$

$$\begin{array}{c} \\ 1 \\ N_q \\ N_p \\ N_p \end{array} \begin{array}{c} \begin{array}{ccc} 1 & N_q & N_p \end{array} \\ \left[\begin{array}{ccc|c} e_i^T(\bar{\mathbf{f}}-\mathbf{D}_f^{\hat{K}_0,\hat{v}}) & (\mathbf{D}_q^{\hat{K}_0,\hat{v}})^T- \frac{e_i^T}{2}\mathbf{D}_{fp}G_i^T & -\frac{e_i^T}{2}\mathbf{D}_{fp}S_i & -\frac{e_i^T}{2}\mathbf{D}_{fu} \\ * & R_i+\mathcal{H}\big(\mathbf{D}_{qp}G_i^T\big) & \mathbf{D}_{qp}S_i & \mathbf{D}_{qu} \\ * & * & S_i & 0 \\ \hline 0 & G_i^T & S_i & 0 \end{array}\right] \end{array} \begin{array}{c} \\ N_u \end{array},$$

where $([\hat{K}_0\ \hat{K}],\hat{v}) \in \mathcal{K} \times \mathbb{R}^{N_u}$ and $(S,R,G), \in \hat{\Psi}$ are slack variables with $\hat{\Psi}$ which is defined as:

$$\widehat{\Psi} = \{(S,R,G) \colon S,R \succ 0,\ S\Delta = \Delta R,\ \mathcal{H}(\Delta G) = 0\, \forall \Delta \in \widehat{\mathbf{\Delta}}\}. \tag{6.20}$$

In this study, instead of solving multible nonlinear matrix inequalities for the constraints as presented in (6.19) (one for each of the N_f constraints), a single nonlinear inequality is defined for all constraints, similarly to [77]. By doing so a reduction on the computational complexity and algorithm scalability can be achieved. Therefore without loss of generality, the multiple nonlinear inequalities presented in (6.19) can be written as a single nonlinear inequality as shown below:

$$\tilde{T}_1 + \mathcal{H}(\tilde{T}_2 \hat{K} \mathbf{B}_p \tilde{T}_3) \succ 0, \tag{6.21}$$

where $\begin{bmatrix} \tilde{T}_1 & \tilde{T}_2 \\ \tilde{T}_3 & 0 \end{bmatrix} =$

$$\begin{array}{c} \\ 1 \\ N_f \\ N_q \\ N_p \\ \hline N_p \end{array} \begin{array}{c} \begin{array}{cccc|c} 1 & N_f & N_q & N_p & N_u \end{array} \\ \left[\begin{array}{cccc|c} 2\mu\ (\bar{\mathbf{f}} - \mathbf{D}_f^{\hat{K}_0,\hat{\upsilon}} - Me - e\mu)^T & (\mathbf{D}_q^{\hat{K}_0,\hat{\upsilon}})^T & 0 & 0 \\ * & M + M^T & -\mathbf{D}_{fp}\tilde{G}^T & -\mathbf{D}_{fp}\tilde{S} & -\mathbf{D}_{fu} \\ * & * & \tilde{R} + \mathcal{H}(\mathbf{D}_{qp}\tilde{G}^T) & \mathbf{D}_{qp}\tilde{S} & \mathbf{D}_{qu} \\ * & * & * & \tilde{S} & 0 \\ \hline 0 & 0 & \tilde{G}^T & \tilde{S} & 0 \end{array}\right], \end{array}$$

It follows that the relaxed RMPC problem can be summarised as:

$$\begin{aligned} \min\{\gamma^2 : ([\hat{K}_0 \quad \hat{K}], \hat{\upsilon}) \in \mathcal{K} \times \mathbb{R}^{N_u}, (6.18), (6.21) \text{ are satisfied,} \\ (S, R, G) \in \widehat{\Psi},\ i \in \mathcal{N}_f\}. \end{aligned} \tag{6.22}$$

The non-linearities appear in (6.18,6.21) due to terms of the form $\hat{K}\mathbf{B}_p\Phi^T$ where Φ stands for S, G, $\tilde{S}$ and $\tilde{G}$. By introducing three new slack variables Y, $\tilde{Y}$ and X and using Elimination lemma derived in [77], the problem can be linearised into two LMIs described below in (6.23) and (6.24):

$$\begin{bmatrix} T_1 + \mathcal{H}\left(T_2 \bar{K} Y^*\right) & * \\ \left(\mathbf{B}_p T_3 - \bar{K}^T T_2^T\right) - XY^* & X + X^T \end{bmatrix} \succ 0 \tag{6.23}$$

$$\begin{bmatrix} \tilde{T}_1 + \mathcal{H}\left(\tilde{T}_2 \bar{K} \tilde{Y}^*\right) & * \\ \left(\mathbf{B}_p \tilde{T}_3 - \bar{K}^T \tilde{T}_2^T\right) - X\tilde{Y}^* & X + X^T \end{bmatrix} \succ 0, \tag{6.24}$$

for any $Y^* \in \mathbb{R}^{N_n \times (N_z + 1 + N_q + N_p)}$, $\tilde{Y}^* \in \mathbb{R}^{N_n \times (1 + N_f + N_q + N_p)}$ and where $\bar{K} := \hat{K}X \in \mathcal{K}$ and let $Y^* = \mathbf{B}_p T_3(S^*, G^*) + (T_2\hat{K}^*)^T$ and $\tilde{Y}^* = \mathbf{B}_p \tilde{T}_3(\tilde{S}^*, \tilde{G}^*) + (\tilde{T}_2\hat{K}^*)^T$. Then

(6.23) and (6.24) are feasible. The proposed LMI-based RMPC scheme does not restrict the structure of the slack variables (R, S, G) beyond the requirements of $\widehat{\Psi}$, and the reformulation of a single inequality for the constrained signal does not add any additional conservativeness into the problem; see [77] for more details.

The above formulation shows that the initial non-convex and non-linear RMPC problem can be written as an LMI optimisation problem [85]. K_0, K and $\boldsymbol{\upsilon}$ can be computed online and applied in the usual receding horizon MPC manner, where the first input of the control sequence $\mathbf{u}$ is applied to the plant, the time window is shifted by 1, the current state is read and the process is repeated.

In this study, lookup table is built up offline to map all the initial state $x_0 \in \mathcal{X}$ to the corresponding Y^* and $\tilde{Y}^*$. Then the offline calculation is implemented to update the initial guesses of $\tilde{S}^*, \tilde{G}^*, \hat{K}^*$ once, after which the initial feasible solutions $Y^*(S^*, G^*, \hat{K}^*)$ and $\tilde{Y}^*(\tilde{S}^*, \tilde{G}^*, \hat{K}^*)$ are obtained and fed online (for more details refer to [77].

By following the description that is given for both offline and online controllers, the RMPC strategy that is employed in this thesis is summarised in Algorithm 1:

6.4 Overall control scheme

In this section, the issues encountered when adapting the RMPC synthesised in Section 6.3 to the nonlinear multi-body model of quarter car SAVGS introduced in subsection 2.2.2.1 are fully discussed.

6.4.1 PI control to solve the single link drifting

The linear equivalent model in subsection 2.2.4.1 cannot achieve the zero value convergence of linear actuator displacement ($\Delta z_{lin} = 0$) and thereby the single link

Algorithm 1: RMPC controller strategy

Offline calculation:
1. Build the lookup table to map all the initial state $x_0 \in \mathcal{X}$ to the corresponding Y^* and $\tilde{Y}^*$.
2. Compute the initial feasible solutions Y^* and $\tilde{Y}^*$, by reading the lookup table given first initial state x_0, and fix the value of Y^* and $\tilde{Y}^*$ for the later on online calculation

Online calculation:
1. Read the current state x_k and set it as initial state x_0. Then based on x_0, extract the value of Y^* and $\tilde{Y}^*$ from offline calculation.
2. Compute the triple (K_0, K, υ) through the two LMI procedures outlined in (6.23) and (6.24) and apply the first input of the control sequence shown in (6.10).
3. Return to step 1.

angle $\Delta\theta_{SL}$ cannot be steered to the trim state of $\Delta\theta_{SL} = 90^\circ$ in high frequency. In previous work [4], the transfer function filtering the output $\dot{z}_{lin}$ has a free integrator and aims to ensure a zero steady-state tracking error of the Δz_{lin}. However, in this thesis, a more conventional approach is utilised which introduces the PI control based on the uncertain system developed in subsection 6.2.2 to ensure zero steady-state error of Δz_{lin}. As shown in Figure 6.1, the exogenous reference signal $z_{lin}^{(ref)} = 0$ is introduced representing nominal equilibrium of θ_{SL}, and its tracking error ($z_{lin}^{(trk)} := z_{lin}^{(ref)} - z_{lin} = rx$, where $r = [0\,0\,0\,0\,1]$ is the scalar and x is the state) is fed back into the PI controller of the form:

$$\Delta z_{lin}^* = K_p z_{lin}^{(trk)} + K_i \int z_{lin}^{(trk)}. \tag{6.25}$$

The parameters K_p and K_i can be tuned using the approach in [21]. Therefore, the augmented system combines the uncertain system (6.6) and the PI control (6.25), which, after descretisation, can be described as follows:

$$\bar{x}(k+1) = \bar{A}\bar{x}(k) + \bar{B}_u u(k) + \bar{B}_p p(k) + \bar{B}_d d(k), \tag{6.26}$$

where $\bar{x} = [x^T \quad \int(z_{lin}^{(ref)} - z_{lin})]^T$ is the augmented state and where

$$\bar{A} = \begin{bmatrix} A + B_u K_p r & B_u K_i \\ r & 0 \end{bmatrix}, \quad \bar{B}_u = \begin{bmatrix} B_u \\ 0 \end{bmatrix}, \quad \bar{B}_d = \begin{bmatrix} B_d \\ 0 \end{bmatrix}, \quad \bar{B}_p = \begin{bmatrix} B_p \\ 0 \end{bmatrix}, \tag{6.27}$$

where the matrices A, B_u, B_d, B_p, are defined in (6.4). Then the robust model

-

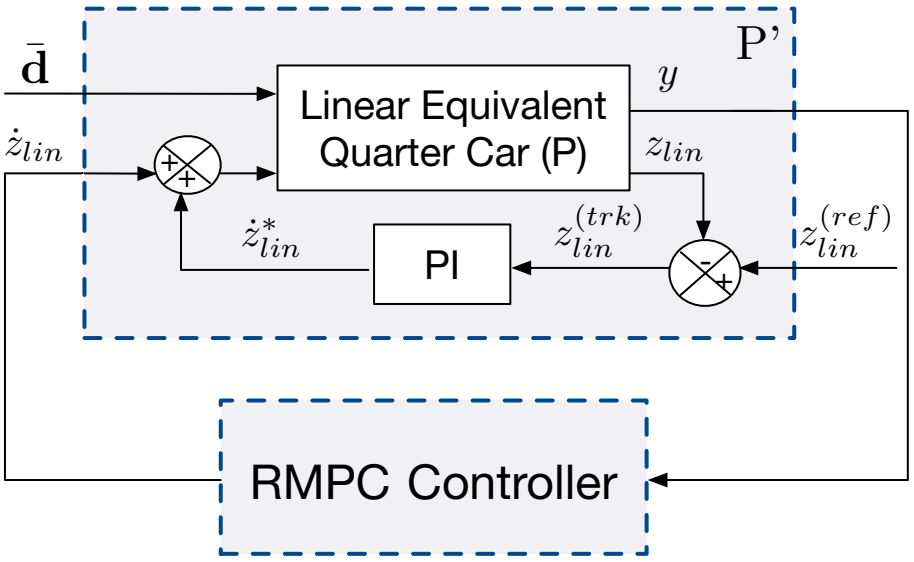


Figure 6.1: PI incorporated plant model of quarter car SAVGS, where $\bar{\mathrm{d}}$ corresponds to the stack vector for disturbance bound, P' to the new uncertain system with parallel PI incorporated, and $z_{lin}^{(ref)}$ to the exogenous reference signal of linear actuator displacement.

6.4.2 Selection of the disturbance in Robust MPC design

Apart from the single link drifting issue, the boundary of disturbance ($\bar{d}$) which is based on the road profile is initially chosen as the maximum value of the vertical road velocity (known in the simulation). However, when implementing this value in the different driving manoeuvres, it is hard to guarantee feasible solution in the optimisation problem. Therefore, the value of the disturbance bound is relaxed in this study and chosen as 0.1 m/s for all the driving manoeuvres to guarantee the feasible solution.

6.4.3 Constraint conversion between nonlinear high fidelity model and linear equivalent model

The nonlinear high fidelity model constraints in section 6.2.3 include the single-link angle θ_{SL}, the control input ω_{SL} and low speed shaft torque T_{lss}, which correspond to actuator displacement Δz_{lin}, actuator velocity $\dot{z}_{lin}$ and actuator force F_{lin} constraints in the linear equivalent model. Since the robust model predictive control is synthesised with the linear equivalent model, the practical constraints of the nonlinear model have to be converted to obtain the constraints values in the linear equivalent model. The actuator displacement is one of the states and its limit is obtained with β function utilised since $\Delta\theta_{SL}$ can be measured and $\Delta z_{lin} = \beta\Delta\theta_{SL}$ [4]. Both the actuator velocity (control input) and the actuator force are taken into account in the constraint signal $\mathbf{f}$. To convert the practical constraints in the nonlinear model to the corresponding ones in the linear equivalent model, the figure of conversion function α with respect to Δz_{lin} is shown in figure.6.2, (based on function plots of α in Figure 2.6) to introduce the constraint of $\dot{z}_{lin}$ in the linear model. Similarly, the low speed shaft torque T_{lss} in the nonlinear model which is limited between zero and 97 Nm to gearbox backlash effect avoidance, can be converted to

the actuator force F_{lin}, where F_{lin} can be expressed in terms of the states (Δl_s and Δz_{lin}) as follows:

$$F_{lin} = m_s g + k_{eq}(\Delta l_s - \Delta z_{lin}). \tag{6.28}$$

It follows that the constraints on F_{lin} can guarantee the constraints on T_{lss} following the same procedure shown in Figure 6.2 since $\alpha = T_{lss}/F_{lin}$

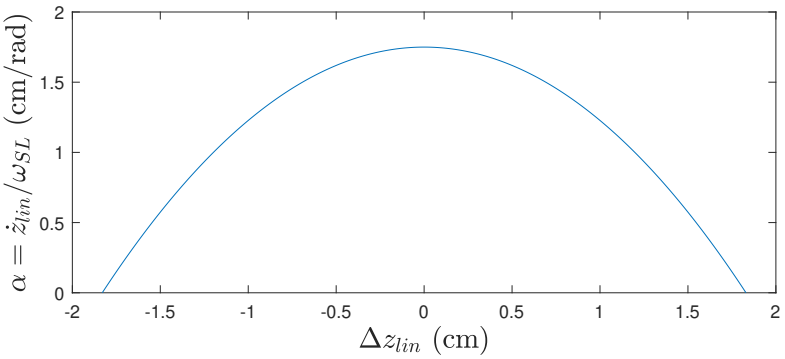


Figure 6.2: Plot of function α with respect to Δz_{lin} for conversion between multibody and linear equivalent model.

In addition to the constraints considered in the control design, the power constraints which are typically soft constraints are imposed in the actuator control to limit energy consumption. In addition to what was done in [4], which intentionally limits the single-link actuator power to 500 W, in this study, the power constraints limit the currents obtained through a simplified computation of electrical power flow to/from the PMSM based on the electromechanical output power and on either motoring mode (500 W power flow from the PMSM) or generating mode (1500 W power flow to the PMSM), which can be shown as follows:

$$-\underline{P} \leq P = \frac{3}{2}(v_d i_d + v_q i_q) \leq \bar{P}, \tag{6.29}$$

where (v_d,i_d),(v_q,i_q) are the pairs of d-axis and q-axis currents and voltages respectively [4], $\underline{P}$ and $\bar{P}$ are minimum and maximum PMSM power values and typically

$\bar{P} \leq \underline{P}$ to allow for high power flows when regenerating.

6.5 Numerical Simulations and analysis

In this section, with nonlinear multi-body quarter car SAVGS model described in [3], and control strategies proposed in section 6.3 and section 6.4, a group of ISO driving manoeuvres, containing, i) sinusoidal profile, ii) smoothed bump and hole, iii) random road class A-C, are tested to evaluate the efficiency and robustness of the synthesised controllers. Since the suspension damping coefficient is considered to be uncertain, the suspension damping coefficients c_{eq} is considered to be an uncertain parameter (structured uncertainty) which could vary by up to $\pm 208 Ns/m$ from its nominal value, where $c_{eq}^{(nom)} = 2087.4\, Ns/m$, $c_{eq}^{(min)} = 1878\, Ns/m$ and $c_{eq}^{(max)} = 2296\, Ns/m$. The time-invariant uncertainty has the form $\mathbf{\Delta} := \{\delta : \delta \in \mathbb{R}\}$ and the disturbances set is $\mathcal{D} := \{d \in \mathbb{R}^{n_d} : -0.15 \leq d_i \leq 0.15, i = 1, \ldots, n_d\}$ due to the maximum value of the random road A road plate vertical velocity. The constraints are $-\bar{u} \leq u_k \leq \bar{u} := \dot{z}_{lin}^{(max)}, k = 0, \ldots, N-1$ and the initial state is obtained from the RMPC offline calculation using Algorithm 1 proposed in [77]. The cost signal is $z_k = [\sqrt{10}\ddot{z}_s\ \sqrt{10}\Delta l_t\ 10\sqrt{6}\dot{z}_{lin}]^T$ which has the weight tuned using trial and error method and incorporated inside; the reference cost in (6.8) is $\bar{z}_k = [0\ 0\ 0]^T$. Similarly, the terminal cost signal incorporated with weights inside is $z_N = [20\ddot{z}_s\ 20\Delta l_t]^T$ and $\bar{z}_N = [0\ 0]^T$. The terminal cost weight is almost 10 times than cost weight which guarantees stability to converge to the invariant set. The objective is to minimise the cost function in (6.8), noting from (6.3) and (6.4) that this cost signal can be expressed in terms of x_k and u_k and this can be used to define C_{zu} and D_{zu}. The prediction horizon is set as $N = 5$. The block diagram in Figure 6.3 shows the closed-loop scheme of the overall controller (synthesised in Section.6.4) and plant (proposed in Figure 6.1), used for closed-loop simulations, where the PI parameters

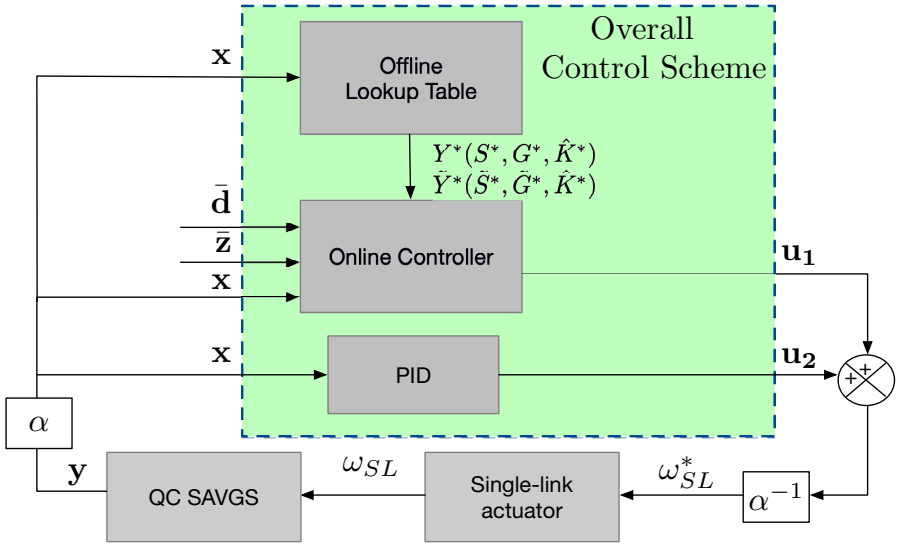


Figure 6.3: Block diagram of quarter car SAVGS closed-loop control and simulation scheme.

6.5.1 Simulation With Harmonic Road

Figure6.4 presents the time response results for the body acceleration, tire deflection, suspension travel and single-link angle of the quarter-car in response to a sinusoidal road disturbance of 2 Hz, for the passive, H_∞ and RMPC controllers. It can be seen that the H_∞ can significantly attenuate the performance objectives, with a 67% and 64% (rms) drop in the sprung mass acceleration and the tire deflection, respectively, as compared to the passive suspension. RMPC has a similar performance to that of H_∞ with marginally larger mitigation in terms of body acceleration (74%) and tire deflection(70%), as compared to the passive suspension. Furthermore, Figure 6.5, indicates that the RMPC control scheme does satisfy all the hard constraints of actuators and the soft constraints, which are shown as suspension travel and single-link angle in Figure 6.4.

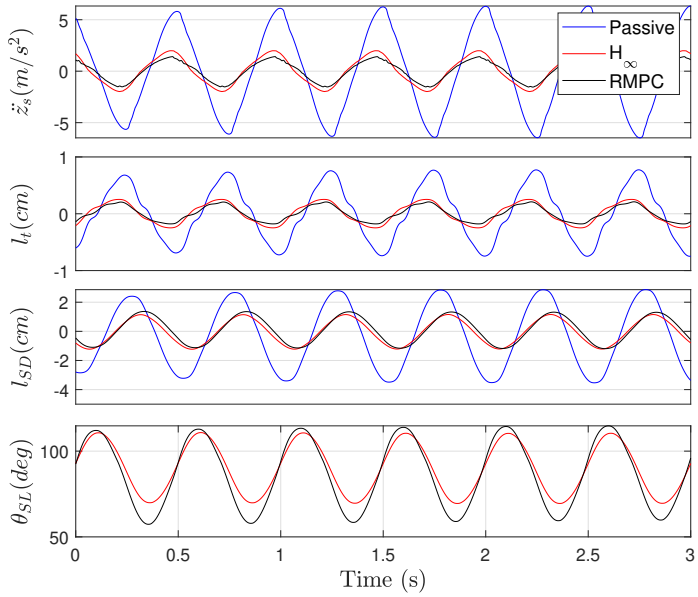


Figure 6.4: Numerical simulation results (top to bottom): the sprung mass acceleration, tire deflection, suspension deflection and single-link angle, when the quarter car SAVGS is undergoing a harmonic road profile, with 2 Hz frequency and 2.75 cm peak-to-peak amplitude [86], for different cases of active suspension control.

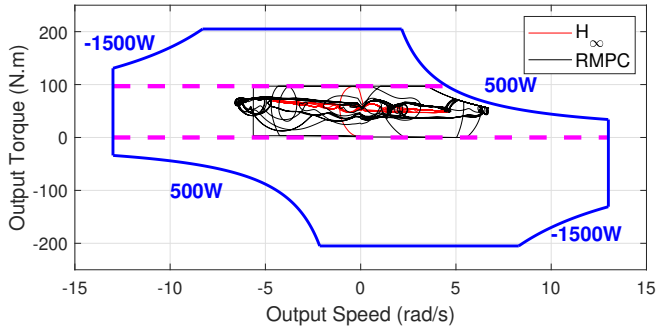


Figure 6.5: Output torque vs. output speed characteristics of the quarter car SAVGS when it is undergoing a sinusoidal road profile for different cases of active suspension control, with torque-speed operating points and actuator limit boundaries shown in blue solid lines and magenta solid lines, respectively.

6.5.2 Simulation With Smoothed Bump and Hole

Speed bumps or humps are common in some roadways and are normally approximated as a raised cosine shape. The mathematical representation of the wheel road

heights running over a standard laterally uniform bump (0.0275 m height and 1.4 m length) is presented below:

$$h = \ 0.025(1 - cos(2\pi x/2)), \tag{6.30}$$

where h is a function of the travel distance x.

Numerical simulation results with the SAVGS-retrofitted quarter car at a forward speed of 100 km/h with different active control cases are shown in Figure 6.6 and Figure 6.7. Similarly to the sinusoidal road cases, RMPC outperforms H_∞ with 9% and 7.5% further reduction in terms of vertical acceleration and tire deflection as compared to the passive suspension, respectively, while the actuator constraints are satisfied.

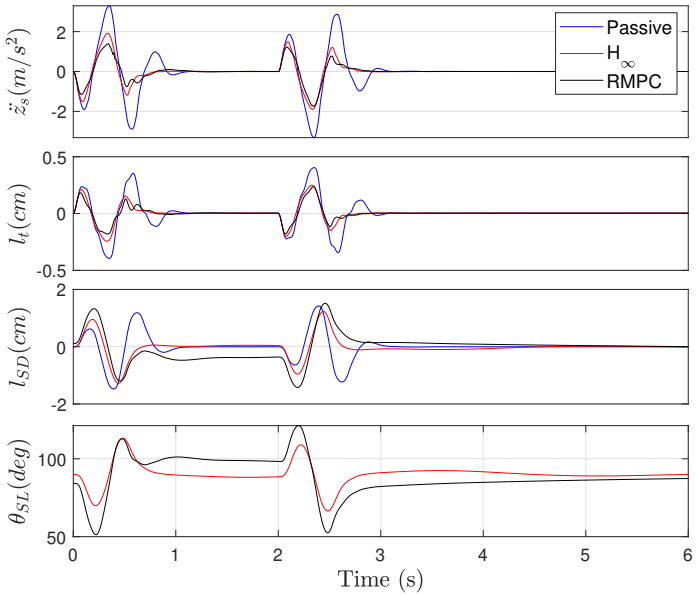


Figure 6.6: Numerical simulation results (top to bottom): the sprung mass acceleration, tire deflection, suspension deflection and single-link angle when the quarter-car SAVGS is running over a smoothed bump (0-2 s) and hole (0-4 s), with 2.75 cm peak-to-peak amplitude in road height, 1.4 m width and 10 km/h driving speed [86] for different cases of active suspension control.

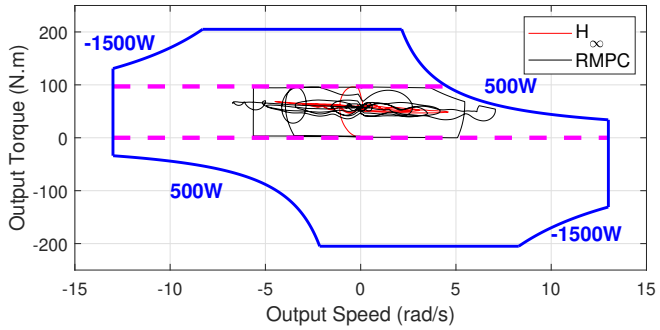


Figure 6.7: Output torque vs. output speed characteristics when the quarter car SAVGS is undergoing a smoothed bump and hole road profile for different cases of active suspension control, with torque-speed operating points and actuator limit boundaries shown in blue solid lines and magenta solid lines respectively.

6.5.3 Simulation With Random Road

The ISO random roads are used to simulate road unevenness. The parameters of the random road profiles for nonlinear simulations are selected as: the spatial frequency range $[n_{min},n_{max}] = [0.01,1]$ cycles/m, the road length L=1 km and $\Delta n = 0.001$ cycles/m ($\Delta n \leq 1/L$ should be satisfied).

In the numerical simulation environment, the SAVGS-retrofitted quarter car is driven with a forward speed of 100 km/h. Different road profiles (of same unevenness) against traveled distance are generated for the wheel. In the present work, three 10 km long road sections have been generated and used to validate the improvement of the ride comfort and road holding in typical uneven road surface conditions corresponding to a good highway (class A), an average quality road (class B), and a poor quality road (road C).

The nonlinear simulation PSDs of the sprung mass acceleration and the tire deflection over random road (Classes A-C) are shown in Figure 6.8. The H_∞ and RMPC both give a notably improved performance in terms of ride comfort and road holding at around human-sensitive frequency (1-3 Hz) as compared to the passive

case. It can be observed that the RMPC universally outperforms H_∞ in terms of sprung mass acceleration attenuation. In particular, although the PSD plot in Figure 6.8-bottom shows that Δl_t deteriorates at about 7 Hz with RMPC, the RMS value detailed in Table 6.1 demonstrates that overall there is improvement.

The output torque-speed operating points for the actuators are plotted in Figure 6.9 alongside the power, torque and speed constraint envelop. The most power consuming event, the poor quality random road C, is examined. Results shows that the proposed RMPC control utilises the actuator capabilities fully: the operating torque-speed points approach boundaries without exceeding them. The H_∞ control though guarantee robustness, it only employs part of the actuator capability leading to the conservative performance in terms of ride comfort and road holding shown above in Figure 6.8.

Table 6.1: RMS values of the $\ddot{z}_s$ and l_t with different controllers (Rand denotes random)

	Symbol	Passive	H_∞	$RMPC$
RandC	$\ddot{z}_s$	1.911	1.602(-16%)	1.570(-18%)
	l_t	0.281	0.270(-4.1%)	0.269(-4.5%)
RandB	$\ddot{z}_s$	1.055	0.957(-9.3%)	0.915(-13.2%)
	l_t	0.144	0.147(+1.9%)	0.141(-2.1%)
RandA	$\ddot{z}_s$	0.627	0.573(-8.6%)	0.506(-19.3%)
	l_t	0.083	0.085(+2.2%)	0.081(-2.5%)

6.6 CONCLUSIONS

The recently proposed mechatronic suspension of the Series Active Variable Geometry Suspension (SAVGS) is investigated in the application to a quarter car with suspension damping uncertainties taken into consideration in the suspension control design, revealing promising potential in terms of ride comfort and road holding improvement.

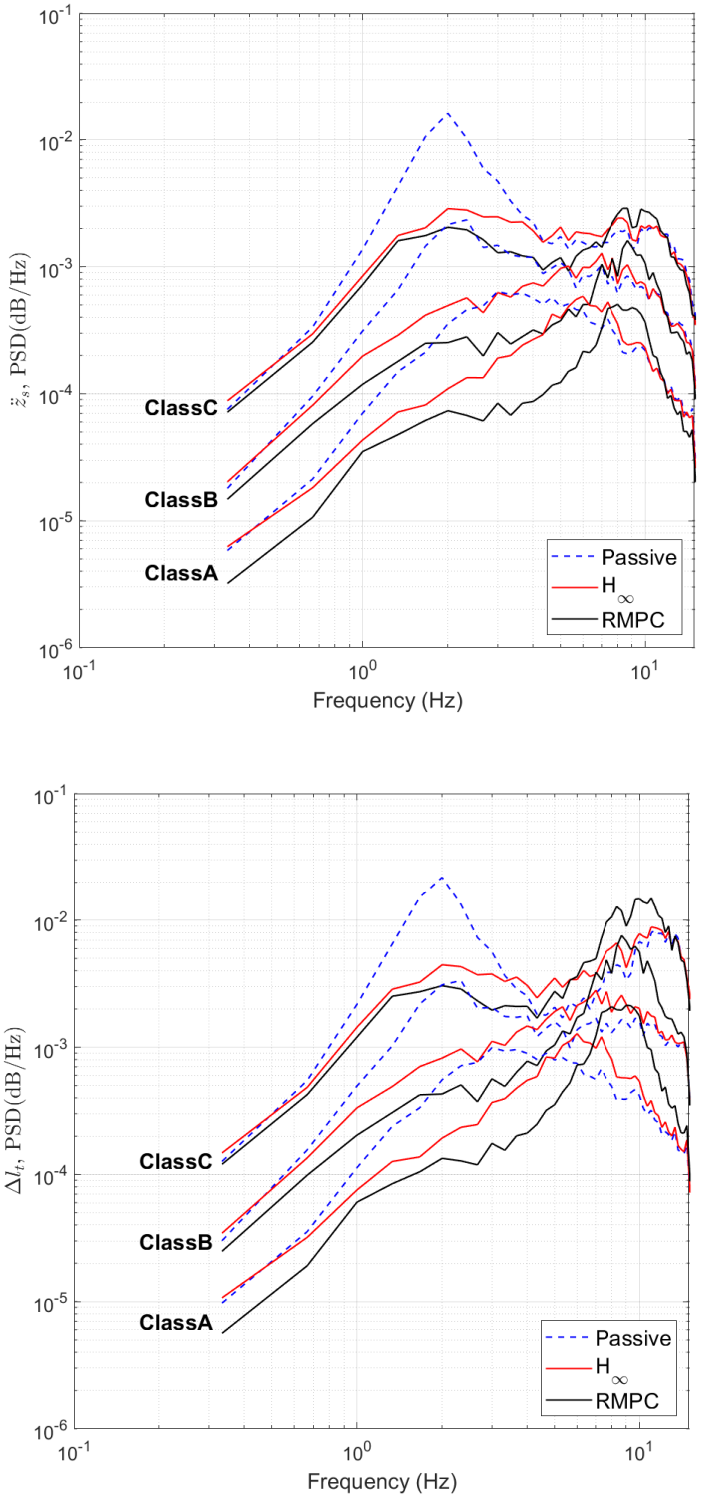


Figure 6.8: Numerical simulation results: the PSD estimate of the sprung mass acceleration (top) and tire deflection (bottom), when the quarter car SAVGS is undergoing random road (Classes A-C) for different cases of active suspension control.

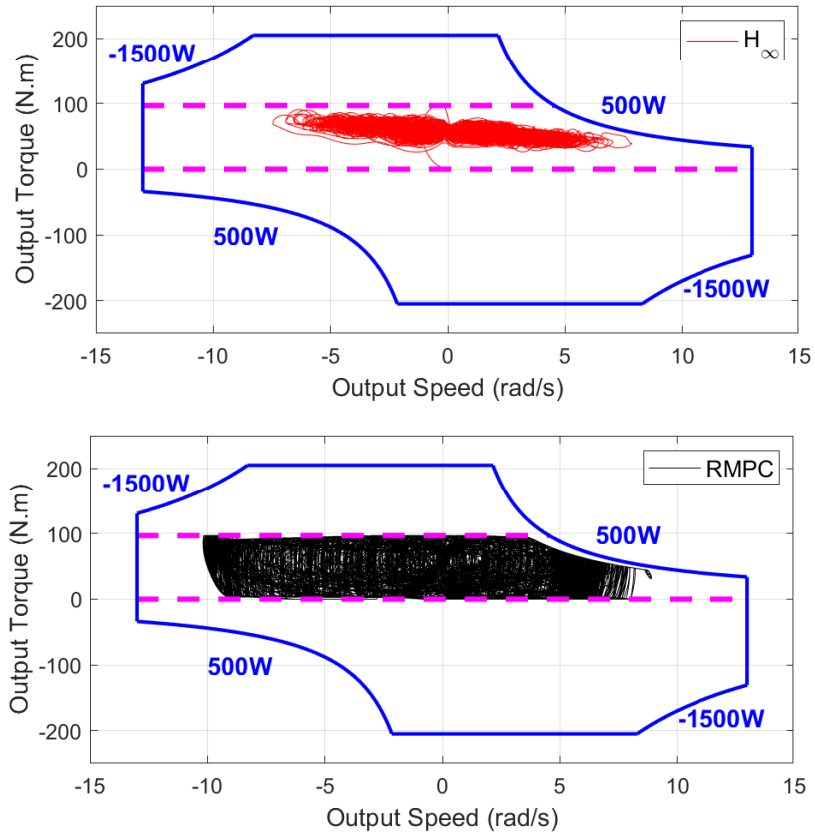


Figure 6.9: Output torque vs. output speed characteristics when the quarter car SAVGS is undergoing random road profile (class C) for H_∞ control (top) and robust model predictive control (bottom), with torque-speed operating points and actuator limit boundaries shown in blue solid lines and magenta solid lines respectively.

The robust model predictive control scheme is proposed that can effectively improve the road holding and ride comfort performance at the human comfort frequency range (1-8 Hz) with the uncertain system description, while system stability is preserved by the offline algorithm 1 proposed in [77]see Figure 6.9. As compared to the H_∞ control, the RMPC control provides a substantial performance improvement and ensures hard constraint satisfaction see Figure 6.8 and Figure 6.9 respectively. Moreover, the proposed robust model predictive control scheme provides decent performance improvement as compared to H_∞, with 18.7%, 19.8% and 11.8% in terms of body acceleration in the harmonic, smoothed bump and hole and random road

class A driving manoeuvres see Figure 6.4, Figure 6.6 and Figure 6.8. Numerical simulations of various ISO manoeuvres, such as sinusoidal road, smoothed bump and hole and random road (Classes A-C) with a high fidelity model of the quarter-car with SAVGS, have been provided to illustrate the effectiveness of the proposed methods.

This work forms a novel application to SAVGS and use of the quarter car model assists in explaining the outcomes and efficiency of the LMI-based RMPC approach. The control method has strong potential to be considered further in this suspension application and further investigation is suggested for future work.

Chapter 7

Conclusions and Future Work

This thesis has set out the target of developing control strategies for the recently introduced SAVGS and PALS concepts. To this end, work has been successfully undertaken on the μ-synthesis-based control and its application to the GT (SAVGS) and SUV (PALS) full-car models, with practical uncertainties taken into consideration. By doing so, the project has revealed promising potential for both low-frequency chassis levelling and high-frequency ride comfort, offering road-holding improvement under variable payload. Moreover, the feedforward PID control strategy obtained in this work achieves chassis levelling and speed-of-convergence enhancement for a PALS low-frequency application. The final RMPC scheme proposed in this work can effectively improve both road holding and the ride comfort. Therefore, the results of this thesis lay the foundation for the success of the experimental validation work on the SAVGS and PALS and the implementation of the control technique in other vehicle models. On the basis of the research outcomes obtained in this thesis, Section 7.1 draws key conclusions, while Section 7.2 identifies areas for future work, promoting the addition of both the SAVGS and the PALS to the vehicle market.

7.1 Conclusions

1. Important realistic uncertainties are identified and characterised in terms of the operation of both the SAVGS and PALS-retrofitted full-car models (ignored in the previous linearisation work), for the purpose of designing an effective active suspension control that can operate under a variable vehicle payload.

2. The μ-synthesis control strategy is utilised for both SAVGS and PALS high-frequency applications, offering essential improvements over the passive suspension system in terms of both road holding and ride comfort at the human-comfort frequency range (1-8 Hz). In addition, accommodating the characterised system uncertainties, the proposed μ-synthesis-based control scheme provides a more robust suspension performance enhancement of the SAVGS/-PALS full car, compared to that offered by conventional H_∞-based control schemes, which significantly under-perform at deviated mass parameters.

3. The developed multi-objective PID and μ-synthesis control schemes are merged to enable all the functions of PALS in a unified control scheme for both low-frequency chassis attitude stabilisation (e.g., chassis levelling) and high-frequency vehicle vibration attenuation, given selected uncertainties. Compared to the conventional hybrid control of multi-objective PID and H_∞ control for a nominal payload, the synthesised hybrid control preserves the high-frequency ride comfort and road-holding improvement without deteriorating the low-frequency chassis levelling performance. In addition, the developed multi-objective PID μ-synthesis control significantly outperforms the conventional hybrid control scheme, especially at high frequencies and under the varied payload; it can also effectively control low-frequency dynamics, which

μ-synthesis control does not cover.

4. An RMPC scheme is proposed that can effectively improve the road holding and ride-comfort performance at the human-comfort frequency range (1-8 Hz), with actuator capabilities fully utilised as compared to H_∞ control, while system stability is preserved by the proposed offline algorithm.

5. The proposed feedforward PID control strategy with nonlinear polynomial fitting method applied is proposed for a PALS low-frequency application, offering an essential improvement to the passive suspension system and decent enhancement to 'PALS-PID' in terms of speed of response and chassis attitude stabilisation.

7.2 Future work

Based on this work on control strategies for both the SAVGS and PALS quarter- and full-car models, the following avenues are suggested for future research.

1. Based on the outcomes of this thesis, the experimental validation of the single-link variant of the SAVGS control and rocker-pushrod of the PALS control can be executed. Specifically, a quarter-car test-rig control has been published in [4, 22], in which experiments are presented that demonstrate the practicality and feasibility of the SAVGS/PALS, in addition to their performance enhancement and the robustness of the controller's behaviour. Furthermore, the SAVGS and the PALS could be integrated in a full car, following which an experimental evaluation of the controller for the full-car SAVGS/PALS model could be explored on road tests.

2. Physical space and weight increments, economic costs, and overall system reliability and maintenance have been introduced by the novel mechatronic

suspension systems; these will have to be evaluated in an experimental study before any development by car manufacturers can take place.

3. According to the control design, the advanced camera or look-ahead sensor is equipped to enable road-preview control (such as fuzzy logic control and MPC) to further exploit the potential of the SAVGS and the PALS. Additionally, the sliding mode control can be implemented; this introduces a sliding surface to allow for faster tracking of the position reference (pitch and roll angle) for the attitude motion mitigation, while still guaranteeing the robust behaviour of the system.

4. Energy demand is one of the major problems in commercialisation. Therefore, various different electromagnetic harvesting-based dampers are to be introduced to replace the conventional hydraulic damper and recover the dissipated energy. In addition, state-of-the-art energy harvesting-based multi-objective control methodologies are to be developed that will simultaneously ensure the ride comfort, road-holding and energy-harvesting performance.

Bibliography

[1] C. Arana, S. A. Evangelou, and D. Dini, "Series active variable geometry suspension for road vehicles," *IEEE/ASME Transactions On Mechatronics*, vol. 20, no. 1, pp. 361–372, 2014.

[2] Arana, Carlos and Evangelou, Simos A and Dini, Daniele, "Series active variable geometry suspension application to chassis attitude control," *IEEE/ASME Transactions on Mechatronics*, vol. 21, no. 1, pp. 518–530, 2015.

[3] C. Arana, S. A. Evangelou, and D. Dini, "Series active variable geometry suspension application to comfort enhancement," *Control Engineering Practice*, vol. 59, pp. 111–126, 2017.

[4] M. Yu, C. Arana, S. A. Evangelou, and D. Dini, "Quarter-car experimental study for series active variable geometry suspension," *IEEE Transactions on Control Systems Technology*, vol. 27, no. 2, pp. 743–759, 2017.

[5] M. Yu, S. A. Evangelou, and D. Dini, "Parallel active link suspension: Full car application with frequency-dependent multiobjective control strategies," *IEEE Transactions on Control Systems Technology*, pp. 1–16, 2021.

[6] M. Smith and F.-C. Wang, "Performance benefits in passive vehicle suspensions employing inerters," in *42nd IEEE International Conference on Decision and Control (IEEE Cat. No.03CH37475)*, vol. 3, 2003, pp. 2258–2263 Vol.3.

[7] C. Arana, S. A. Evangelou, and D. Dini, "Series active variable geometry suspension application to chassis attitude control," *IEEE/ASME Transactions on Mechatronics*, vol. 21, no. 1, pp. 518–530, 2016.

[8] H. Kim and H. Lee, "Height and leveling control of automotive air suspension system using sliding mode approach," *IEEE Transactions on Vehicular Technology*, vol. 60, no. 5, pp. 2027–2041, 2011.

[9] Kim, Hyunsup and Lee, Hyeongcheol, "Fault-tolerant control algorithm for a four-corner closed-loop air suspension system," *IEEE Transactions on industrial Electronics*, vol. 58, no. 10, pp. 4866–4879, 2011.

[10] BUYACAR TEAM, "Car with air suspension," https://www.buyacar.co.uk/cars/901/cars-with-air-suspension, 2021.

[11] Wikipedia, "Air suspension," https://en.wikipedia.org/wiki/Air_suspension#cite_note-25.

[12] LOEBER MOTORS, "Mercedes air suspension," https://www.loebermotors.com/blog/what-is-a-mercedes-benz-airmatic-suspension/.

[13] Mercedes-Benz of Ontario, "Benefit of mercedes-benz airmatic suspension," https://www.mbontario.com/mercedes-benz-airmatic-suspension-benefits/?__cf_chl_tk=XHYTxzfhrMymzMLdSu6ifJfJCXbgd1i3O_yN38ZSKFw-1649560957-0-gaNycGzNCCU, 2018.

[14] Audi Media Center, "Audi adaptive suspension," https://www.audi-mediacenter.com/en/technology-lexicon-7180/chassis-7185.

[15] Audi Technology Portal, "Adaptive air suspension," https://www.audi-technology-portal.de/en/chassis/suspension-control-systems/adaptive-air-suspension_en, 2017.

[16] Fred Lambert, "Tesla model x smart air suspension," https://electrek.co/2016/10/07/tesla-increases-base-price-model-x-smart-air-suspension-standard/, 2016.

[17] Wikipedia, "Active body control," https://en.wikipedia.org/wiki/Active_Body_Control.

[18] Peter H, "Active body control/magic body control," https://500sec.com/abc-active-body-control-mbc-magic-body-control/, 2009.

[19] Adrian Padeanu, "Audi A8 predictive suspension," https://uk.motor1.com/news/360590/audi-a8-predictive-air-suspension/.

[20] D. Crolla, "Vehicle dynamics—theory into practice," *Proceedings of the Institution of Mechanical Engineers, Part D: Journal of automobile engineering*, vol. 210, no. 2, pp. 83–94, 1996.

[21] C. Arana, "Active variable geometry suspension for cars," Ph.D. dissertation, Imperial College London, 2015.

[22] M. Yu, C. Arana, S. A. Evangelou, D. Dini, and G. D. Cleaver, "Parallel active link suspension: A quarter-car experimental study," *IEEE/ASME Transactions on Mechatronics*, vol. 23, no. 5, pp. 2066–2077, 2018.

[23] M. Yu, S. A. Evangelou, and D. Dini, "Position control of parallel active link suspension with backlash," *IEEE Transactions on Industrial Electronics*, vol. 67, no. 6, pp. 4741–4751, 2019.

[24] C. Cheng, "Control strategies of series active variable geometry suspension for cars," Ph.D. dissertation, Imperial College London, 2017.

[25] M. Yu, C. Cheng, S. Evangelou, and D. Dini, "Robust control for a full-car

prototype of series active variable geometry suspension," in *2019 IEEE 58th Conference on Decision and Control(CDC)*, 2019.

[26] C. Cheng and S. A. Evangelou, "Series active variable geometry suspension robust control based on full-vehicle dynamics," *Journal of Dynamic Systems, Measurement, and Control*, vol. 141, no. 5, p. 051002, 2019.

[27] M. Fujita, T. Namerikawa, F. Matsumura, and K. Uchida, "μ-synthesis of an electromagnetic suspension system," *IEEE Transactions on Automatic Control*, vol. 40, no. 3, pp. 530–536, 1995.

[28] T. Sun, F. Yu, and J. Liu, "The mixed-uncertainty modeling and control for active suspension based on robust mu-synthesis," *JOURNAL-SHANGHAI JIAOTONG UNIVERSITY-CHINESE EDITION-*, vol. 40, no. 6, p. 0936, 2006.

[29] M. Fleps-Dezasse, T. Bünte, F. Svaricek, and J. Brembeck, "Lpv feedforward control of semi-active suspensions for improved roll stability," *Control Engineering Practice*, vol. 78, pp. 1–11, 2018.

[30] ISO, "8608:2016, Mechanical vibration - Road surface profiles - reporting of measured data," Geneva, Switzerland, 2016.

[31] P. Zhang, H. Yue, Z. Shi, J. Lin, and Z. Chen, "A fuzzy pid algorithm-based attitude control method of suspension-type small rail vehicles," *Journal of Vibration Engineering & Technologies*, pp. 1–20, 2021.

[32] R. Kalaivani, K. Sudhagar, and P. Lakshmi, "Neural network based vibration control for vehicle active suspension system," *Indian Journal of Science and Technology*, vol. 9, no. 1, pp. 1–8, 2016.

[33] W. Sun, H. Gao, and O. Kaynak, "Adaptive backstepping control for active suspension systems with hard constraints," *IEEE/ASME transactions on mechatronics*, vol. 18, no. 3, pp. 1072–1079, 2012.

[34] K. El Majdoub, F. Giri, and F.-Z. Chaoui, "Adaptive backstepping control design for semi-active suspension of half-vehicle with magnetorheological damper," *IEEE/CAA Journal of Automatica Sinica*, vol. 8, no. 3, pp. 582–596, 2020.

[35] C. Liu, L. Chen, X. Yang, X. Zhang, and Y. Yang, "General theory of skyhook control and its application to semi-active suspension control strategy design," *IEEE Access*, vol. 7, pp. 101 552–101 560, 2019.

[36] S. Park, A. Turnip, K.-S. Hong *et al.*, "Application of lqr control theory to the design of modified skyhook control gains for semi-active suspension systems," in *2009 ICCAS-SICE*. IEEE, 2009, pp. 4698–4703.

[37] J. H. Park and Y. S. Kim, "An h_∞ controlller for active suspensions and its robustness based on a full-car model," *IFAC Proceedings Volumes*, vol. 32, no. 2, pp. 8178–8183, 1999.

[38] G. Wang, C. Chen, and S. Yu, "Robust non-fragile finite-frequency h_∞ static output-feedback control for active suspension systems," *Mechanical Systems and Signal Processing*, vol. 91, pp. 41–56, 2017.

[39] C. Cheng, S. A. Evangelou, C. Arana, and D. Dini, "Active variable geometry suspension robust control for improved vehicle ride comfort and road holding," in *2015 American Control Conference (ACC)*. IEEE, 2015, pp. 3440–3446.

[40] K. Zhou and J. C. Doyle, *Essentials of robust control*. Prentice hall Upper Saddle River, NJ, 1998, vol. 104.

[41] H. Pan, W. Sun, H. Gao, and J. Yu, "Finite-time stabilization for vehicle active suspension systems with hard constraints," *IEEE transactions on intelligent transportation systems*, vol. 16, no. 5, pp. 2663–2672, 2015.

[42] Y. M. Sam, J. H. Osman, and M. R. A. Ghani, "A class of proportional-integral sliding mode control with application to active suspension system," *Systems & control letters*, vol. 51, no. 3-4, pp. 217–223, 2004.

[43] B.-L. Zhang, G.-Y. Tang, and F.-L. Cao, "Optimal sliding mode control for active suspension systems," in *2009 International conference on networking, sensing and control*. IEEE, 2009, pp. 351–356.

[44] Chen, Shi-An and Wang, Jun-Cheng and Yao, Ming and Kim, Young-Bae, "Improved optimal sliding mode control for a non-linear vehicle active suspension system," *Journal of Sound and Vibration*, vol. 395, pp. 1–25, 2017.

[45] L. Chai and T. Sun, "The design of lqg controller for active suspension based on analytic hierarchy process," *Mathematical Problems in Engineering*, vol. 2010, 2010.

[46] H. Habibullah, H. Pota, I. R. Petersen, and M. Rana, "Tracking of triangular reference signals using lqg controllers for lateral positioning of an afm scanner stage," *IEEE/ASME Transactions on Mechatronics*, vol. 19, no. 4, pp. 1105–1114, 2013.

[47] A. H. Mohamed, D. Abidou, and S. A. Maged, "Lqr and pid controllers performance on a half car active suspension system," in *2021 International Mobile, Intelligent, and Ubiquitous Computing Conference (MIUCC)*. IEEE, 2021, pp. 48–53.

[48] D. Q. Mayne, J. B. Rawlings, C. V. Rao, and P. O. Scokaert, "Constrained model predictive control: Stability and optimality," *Automatica*, vol. 36, no. 6, pp. 789–814, 2000.

[49] B. Sereni, R. Manesco, E. Assunção, and M. Teixeira, "Relaxed lmi con-

ditions for the design of robust static output feedback controllers," *IFAC-PapersOnLine*, vol. 51, no. 25, pp. 428–433, 2018.

[50] S. M. Moradi, A. Akbari, and M. Mirzaei, "An offline lmi-based robust model predictive control of vehicle active suspension system with parameter uncertainty," *Transactions of the Institute of Measurement and Control*, vol. 41, no. 6, pp. 1699–1711, 2019.

[51] H. Li, H. Liu, H. Gao, and P. Shi, "Reliable fuzzy control for active suspension systems with actuator delay and fault," *IEEE Transactions on Fuzzy Systems*, vol. 20, no. 2, pp. 342–357, 2011.

[52] X. Shao, F. Naghdy, and H. Du, "Reliable fuzzy h_∞ control for active suspension of in-wheel motor driven electric vehicles with dynamic damping," *Mechanical Systems and Signal Processing*, vol. 87, pp. 365–383, 2017.

[53] J. Sun and K. Zhao, "Adaptive neural network sliding mode control for active suspension systems with electrohydraulic actuator dynamics," *International Journal of Advanced Robotic Systems*, vol. 17, no. 4, p. 1729881420941986, 2020.

[54] N. Yagiz, Y. Hacioglu, and Y. Taskin, "Fuzzy sliding-mode control of active suspensions," *IEEE Transactions on industrial electronics*, vol. 55, no. 11, pp. 3883–3890, 2008.

[55] H. Li, J. Yu, C. Hilton, and H. Liu, "Adaptive sliding-mode control for nonlinear active suspension vehicle systems using t–s fuzzy approach," *IEEE Transactions on industrial electronics*, vol. 60, no. 8, pp. 3328–3338, 2012.

[56] E. Bender, "Optimum linear preview control with application to vehicle suspension," 1968.

[57] C. Gohrle, A. Schindler, A. Wagner, and O. Sawodny, "Design and vehicle implementation of preview active suspension controllers," *IEEE Transactions on Control Systems Technology*, vol. 22, no. 3, pp. 1135–1142, 2013.

[58] I. Youn and A. Hac, "Preview control of active suspension with integral action," *International Journal of Automotive Technology*, vol. 7, no. 5, pp. 547–554, 2006.

[59] A. Moran, M. Nagai, and M. Hayase, "Design of active suspensions with h_∞ preview control," in *International Symposium on Advanced Vehicle Control*, 1996, pp. 215–233.

[60] S. Ryu, Y. Kim, and Y. Park, "Robust h_∞ preview control of an active suspension system with norm-bounded uncertainties," *International Journal of Automotive Technology*, vol. 9, no. 5, pp. 585–592, 2008.

[61] C. Göhrle, A. Wagner, A. Schindler, and O. Sawodny, "Active suspension controller using mpc based on a full-car model with preview information," in *2012 American Control Conference (ACC)*. IEEE, 2012, pp. 497–502.

[62] S. De Bruyne, H. Van der Auweraer, J. Anthonis, W. Desmet, and J. Swevers, "Preview control of a constrained hydraulic active suspension system," in *2012 IEEE 51st IEEE Conference on Decision and Control (CDC)*. IEEE, 2012, pp. 4400–4405.

[63] J. Theunissen, A. Sorniotti, P. Gruber, S. Fallah, M. Ricco, M. Kvasnica, and M. Dhaens, "Regionless explicit model predictive control of active suspension systems with preview," *IEEE Transactions on Industrial Electronics*, vol. 67, no. 6, pp. 4877–4888, 2019.

[64] Sultoni, Arif Indro and Sutantra, I Nyoman and Pramono, Agus Sigit, "h_∞

multi-objective implementation for energy control of electromagnetic suspension," *International Review of Mechanical Engineering*, vol. 9, no. 6, 2015.

[65] A. Casavola, F. Tedesco, and P. Vaglica, "Full-car multivariable control strategies for energy harvesting by regenerative suspension systems," in *2020 American Control Conference (ACC)*. IEEE, 2020, pp. 2256–2261.

[66] M. Ataei, E. Asadi, A. Goodarzi, A. Khajepour, and M. B. Khamesee, "Multi-objective optimization of a hybrid electromagnetic suspension system for ride comfort, road holding and regenerated power," *Journal of Vibration and Control*, vol. 23, no. 5, pp. 782–793, 2017.

[67] R. Sharp and S. Hassan, "An evaluation of passive automotive suspension systems with variable stiffness and damping parameters," *Vehicle System Dynamics*, vol. 15, no. 6, pp. 335–350, 1986.

[68] H. E. Vongierke, "The iso standard: Guide for the evaluation of human exposure to whole-body vibration," in *NASA. Langley Res. Center The 1975 Ride Quality Symp.*, 1975.

[69] R. Sharp and D. Crolla, "Road vehicle suspension system design-a review," *Vehicle system dynamics*, vol. 16, no. 3, pp. 167–192, 1987.

[70] H. Wang, M. Fu, and H. Zhang, "h_∞ control for stochastic systems with disturbance preview," *SIAM Journal on Control and Optimization*, vol. 58, no. 1, pp. 215–242, 2020.

[71] H. E. Tseng and D. Hrovat, "State of the art survey: active and semi-active suspension control," *Vehicle system dynamics*, vol. 53, no. 7, pp. 1034–1062, 2015.

[72] ISO, "2631-1:1997, Mechanical vibration and shock - Evaluation of human exposure to whole-body vibration - part 1: General requirements," Geneva, Switzerland, 1997.

[73] ISO, "4138: Passenger cars–steady-state circular driving behaviour–open-loop test methods," *ISO: Geneva, Switzerland*, 2012.

[74] ISO 7401: 2011, "Road vehicles–lateral transient response test methods–open-loop test methods," 2011.

[75] ISO, "7975:2006, passenger cars – braking in a turn – open loop test procedure," 2006.

[76] National Highway Traffic Safety Administration and others, "Laboratory test procedure for dynamic rollover: the fishhook maneuver test procedure," *Washington (DC): US, Department of Transportation*, 2013.

[77] Georgiou, Anastasis and Tahir, Furqan and Jaimoukha, Imad M and Evangelou, Simos A, "Computationally efficient robust model predictive control for uncertain system using causal state-feedback parameterization," *IEEE Transactions on Automatic Control*, 2022.

[78] A. Georgiou, S. Evangelou, I. Jaimoukha, and G. Downton, "Tracking control for directional drilling systems using robust feedback model predictive control." Elsevier, 2021, pp. 11 974–11 981. [Online]. Available: http://dx.doi.org/10.1016/j.ifacol.2020.12.723

[79] Z. Feng, M. Yu, C. Cheng, S. A. Evangelou, I. M. Jaimoukha, and D. Dini, "Uncertainties investigation and μ-synthesis control design for a full car with series active variable geometry suspension," *IFAC-PapersOnLine*, vol. 53, no. 2, pp. 13 882–13 889, 2020.

[80] M. V. Kothare, V. Balakrishnan, and M. Morari, "Robust constrained model predictive control using linear matrix inequalities," *Automatica*, vol. 32, no. 10, pp. 1361–1379, 1996.

[81] J. B. Rawlings and D. Q. Mayne, *Model predictive control: Theory, computation and design.* Madison, Wisconsin: Nob Hill, August 2017.

[82] J. Skaf and . S. P. Boyd, "Design of affine controllers via convex optimization," *IEEE Transactions on Automatic Control*, vol. 55, pp. 2476–2487, 2010.

[83] F. Tahir and I. Jaimoukha, "Causal state-feedback parameterization in robust model predictive control," *Automatica*, vol. 49, no. 9, pp. 2675–2682, 2013.

[84] P. O.M. Scokaert and D. Q. Mayne, "Min-max feedback model predictive control for constrained linear system," *IEEE Transaction on Automatic Control*, no. 43, pp. 1136–1142, 1998.

[85] S. Boyd, L. E. Ghaoui, and V. Balakrishnan, *Linear matrix inequalities in system and control theory.* Philadelphia: SIAM, 1994.

[86] M. Yu, S. A. Evangelou, and D. Dini, "Model identification and control for a quarter car test rig of series active variable geometry suspension," *IFAC-PapersOnLine*, vol. 50, no. 1, pp. 3376–3381, 2017.